Physik-Department E11
Lehrstuhl für
Laser- und Röntgenphysik

Time-Resolved Infrared Spectroscopy on Hydrogen Bonded Systems

Dipl.-Phys. Univ. Daniel Hutzler

Vollständiger Abdruck der von der
Fakultät für Physik der Technischen Universität München
zur Erlangung des akademischen Grades eines

Doktors der Naturwissenschaften

genehmigten Dissertation.

Vorsitzender:
Prof. Dr. Martin Zacharias

Prüfer der Dissertation:
1. Prof. Dr. Reinhard Kienberger
2. Prof. Dr. Katharina Krischer

Die Dissertation wurde am 20.06.2017 bei der
Technischen Universität München eingereicht und durch die
Fakultät für Physik am 30.08.2017 angenommen.

To my parents Heidelinde and Rudolf Hutzler

Zusammenfassung

Viele grundlegende Eigenschaften von Wasser und wässrigen Systemen lassen sich auf Wasserstoffbrücken und ihr intermolekulares Netzwerk zurückführen. Da ein direktes Vermessen dieser schwachen Bindungen sehr schwierig ist, wird oft die OH-Streckschwingung genutzt, um einen indirekten Zugang zu erhalten. Letztere ist sehr sensitiv auf ihre chemische Umgebung und kann daher als Sonde für diese verwendet werden. Dennoch ist es in vielen Fällen schwierig, einen direkten Zusammenhang zwischen spektralen und strukturellen Merkmalen herzustellen. Abhilfe können hier Salzhydrate schaffen, die die einzigartige Möglichkeit bieten, Wassermoleküle zu untersuchen, die in wohldefinierten Salzkristallen enthalten sind.
Mittels eines neuartigen Versuchsaufbaus für zeitaufgelöste Anrege–Wiederanrege–Abfrage-Spektroskopie wurden zunächst die Obertöne der OH-Streckschwingung quasi-isolierter Wassermoleküle in Natriumperchlorat-Monohydrat vermessen. Das zugehörige Potenzial wurde bis zum dritten angeregten Zustand abgetastet und die Lebenszeiten von erstem und zweitem angeregten Zustand bestimmt. Des Weiteren wurden kleine Wassercluster in Bariumperchlorat-Trihydrat untersucht. Simulationen und Symmetrieüberlegungen weisen auf eine Delokalisierung der OH-Streckschwingung hin. Darüber hinaus wurde ein Besetzungsaustausch zwischen symmetrischer und antisymmetrischer Streckschwingung beobachtet, dem konkrete Raten zugeordnet werden konnten. Die gegenseitige Kohärenz der beiden Zustände wurde anhand einer Quantenschwebung im Übergang zu einem gemeinsamen Oberton beobachtet. In weiteren Untersuchungen wurden Schwingungsspektrum und -dynamik in isotopisch verdünntem Eis in Relation zu den entsprechenden Eigenschaften ausgewählter Salzhydrate gesetzt. Die Ergebnisse zeigen, dass die Abregung der OH-Streckschwingung in Eis nur schwer mit einem einzigen Relaxationskanal erklärt werden kann. Vielmehr scheint die Relaxation über eine Kombination aus dem Oberton der Biegeschwingung und zusätzlichen Moden des Lösungsmittels stattzufinden. Abschließende Experimente befassten sich mit einer eisähnlichen Wasserstoffbrücke in Lithiumnitrat-Trihydrat. Die zugehörige OH-Streckschwingung weist spektrale Signaturen und Dynamiken auf, die denen in Eis sehr ähnlich sind. Aus der vorliegenden Kristallstruktur wurde daher geschlossen, dass drei Wassermoleküle ausreichen, um die Vibrationseigenschaften von reinem Eis zu reproduzieren.
Angefangen bei isolierten Wassermolekülen über kleine Wassercluster bis hin zu einer starken eisähnlichen Wasserstoffbrücke bietet diese Arbeit einen umfassenden Überblick über Wasserstoffbrücken-Systeme.

Abstract

Many basic properties of water and aqueous systems can be traced back to hydrogen bonds and their intermolecular network. A direct measurement of these weak polar bonds is very complicated and often yields ambiguous data. To circumvent this difficulties, commonly the OH stretching vibration is utilized. Since the latter is very sensitive to its chemical environment, it can be applied to indirectly probe the hydrogen bond system. However, it oftentimes is very complicated to link spectral to structural features. This can be remedied by using aqueous salt hydrates that are an ideal model system for water molecules embedded in well-defined crystal matrices.

First the OH stretching overtones of quasi-isolated water molecules in sodium perchlorate monohydrate were investigated by means of a newly developed setup for pump–repump–probe spectroscopy. The underlying potential was scanned up to the third excited state, and the vibrational lifetimes of the first and second excited state were extracted. Another experiment was concerned with small water clusters in barium perchlorate trihydrate. Simulations and symmetry assumptions indicate a delocalization of the OH stretching mode. Moreover, relaxation between symmetric and antisymmetric stretching was observed and could be quantified by corresponding relaxation rates. The coherence between the two vibrations was analyzed in quantum beats that were measured in the transition to a combination tone. Further experiments put the vibrational spectrum and dynamics measured in isotopically diluted ice in relation to the corresponding findings in diverse salt hydrates. The data shows that the relaxation of the stretching in ice cannot be fully explained by a single deexcitation channel. The observations rather suggest relaxation through a combination of the bend overtone and additional modes provided by the solvent molecules. Final investigations focused on an ice-like hydrogen bond, which is found in lithium nitrate trihydrate. The related OH stretching vibration exhibits spectral and dynamical behavior that closely resemble the corresponding properties in ice. Putting these findings in relation to the crystal structure of the hydrate indicates that three water molecules suffice to mimic the vibrational properties of ice.

With quasi-isolated water molecules as starting point through small water clusters up to an ice-like hydrogen bond, the present thesis provides a comprehensive overview of hydrogen bonded systems.

Contents

Chapter 1

Introduction

Liquid water is not a bit player in the theatre of life - it's the headline act. [1]

This citation found in *Nature Reviews Molecular Cell Biology* nicely expresses the vital role water plays for practically any organism. It serves as a universal solvent and dictates virtually every biochemical process. Water accounts for about two thirds of the human body, where it takes on several tasks, like being a solvent for salts and minerals, transportation of nutrients, and body temperature regulation. Behind H_2, water is the second most abundant molecule in the universe. It covers more than 70 % of the earth's surface and is the reason why our planet often is referred to as the blue planet. Currently, *Following the Water* is not only the motto of NASA's Mars exploration program but also a common approach in the search for alien life [2, 3].
Being composed of one oxygen and two hydrogen atoms, an individual water molecule is rather simple in its structure. However, its intermolecular hydrogen bonding network lends water a highly complex and extraordinary character, an understanding of which challenges scientists to this day. In liquid water, the motion due to thermal energy forces hydrogen bonds to continuously bend, stretch, shorten, break, and reform. When raising the temperature to the boiling point, the bonds completely break, and the system passes into the gas phase. On the other end, lowering the temperature coerces the water molecules into a crystalline structure that is sustained by hydrogen bonds. The orientation of these bonds upon freezing results in the commonly known density anomaly of water, which may be the most prominent one alongside various other abnormalities. It describes the fact that water shows highest density at 4 °C and therefore in the liquid phase. A first detailed investigation of this non-intuitive behavior can be back-dated to a work of the *Accademia del Cimento* from 1667 [4]. Today we know that in ice I_h (hexagonal crystal form of ordinary ice) the hydrogen bonding network or more exactly the directionality of the water–water hydrogen bond is responsible for the density anomaly.

One immediately sees that understanding water goes along with understanding its hydrogen bonding network. In general, a hydrogen bond (H bond) is the electrostatic attraction a covalently bound hydrogen atom exerts upon another nearby electronegative atom (usually fluorine, nitrogen, or oxygen). Normally, its strength is well below that of ionic and covalent bonds with binding energies ranging from 1 to roughly 170 kJ/mol. Upon hydrogen bond formation between a donor X–H and an acceptor A, the intramolecular X–H distance is elongated, while the intermolecular X$\cdots$A spacing is shortened. H bonds are often classified as electrostatic dipole–dipole interactions, whereas they also show analogies to covalent bonds, like directionality, strength, and limited number of interaction partners.
Liquid water can be referred to as a random network of molecules that is connected by hydrogen bonds and continually undergoes topological reorganization [5]. Access to its structure is provided by nuclear magnetic resonance (NMR) spectroscopy, X-ray and neutron scattering [6–11]. Nevertheless, owed to the limited time resolution, the gained information provides only average structural data. The interconnected hydrogen bonding network in liquid water is highly dynamical though. It fluctuates and rearranges on timescales between a few femtoseconds and several picoseconds [12–14]. Since these fast H bond dynamics are the key to an understanding of the physical, chemical, and biological properties of water, there is a need for ultrafast techniques and experiments. In recent years, time-resolved infrared spectroscopy evolved as one of the most prominent tools in this field. Here, usually the OH stretching vibration is consulted as indirect probe of the H bonded network [15–17]. This is reasonable, since spectral and dynamical behavior of the OH stretching vibration are very sensitive to its chemical environment and readily accessible in actual experiments. However, this kind of measurement delivers no direct structural information and data analysis can thus be ambiguous and may require complicated simulations and calculations. This effort can be bypassed by a recently proposed approach that utilizes aqueous salt hydrates as a new model system for confined water molecules incorporated in well-defined geometrical structures [18, 19]. Since the overall character of the interactions of the hydrate water molecules is the same as in bulk water, they can be applied to probe water's intermolecular energy surface. Beyond that, environment, bonding partners, and distances distinctly vary between samples prepared with different salts. Therefore, aqueous salt hydrates are very well suited to probe the particular kinds of interaction that constitute water's hydrogen bond network.

To fully exploit the potential of these systems, the most auspicious samples have to be chosen in the first place. Fortunately, the crystal structures of a vast number of salt hydrates are well-known and can be looked up in accessible data bases [20]. Moreover, good preparatory work on salt hydrates has been done at our chair at the *Technische Universität München* and one can refer to the already established experience [21–23]. To get a maximum of information out of the selected samples, cutting-edge experimental techniques and sophisticated fitting procedures have to be applied. By cross-checking and comparing the data gained in different hydrates, finally, a comprehensive picture can be generated and a bridge to bulk water and ice can be built by merging the results. Here, one can say that the whole is more than the sum of its parts since only the interplay of the particular types of interaction yields the extraordinary properties of water. An approach as just outlined forms the basis of my work and also finds its way into the structure of this thesis.
In the next chapter, first a general overview of hydrogen bonding is given. Thereafter, the OH stretching vibration is presented as an adequate probe of the latter and aqueous salt hydrates are introduced as a new model system for confined water molecules. In chapter 3, the theoretical basis for an understanding of the experimental methods and the processes within the investigated samples is outlined. Chapter 4 is concerned with the applied optical setup and its individual components, followed by a comprehensive overview of the utilized time-resolved spectroscopic methods. Experiments and results are presented in chapter 5. The first section is concerned with the relaxation of the OH stretching overtones in quasi-isolated water molecules in sodium perchlorate monohydrate. Subsequently, the system under investigation is extended to small water clusters, which are planar cyclic water trimers in barium perchlorate trihydrate. Then a bridge is built to the dynamics found in hexagonal ice. Here, first the relaxation processes in isotopically diluted ice I_h are analyzed by putting them in relation to those observed in barium perchlorate trihydrate and sodium chloride dihydrate. Finally, the observations are concluded by a comparison of the spectral properties and dynamics due to strong hydrogen bonds in lithium nitrate trihydrate and ice. In the end, the achievements are summarized and a short outlook on future experiments is given.

Chapter 2

Considerations about Hydrogen Bonded Systems

The emphasis of the following chapter lies on hydrogen bonds and how they can best be probed experimentally. First, a general overview of formation, properties, and differentiation from other types of bonding is given. Subsequently, the hydrogen bonds formed by water molecules are elucidated in particular. In the next section, the OH stretching vibration is introduced as an indirect probe of H bond strength and local chemical structure. Lastly, aqueous salt hydrates are presented as a promising model system for water molecules incorporated in defined geometrical environments.

2.1 Fundamentals of Hydrogen Bonds

Ever since their discovery in the early 20th century [24–27], hydrogen bonds have been subject of active research. This is not surprising since they are responsible for structure, function, and dynamics of a tremendous number of chemical systems. Including biochemistry, inorganic and organic chemistry, supramolecular chemistry, material science, mineralogy, molecular medicine, and pharmacy, a wide range of different fields is involved in this ongoing research [28].
Within the last decade several attempts to form a universal definition of the term *hydrogen bond* have been made. The following general description was proposed by Thomas Steiner as a modification of Pimentel and McClellan's two-point definition [29]:
An X–H· · ·A interaction is called a "hydrogen bond", if 1. it constitutes a local bond, and 2. X–H acts as proton donor to A. [28]
Hydrogen bonds are formed between a proton donor X–H and an electronegative proton acceptor A. As a result, the X–H distance is elongated, while the X· · ·A distance is shortened. One key feature of hydrogen bonds is

strong directionality. In a compound X–H$\cdots$A, a collinear orientation of the hydrogen bond with respect to the donor direction X–H is favored over a bent one. Contrary to the general opinion, A does not have to be eminently electronegative or an anion, but only has to carry a sterically perceptible negative charge. On the other hand, X–H must be at least slightly polar.
Hydrogen bond energies cover a wide range from about 1 kJ/mol up to almost 170 kJ/mol. The total H bond energy thereby is composed of different constituents. Normally, the electrostatic interaction makes up the largest part. It comprises the interaction of all permanent charges and multipoles involved. It is directional and of the longest range. A smaller but significant contribution is a result of charge transfer, which in hydrogen bonding primarily takes place from proton acceptor to proton donor via σ-type interaction [30]. Distortion of the electron distribution usually plays a minor but not negligible role. This so-called polarization interaction covers all effects based on induced multipoles. Short-distance repulsion caused by the overlap of the electron distributions of donor and acceptor usually is referred to as exchange repulsion. Together with electron correlation effects, the latter can be treated as an isotropic van der Waals term. A comprehensive analysis of the energy decomposition of hydrogen bonds was made by Morokuma in 1977 [30, 31].
Hydrogen bonds can be classified as strong, moderate, and weak. According to Jeffrey, strong bonds show energies ranging between 63 kJ/mol and 167 kJ/mol with bond lengths between 1.5 $\mathring{A}$ and 1.2 $\mathring{A}$, bonds with energies between 17 kJ/mol and 63 kJ/mol with corresponding bond lengths between 2.2 $\mathring{A}$ and 1.5 $\mathring{A}$ are referred to as moderate, while bonds with energies below 17 kJ/mol and lengths larger than 2.2 $\mathring{A}$ are called weak [32]. However, there are no well-defined boundaries between these different types of bonding. Moreover, hydrogen bonds can be distinguished by the number of acceptors that a donor interacts with. The bond is called bifurcated when two acceptors are involved and trifurcated when there are three acceptors participating. The formation of hydrogen bonds with more than three acceptors is possible but very rare, because of the required high acceptor density.
Differentiation from other types of binding can be very challenging and often is equivocal. On the low-energy edge, there is a smooth transition to plain van der Waals interaction: Lowering the polarity of X and/or A reduces the electrostatic contribution to the H bond. As a consequence, the directional character changes into an isotropic one and the bond becomes more and more van der Waals-like. At the other end of the scale, in so-called symmetric hydrogen bonds X–H–X, donor and acceptor can no longer be

distinguished and the line between hydrogen bond and covalent bond is blurring. A drastic example is the bifluoride anion $(F–H–F)^-$ with a binding energy of 164 kJ/mol. Comparisons to ionic bonding can be drawn when forming an H bond between two compounds X–H and Y–H with opposite net charge. Here applies: the larger the charges, the more preeminent the ionic character of the bond.

Usually, hydrogen bonds do not appear isolated but as a network. In such interconnected systems, various properties of H bonds are non-additive. This means that one cannot simply sum up the contributions of individual H bonds to describe the whole network. If, for example, an X–H group donates a hydrogen bond X–H$\cdots$A, its polarity is increased. The same holds when it accepts an H bond from an Y–H group. Thus, in a compound Y–H$\cdots$X–H$\cdots$A, both hydrogen bonds become stronger.

Since this thesis first and foremost is concerned with the properties of water and its characteristics as a solvent, the H bonds formed by H_2O are of special interest and will be looked at in more detail. In a water molecule, the oxygen nucleus shows greater affinity to attract binding electrons than the hydrogen nuclei. These different electronegativities lend highly polar character to the covalent O–H bonds and a single water molecule can thus act as H bond donor and acceptor. The energy of the hydrogen bond between the two water molecules of a water dimer is of the order of 20 kJ/mol [33, 34]. However, a key feature of the bonds found in water is the aforementioned cooperativity that can cause H bonds in water to be up to 2.5 times stronger than a single bond in a water dimer [35]. These cooperative effects tend to increase the length of the covalent O–H bond, while the non-covalent hydrogen bond length is shortened, resulting in an overall reduction of the O–O distance [36, 37]. This can be seen when comparing the corresponding O–O distances found for the different physical states of water, which are 2.98 $\mathring{A}$ in the gas-phase dimer, about 2.85 $\mathring{A}$ in liquid water, and 2.75 $\mathring{A}$ in regular ice I_h [8, 38–41]. In pure water, each H_2O molecule can bind up to four neighboring water molecules via four hydrogen bonds, two involving its hydrogen atoms and two between its oxygen atom and the hydrogen atoms of adjacent water molecules. These four binding partners optimally arrange themselves tetrahedrally around the molecule in the middle, like it is the case in ordinary ice I_h. In the liquid phase, thermal energy can elongate, bend, and break hydrogen bonds. Thus, the tetrahedral order is reduced to local clustering. In general, there is a variety of short straight and long bent H bonds in liquid water. Proton magnetic shielding experiments performed by Modig et al. showed that this results in a broad distribution of hydrogen

bond lengths centered around 1.87 $\mathring{A}$ at 0 °C that shifts its center towards higher values and gets broader with increasing temperature [10].
Water oftentimes is referred to as a universal solvent. Indeed, it is able to dissolve more substances than any other liquid. Primarily, polar substances exhibit hydrophilic character and tend to dissipate in water. The water molecules, being polar for their own part, are attracted by the charged particles of the solute and surround them. This formation of a hydration shell goes along with rearranging, reforming, and breaking of hydrogen bonds. A typical example are aqueous salt hydrates as they are discussed in section 2.3. In contrast, water is a poor solvent for hydrophobic, non-polar substances, like lipids. In this case, the hydrogen bond network of the water molecules is reshaped in a way to build a cage-like structure around the respective substance, a process that is called clathration.

2.2 The OH Stretching Vibration as Indirect Probe of H Bonded Systems

The hydrogen bond network of water is subject to constant fluctuations and rearrangements. The respective processes occur on ultrashort timescales ranging from 10 fs to 10 ps [12–14]. Turning to the spectral characteristics, one finds the vibrations associated with the H bond network located in the far-infrared spectral region [42]. The hydrogen bond bending and stretching modes in water were determined to exhibit frequencies around 60 cm^{-1} and 200 cm^{-1} [43–45].[1] This spectral region is hardly accessible for time-resolved spectroscopy. Aggravating this situation, these low-lying excitations overlap with low frequency librational modes[2] and can also be thermally activated within the temperature range applied in this study. A solution to this dilemma is provided by the OH stretching vibration that acts as a sensitive probe for its chemical environment. In liquid water, it is centered in the mid-infrared spectral region around 3400 cm^{-1}.
Steady state absorption spectra of the OH stretching vibration of water and water molecules bound in different hydrate crystals can easily be conducted via conventional spectroscopy, such as Fourier transform infrared (FTIR) spectroscopy. In combination with structure resolving methods, like NMR

[1] The unit cm^{-1} refers to the physical quantity *wavenumber* with the formula symbol $\tilde{\nu}$, which is generally applied to specify energies in infrared spectroscopy. It is calculated as $\tilde{\nu} = \nu/c = 1/\lambda$, where ν is the frequency, c the vacuum speed of light, and λ the wavelength.

[2] In general, a libration is a reciprocating motion of an object with a virtually fixed orientation that slightly rotates back and forth.

and X-ray and neutron scattering, the absorption spectra can be put in relation to geometrical and chemical parameters. A remarkable finding is that the redshift of the OH stretching vibration of water molecules is proportional to the strength of the corresponding H bond. This is commonly known as Badger's Rule and connects the intramolecular bond distance (here: the O–H spacing in a water molecule) to the bond force constant, which itself is directly related to the intramolecular stretching frequency [46, 47]. When considering an elongation of the O–H distance in a water molecule due to the attractive force an H bond acceptor exerts, this will lead to a decrease of the stretching vibration's frequency. By rule of thumb, one can thus say that the stronger the underlying hydrogen bond, the larger the amount of redshift in the corresponding OH stretching vibration and vice versa. Exploiting this relation, the OH stretching vibration can be applied to indirectly probe H bond strengths and the chemical vicinity of the respective water molecules. As the OH stretch frequencies range around 3400 cm^{-1}, they can be directly accessed by mid-infrared pulses generated via optical parametric amplification. Moreover, as shown in section 4.1.3, the thus generated pulses are also suited to resolve the aforementioned ultrafast hydrogen bond dynamics.
Note that in H_2O, the OH stretching vibration is splitting into a symmetric vibration, where the two OH groups are elongated and contracted in phase and an antisymmetric vibration, where the two oscillators are vibrating in counter-phase. This can easily be understood when making some simple quantum mechanical considerations [48]: In an H_2O molecule, two OH oscillators are coupled via a mutual oxygen atom. Applying the Hamiltonian for a degenerate two-level system with a certain degree of coupling yields two normal modes. The associated frequencies are distributed symmetrically around that of the so-called local mode, which represents the natural vibration of an individual OH group. The two normal modes are the above-named symmetric and antisymmetric stretching vibration. When probing hydrogen bonds, this splitting into two vibrational bands can complicate data analysis. That is why it is often preferred to use semi-heavy water (HDO). Since the OD stretch is located around 2500 cm^{-1}, it is far from being in resonance with the OH stretching vibration, which hinders frequency mixing and collective motion. Hence, the local OH stretch mode can be individually accessed, leading to clearer absorption spectra and more explicit data.

2.3 Aqueous Salt Hydrates as New Model System for Confined Water Molecules

In liquid water, a large ensemble of different H bond lengths and angles going along with broken and bifurcated bonds results in a broad and structureless absorption band centered around 3400 cm^{-1}. It is the subject of an ongoing discussion whether this can be explained by a multiplicity of discrete environments of the individual molecules or whether this is due to a stochastic distribution of hydrogen bond strengths without underlying preferred local substructure [11, 49, 50]. In accordance with the previous section, there is a general agreement that the low frequency flank of this band is due to OH oscillators engaged in strong H bonds, while the high frequency side can be traced back to weak hydrogen bonds. Detailed structural investigations in water have been conducted using NMR, X-ray and neutron scattering [6–11]. However, due to the limited time resolution of these methods, a direct correlation between structural features and the ultrafast dynamics is strongly impeded. Complementary measurements were performed, applying more sophisticated techniques, like two-dimensional and three-dimensional IR spectroscopy [51, 52]. Yet, building a bridge to structural features remains challenging and often is based on complicated and not fully unambiguous theoretical calculations and simulations.

A promising ansatz to overcome the problems outlined above was proposed by Iglev et al. in 2009 [18]. Here, exemplified by NaCl dihydrate, aqueous hydrates of inorganic salts were introduced as a new model system for confined water molecules. As the latter are embedded in the salt crystal lattice, individual molecules or small water clusters are distinctly separated from each other and incorporated in well-defined geometrical structures. Chemical environment and degree of confinement can be well adjusted by choosing the appropriate salt. The basic character of the interactions in these samples is generally the same and closely resembles that in bulk water and ice. Despite this commonality, the individual contributions to the total interaction energy can strongly vary in different hydrates, which makes them a suited toolkit to remodel the interactions in water. Usually, hydrates are classified by the number of water molecules per formula unit of the salt and accordingly, one speaks of mono-, di-, and trihydrates. A big advantage is that the crystal structures of a great number of salt hydrates are well-known and documented in accessible databases [20].

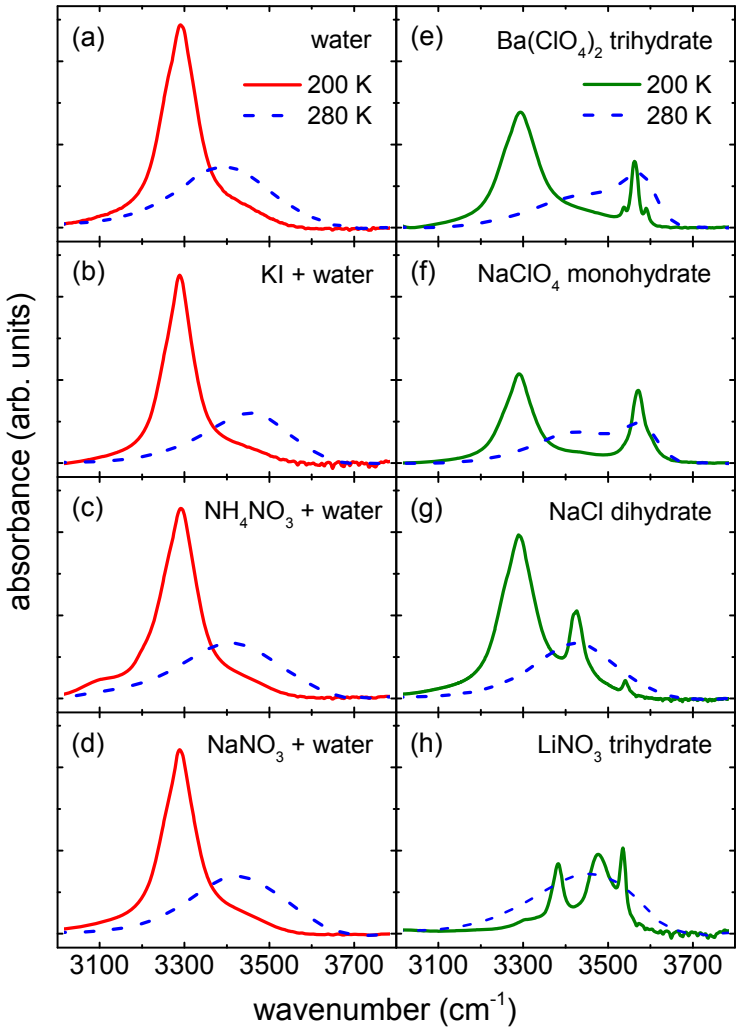

FIGURE 2.1: IR absorption spectra of the OH stretching region in water and seven different water salt solutions. Water here refers to 15M HDO:D_2O. Dashed blue lines are recorded in the liquid phase at 280 K, red and green lines in the crystalline phase at 200 K. Adapted with permission from Ref. [19]. Copyright 2010 American Chemical Society.

Fig. 2.1 shows FTIR spectra of the OH stretching region in water and seven different salts dissolved in water. Water here refers to a solution of 15 molar HDO in D_2O (15M HDO:D_2O). While the spectra of the liquid phase, for the most part, show no significant difference (dashed blue lines), those taken in the crystalline phase at 200 K explicitly reveal whether the salt forms a hydrate or not. The red curves pertaining to water and the water salt mixtures on the left only exhibit one significant peak due to the OH stretching vibration of HDO:D_2O ice around 3300 cm^{-1}. In contrast, in the green lines on the right, new absorption bands emerge, which originate from the OH stretching of the HDO molecules bound in the respective hydrate crystal. Note that besides the hydrate peaks in Figs 2.1 (e-g), the HDO:D_2O ice absorption band

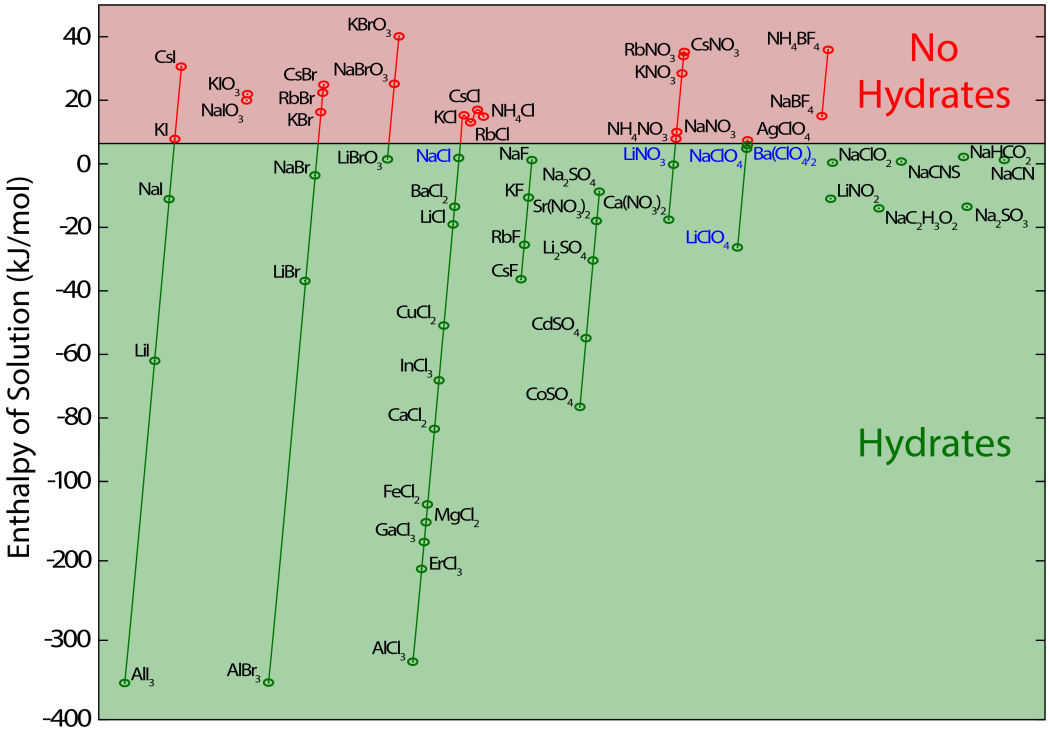

FIGURE 2.2: Graphical representation of the empirical rule of hydrate formation. 60 organic and inorganic salts are sorted by their enthalpies of solution. The threshold value of 6 kJ/mol separates salts that form hydrates (green) from ones that don't (red). Salts that are investigated in the framework of this thesis are highlighted in blue. Adapted with permission from Ref. [19]. Copyright 2010 American Chemical Society.

is still very dominant. This is due to the limited solubility of the salts and gives evidence of polycrystalline samples in which an additional ice phase forms along the hydrate crystal.

A comprehensive prediction of hydrate formation based on thermodynamic parameters is lacking to this day. However, recent studies on 75 organic and inorganic salts that were conducted at our university chair led to a simple empirical rule that links the enthalpy of solution of aqueous salts to their ability to form hydrates [19]. According to these investigations, salts with an enthalpy of solution below a threshold value of 6 kJ/mol form hydrates, whereas salts above this barrier fail to do so. It is evident that this value is very close to the latent heat of ice. Fig. 2.2 illustrates the ability to form hydrates for several salts.

The idea of this work is to start with a simple system and then go to more and more complex ones with pure H_2O ice at the end. The simplest and most fundamental system clearly is one single water molecule. This is an idealized model that can be approached by quasi-isolated water molecules

in $NaClO_4$ monohydrate as it is shown in chapter 5.1. The next step is to include the interaction between individual water molecules in small water clusters, like they can exemplarily be found in $BaClO_4$ trihydrate or $LiNO_3$ trihydrate, respectively (see chapters 5.2 and 5.4). In the end, the intend is to benefit from the great diversity of the hydrate samples by crosschecking the individual results and subsequently putting them in relation to the processes found in neat ice.

Chapter 3

Theoretical Background

In the present chapter, the interaction of light and matter shall be elucidated. For this purpose, a semiclassical approach was chosen. The light field is treated in a classical way based on the Maxwell equations, while the molecule system is referred to as an ensemble of quantum mechanical harmonic oscillators. For a better understanding of the practical chapters, the presented theory will frequently be put in relation to the experimental setup and the actual experiments.

3.1 Electromagnetic Wave Propagation

Bohr's correspondence principle states that systems described by the theory of quantum mechanics reproduce classical physics for large quantum numbers. Considering photons as the excitations of an electromagnetic field, the number of photons can be treated as a quantum number. Hence large photon densities or high electric fields in laser pulses validate a classical treatment based on Maxwell's equations [53]. Presupposing absence of electric currents and free charges in non-magnetic media, these are

$$\vec{\nabla} \cdot \vec{D} = 0 \tag{3.1}$$

$$\vec{\nabla} \cdot \vec{B} = 0 \tag{3.2}$$

$$\vec{\nabla} \times \vec{E} = -\frac{\partial}{\partial t}\vec{B} \tag{3.3}$$

$$\vec{\nabla} \times \vec{B} = \mu_0 \frac{\partial}{\partial t}\vec{D}, \tag{3.4}$$

with μ_0 being the permeability of free space, $\vec{E}$ the electric field, $\vec{B}$ the magnetic field, and $\vec{D}$ the electric displacement.
When penetrating a dielectric material, an electric field forces the positively charged nuclei and their negatively charged electrons to slightly separate and therewith induces a local dipole moment. The electric displacement field

is defined as

$$\vec{D} = \varepsilon_0 \vec{E} + \vec{P}, \tag{3.5}$$

where ε_0 is the vacuum permittivity and $\vec{P}$ the macroscopic polarization. Assuming a linear and instantaneous response of the material to the field $\vec{E}$, the polarization $\vec{P}$ is expressed by

$$\vec{P} = \varepsilon_0 \chi \vec{E}, \tag{3.6}$$

with the so-called electric susceptibility χ being the constant of proportionality. Note that depending on the material, χ may be directional and thus can generally be expressed as a second-rank tensor. Using some vector identities, one can directly derive the electromagnetic wave equation from the Maxwell equations and obtains

$$-\nabla^2 \vec{E} + \mu_0 \frac{\partial^2}{\partial t^2} \vec{D} = -\nabla^2 \vec{E} + \frac{n^2}{c_0^2} \frac{\partial^2}{\partial t^2} \vec{E} = 0. \tag{3.7}$$

Here, $c_0 = 1/\sqrt{\varepsilon_0 \mu_0}$ is the vacuum speed of light and $n = \sqrt{1+\chi}$ the refractive index. A possible solution is a monochromatic plane wave, traveling in the direction of the wave vector $\vec{k}$ that is of the form

$$\vec{E}(\vec{r}, t) = \Re\{\vec{E}_0 e^{-i(\vec{k}\vec{r} - \omega t)}\}, \tag{3.8}$$

where $\vec{E}_0$ is the complex amplitude, $\vec{r}$ the position vector, and ω the angular frequency. Surfaces with constant phase are planes perpendicular to the wave vector $\vec{k}$. They propagate with the phase velocity v_{ph}, and one can define the distance between planes with the same phase as wavelength λ:

$$v_{ph} = \frac{\omega}{|\vec{k}|} = \frac{c_0}{n} \tag{3.9}$$

$$\lambda = \frac{2\pi}{|\vec{k}|} = \frac{2\pi c}{\omega} \tag{3.10}$$

When the light is no longer monochromatic, dispersion, which is the dependence of the wave number $k = |\vec{k}|$ on the frequency ω, becomes relevant. This is important when building a bridge to short laser pulses that can be viewed as wave packages and usually feature broad spectra. For this sake, k can be expanded in a Taylor series in powers of the central frequency ω:

$$k(\omega) = k_0 + \frac{\partial k}{\partial \omega}(\omega - \omega_0) + \frac{1}{2}\frac{\partial^2 k}{\partial \omega^2}(\omega - \omega_0)^2 + ... \tag{3.11}$$

Inspecting the individual terms, the velocity of the wave package is obtained as the inverse of the first derivative of k with respect to ω. It is referred to as group velocity

$$v_{gr} = \frac{\partial \omega}{\partial k}. \tag{3.12}$$

The second order term provides the so-called group velocity dispersion

$$GVD = \frac{\partial^2 k}{\partial w^2} = \frac{\partial}{\partial \omega}\left(\frac{1}{v_{gr}}\right), \tag{3.13}$$

which is the derivative of the inverse of the group velocity and describes the change of the envelope of the laser pulse. In most of the practical cases, the GVD is used as a measure of the chirp, meaning the degree of temporal stretching or compression that a laser pulse experiences when passing through matter.

3.2 Nonlinear Optics

A linear relation between the polarization $\vec{P}$ and the electric field $\vec{E}$ as supposed in Eq. 3.6 no longer holds for high light intensities. Particularly, when $\vec{E}$ is of the same order as the interatomic electric fields, which typically range between 10^5 V/m and 10^8 V/m, a material's response becomes nonlinear and higher orders of $\vec{P}$ have to be taken into account. Historically, the field of nonlinear optics became relevant with the invention of the laser as a source for high light intensities in the mid 20th century. Soon afterwards in 1961, Franken et al. were the first to observe the so-called second harmonic generation, a second order nonlinear process [54].
For a mathematical approach to nonlinear optical effects, the polarization is expanded in a power series of the electric field

$$\vec{P} = \vec{P}^L + \vec{P}^{NL} = \varepsilon_0 \chi^{(1)} \vec{E} + \varepsilon_0 \chi^{(2)} \vec{E}\vec{E} + \varepsilon_0 \chi^{(3)} \vec{E}\vec{E}\vec{E} + ... \tag{3.14}$$

$\vec{P}^L$ represents the part of the polarization that is linear in the electric field and $\vec{P}^{NL}$ the nonlinear one. $\chi^{(1)}$ is the linear susceptibility, $\chi^{(2)}$ is a third-rank tensor and is referred to as second order susceptibility, etc. In general, the nth order nonlinear susceptibility $\chi^{(n)}$ is a $(n+1)$-rank tensor with complex components. The tensor character of the susceptibility reflects the symmetry properties of a material and implies whether a nonlinear effect occurs or not. In matter with inversion symmetry, for instance, the even order susceptibilities equal zero, while the odd order susceptibilities are always symmetry

allowed. A more detailed study of the symmetry relations can, amongst others, be found in the works of Harper and Wherrett [55] or Boyd [56]. Based on Eq. 3.7, one can calculate the nonlinear wave equation

$$\nabla^2 \vec{E} - \frac{n^2}{c_0^2} \frac{\partial^2 \vec{E}}{\partial t^2} = \mu_0 \frac{\partial^2 \vec{P}^{NL}}{\partial t^2}, \tag{3.15}$$

with n being the linear refractive index. As an inhomogeneous wave equation, it describes an electric field $\vec{E}$ driven by the nonlinear polarization $\vec{P}^{NL}$, which can act as a source for new frequency components. For the sake of simplicity, polarization and electric field are treated as scalars subsequently. Considering the response of a lossless medium with non-vanishing second order susceptibility to an incident electric field consisting of two distinct frequencies, ω_1 and ω_2, the following ansatz is made

$$E(t) = E_1 e^{-iw_1 t} + E_2 e^{-iw_2 t} + c.c. \tag{3.16}$$

From this, one derives the second order polarization

$$P^{(2)}(t) = \varepsilon_0 \chi^{(2)} E^2(t) =$$
$$\varepsilon_0 \chi^{(2)} \left[E_1^2 e^{-2i\omega_1 t} + 2E_1 E_2 e^{-i(\omega_1+\omega_2)t} + 2E_1 E_1^* + 2E_1 E_2^* e^{-i(\omega_1-\omega_2)t} + ... \right]. \tag{3.17}$$

The different amplitudes can now be assigned to the underlying physical processes, which are second-harmonic generation (SHG), sum-frequency generation (SFG), difference-frequency generation (DFG), and optical rectification (OR). Taking only positive frequencies into account and assuming $\omega_1 > \omega_2$, the respective amplitudes are

$$\begin{aligned}
P(2\omega_1) &= \varepsilon_0 \chi^{(2)} E_1^2 && \text{(SHG)} \\
P(2\omega_2) &= \varepsilon_0 \chi^{(2)} E_2^2 && \text{(SHG)} \\
P(\omega_1 + \omega_2) &= 2\varepsilon_0 \chi^{(2)} E_1 E_2 && \text{(SFG)} \\
P(\omega_1 - \omega_2) &= 2\varepsilon_0 \chi^{(2)} E_1 E_2^* && \text{(DFG)} \\
P(0) &= 2\varepsilon_0 \chi^{(2)} (E_1 E_1^* + E_2 E_2^*). && \text{(OR)}
\end{aligned} \tag{3.18}$$

Due to dispersion in the nonlinear material, an efficient optical output only can be achieved when the respective phase matching condition is fulfilled:

$$\begin{aligned}
\Delta\vec{k} &= 2\vec{k}_\omega - \vec{k}_{2\omega} = 0 && \text{(SHG)} \\
\Delta\vec{k} &= \vec{k}_{\omega_1} \pm \vec{k}_{\omega_2} - \vec{k}_{\omega_3} = 0 && \text{(SFG, DFG)}
\end{aligned} \tag{3.19}$$

Here, ω_3 represents the sum or difference frequency, respectively. The intensity's dependence on the norm of the wave vector mismatch and the interaction length l is given by the square of a sinc function. It has the form

$$I_{2\omega/\omega_3} \propto \left[\frac{sin(\Delta kl/2)}{\Delta kl/2}\right]^2, \tag{3.20}$$

with its maximum for $\Delta k = 0$ [56]. Typically, phase matching is accomplished by making use of birefringent materials, i.e. materials with a polarization and direction dependent refractive index. In doing so, Δk can be minimized by correctly matching the field polarizations, propagation directions, and crystal orientation.
A detailed analysis of third order nonlinear effects is given elsewhere [55, 56]. Here, only some important examples and relations shall be elucidated. The generation of the third harmonic (THG) can be described in an analogous way to the SHG. Furthermore, third order nonlinearity can lead to an intensity dependent refractive index, a process that is called optical Kerr effect and for its part can evoke self focusing (SF), self phase modulation (SPM), or filamentation that is the propagation of light through a medium without diffraction. These third order processes are essential for the so-called supercontinuum generation (SCG), which is severe spectral broadening of a pump beam in a nonlinear crystal [57]. Note that the latter effect is crucial for the experimental work in this thesis since it lends the used optical parametric amplifiers (OPAs) their excellent spectral tunability (see section 4.1.3).

3.3 Ultrashort Laser Pulses

The laser pulses applied in the time-resolved experiments in chapter 5 are few-cycle mid-infrared (MIR) pulses that feature stable carrier–envelope phase (CEP) and show pulse durations around 50 fs. Pulse duration and CEP stability were verified in frequency optical gating (FROG) and f–2f interferometric measurements (for details see section 4.1.4). For a better understanding and clarification of terms like few-cycle pulse, carrier–envelope phase, and chirp, a comprehensive introduction to ultrashort pulses will be given in this section.
The subsequent considerations follow those made by Diels and Rudolph [58]. As light pulses are electromagnetic wave packages, they can be completely characterized by their time and space dependent electric field $\vec{E}(\vec{r}, t)$. In the following, only the temporal evolution of the electric field, $E(t)$, will

be of interest. For practical reasons, it is recommended to use a complex representation, even though the actually measured signals are real. With the Fourier transform of a real function being hermitian, the real field $E(t)$ can be fully described by its analytic signal $\tilde{E}^{+}(t)$. The latter is a complex valued function that only contains positive frequency components and is comprised of the original function $E(t)$ and its Hilbert transform. It can generally be written as the product of an amplitude function $\varepsilon(t)$ and a phase term with a time dependent phase factor $\Gamma(t)$. Since in most of the practical cases the spectral amplitude spreads around a mean frequency, it is useful to introduce a so-called carrier frequency ω_l that represents the center frequency of the spectral amplitude.[1] Putting all these considerations, together the electric field of a laser pulse can be expressed by

$$\tilde{E}^{+}(t) = \frac{1}{2}\varepsilon(t)e^{i\Gamma(t)} = \frac{1}{2}\varepsilon(t)e^{i\varphi_{CE}}e^{i\varphi(t)}e^{i\omega_l t}, \tag{3.21}$$

with the real field envelope $\varepsilon(t)$ and a time-dependent phase $\varphi(t)$. The constant phase term $e^{\varphi_{CE}}$ represents the carrier–envelope phase that is the offset between the carrier wave oscillating with frequency ω_l and the maximum of the real field envelope. For long pulses consisting of several optical cycles the CEP usually is of minor interest. Nevertheless, it becomes more and more important when entering the regime of few-cycle pulses, where a change in the CEP can lead to a significant change in the maximum field intensity. This can have a crucial impact on the response of the system under investigation. In Fig. 3.1 (a), two exemplary pulses with the same envelope and different CEP are shown (blue and red). With a pulse duration of 30 fs and a carrier frequency that corresponds to a wavelength of 3 μm, the depicted pulses comply with actual Fourier limited probe pulses, as they are characterized in section 4.1.4.

The intensity of a laser pulse by definition is the square of the field envelope $\varepsilon(t)$ and can in many practical cases be well represented by a Gaussian amplitude with its full width at half maximum (FWHM) being a measure of the pulse duration.

Turning to the phase factor $\Gamma(t)$, one deduces the instantaneous frequency of the laser pulse from its first time derivative:

$$\omega(t) = \frac{d}{dt}\Gamma(t) = \omega_l + \frac{d}{dt}\varphi(t) \tag{3.22}$$

[1] Commonly, the carrier frequency ω_l is identified by the frequency at the peak of the laser pulse. An alternative and more accurate definition, however, is provided by the pulse's intensity weighted average frequency.

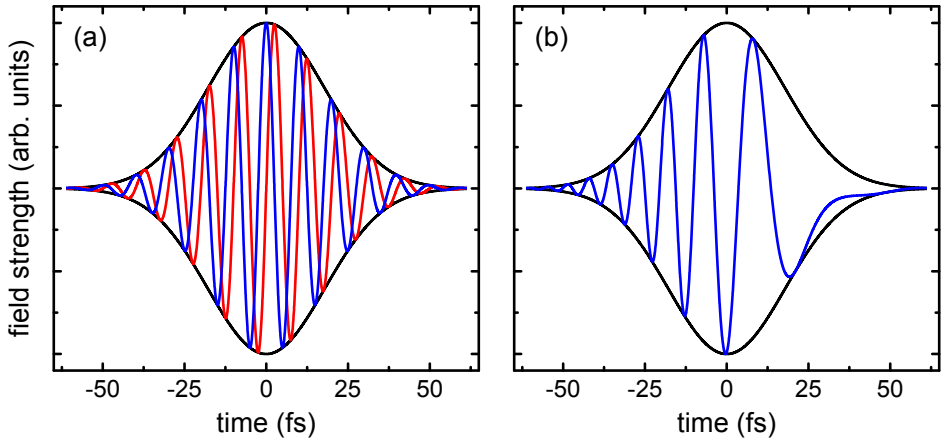

FIGURE 3.1: (a) Two Gaussian pulses with the same pulse form and duration but different CEP (φ_{CE} is 0 for the blue pulse and $\pi/2$ for the red one). (b) Gaussian Pulse that exhibits a linear chirp.

The variation of the instantaneous frequency with time is called chirp. A linearly chirped pulse is displayed in Fig. 3.1 (b). Pulses that exhibit no chirp, i.e. a constant $\frac{d}{dt}\varphi(t)$, are referred to as bandwidth limited or Fourier limited. Here, non-zero but constant $\frac{d}{dt}\varphi(t)$ simply means a linear correction of the carrier frequency.

3.4 The Quantum Harmonic Oscillator

In the experiments shown in chapter 5, laser pulses interact with the OH oscillators of the respective sample. Thereby, each OH group represents a quantum system that in a first approximation can be well described by a quantum mechanical harmonic oscillator. In this picture, the electromagnetic field of the incident laser pulse acts as a time dependent perturbation and can induce transitions between the eigenstates of the system. Apart from slight alterations, the following considerations can be found in any book on quantum mechanics.
In the simplest case of a particle of mass m linked to a body of infinite mass by a spring with spring constant k, the Hamiltonian is given by

$$\hat{H}_0 = \frac{\hat{p}^2}{2m} + \frac{1}{2}k\hat{x}^2, \tag{3.23}$$

with $\hat{p}$ the momentum and $\hat{x}$ the position operator. The eigenstates $|\Phi\rangle$ of the above equation are derived by solving the stationary Schrödinger equation

$$\hat{H}_0 |\Phi\rangle = E |\Phi\rangle . \tag{3.24}$$

The well known eigenstates $\Phi_n(x)$ and corresponding eigenvalues E_n are

$$\Phi_n(x) = A_n H_n(y) e^{-\frac{1}{2}y^2} \tag{3.25}$$

$$E_n = \hbar\omega_0(n + \frac{1}{2}), \tag{3.26}$$

where A_n is a normalization constant, H_n a Hermite polynomial, and y a substituent for $\sqrt{m\omega/\hbar}x$ with ω the angular frequency and $\hbar$ the reduced Planck constant $h/2\pi$. ω_0 equals $\sqrt{k/m}$ and is the resonance frequency of the classical oscillator, and n is the vibrational quantum number. Note that this rather simple approach can be adopted to various different systems, such as diatomic molecules. Considering, for example, an isolated OH group, one can calculate ω_0 by replacing m by the reduced mass μ of the oxygen and hydrogen atoms. Insertion in Eq. 3.26 then yields the respective eigenenergies. Nonetheless, this is an idealized picture that has to be expanded when turning to polyatomic molecules comprising more than two atoms, or when including the coupling of the oscillators to their environment.
As indicated above, transitions between different energy levels that are induced by radiation are handled by adding a time-dependent perturbation $\hat{V}_{int}(t)$ to the Hamiltonian. The time-dependent Schrödinger equation is

$$i\hbar\frac{\partial}{\partial t}\left|\Phi\right\rangle = \hat{H}\left|\Phi\right\rangle = \left[\hat{H}_0 + \hat{V}_{int}(t)\right]\left|\Phi\right\rangle. \tag{3.27}$$

In the dipole approximation, the electric field can be considered to be spatially homogeneous and is of the form

$$\vec{E}(\vec{r},t) = \vec{E}(t) = \vec{E}_0 cos(\omega t) = \frac{1}{2}\vec{E}_0(e^{-i\omega t} + e^{i\omega t}), \tag{3.28}$$

with the vector $\vec{E}_0$ scaling the field strength. One derives the perturbation $\hat{V}_{int}$ to be

$$\hat{V}_{int}(t) = -\vec{\hat{\mu}} \cdot \vec{E}(t) = \hat{V}(e^{-i\omega t} + e^{i\omega t}), \tag{3.29}$$

wherein $\vec{\hat{\mu}}$ is the dipole operator and $\hat{V}$ a time-independent operator that writes

$$\hat{V} = -\frac{1}{2}\vec{\hat{\mu}} \cdot \vec{E}_0. \tag{3.30}$$

The transition rate W_{kl} from state $|l\rangle$ to $|k\rangle$ is given by Fermi's golden rule:

$$\begin{aligned} W_{kl} &= \frac{2\pi}{\hbar^2}|\left\langle k\right|\hat{V}\left|l\right\rangle|^2\left[\delta(\omega_{kl}-\omega)+\delta(\omega_{kl}+\omega)\right] \\ &= \frac{\pi}{2\hbar^2}E_0^2 cos^2(\theta)\mu_{kl}^2\left[\delta(\omega_{kl}-\omega)+\delta(\omega_{kl}+\omega)\right] \end{aligned} \tag{3.31}$$

Here, $\omega_{kl} = (E_k - E_l)/\hbar$ is the transition frequency, and the delta functions ensure resonant excitation. It can immediately be seen that absorption and stimulated emission occur with the same rates. The transition dipole moment $\vec{\mu}_{kl} = |\langle k|\,\vec{\hat{\mu}}\,|l\rangle|$ indicates the strength of an absorbance. With θ being the angle between the latter and the electric field polarization, one clearly sees that only the electric field component parallel to the dipole moment can induce transitions.
For vibrational transitions, the dipole moment operator can be expanded in a Taylor series of the vibrational coordinate x:

$$\vec{\hat{\mu}} = \vec{\mu}_0 + \hat{x}\frac{\partial\vec{\mu}}{\partial x} + ... \tag{3.32}$$

Taking only the first two terms into account and substituting them into Eq. 3.31 under the assumption of resonant excitation yields

$$W_{kl} = \frac{\pi}{2\hbar^2}E_0^2 cos^2(\theta)\left(\frac{\partial\vec{\mu}}{\partial x}\right)^2 |\langle k|\,\hat{x}\,|l\rangle|^2. \tag{3.33}$$

Besides the above mentioned dependence on θ, this expression shows that a vibration is only infrared active when resulting in a change of the dipole moment $\vec{\mu}$. Since this is not the case in symmetric molecules, like O_2 or N_2, the respective vibrations cannot be observed via infrared spectroscopy.
The selection rules in the harmonic approximation are obtained from the matrix element $\langle k|\,\hat{x}\,|l\rangle$. It can be shown that the latter only is non-zero when $l = k\pm1$. This means that only transitions which change the quantum number n by 1 are dipole allowed. However, when adding higher order terms to the interaction Hamiltonian, higher order processes, such as electric quadrupole and octupole transitions, become relevant. In other words, higher multipole moments yield a relaxation of the above selection rule [59]. Furthermore, anharmonicities in the potential, meaning a renunciation from the harmonic approximation, can invalidate the selection rules. Taking the example of a diatomic molecule immediately shows that the harmonic oscillator only provides an approach to many physical systems: On the one hand, the two atoms cannot get arbitrarily close due to repulsive forces of the nuclei, on the other hand, getting too far apart results in dissociation. This behavior can be accounted for by employing an anharmonic potential, such as the Morse potential and leads to a modification of the selection rules and the occurrence of overtones ($\Delta n > 1$).
Note that in anharmonic potentials, the spacing between adjacent energy levels is no longer constant but diminishes when going to higher quantum

numbers. As a result, the transitions $n \rightarrow (n+1)$ occur at different energies for different n and can be observed individually. This can, for example, be seen in chapter 5.1, where the respective transitions of the OH stretch in $NaClO_4$ monohydrate are observed for vibrational quantum numbers n of 0, 1, and 2. One immediately sees that here the anharmonicity of the OH stretching potential is crucial since the spectral and dynamical properties of the individual excitations otherwise could not be investigated separately.

3.5 The Two-Level System

In the previous section, an individual quantum mechanical harmonic oscillator was considered. However, the probed volume in the experiments presented within this thesis consists of a large number of OH groups that can be understood as an ensemble of homogeneous quantum systems. Therefore, it can no more be considered as a pure quantum state but has to be treated as a mixed state that can be characterized using the density matrix formalism [60].
In the following the response of a two-level system to an electromagnetic field is considered. The Hamiltonian of the system is

$$\hat{H} = \hat{H}_0 + \hat{V}(t), \tag{3.34}$$

where $\hat{H}_0$ is the Hamiltonian of the unperturbed system and $\hat{V}(t)$ the energy of interaction with the light field. The two levels are denoted as a and b for the lower and upper level with the associated frequencies ω_a and ω_b and the respective energies

$$E_{a/b} = \hbar\omega_{a/b}. \tag{3.35}$$

As in the previous section, the electric dipole approximation is applied, and the interaction analogously reads

$$\hat{V}(t) = -\hat{\mu}E(t). \tag{3.36}$$

Note that for the sake of simplicity, the vector character in the above equation is omitted. Moreover, only the off-diagonal matrix elements of $\hat{\mu}$ are considered to be non-zero as appropriate for states of definite parity [60]. As the dipole moment operator is hermitian, the non-vanishing elements of $\hat{V}$ are obtained by

$$V_{ba} = V_{ab}^* = -\mu_{ba}E(t). \tag{3.37}$$

For an ensemble of identical systems, the density operator represents the probability that an arbitrary system is in state a or b. It is expressed by the density matrix

$$\hat{\rho} = \begin{pmatrix} \rho_{aa} & \rho_{ab} \\ \rho_{ba} & \rho_{bb} \end{pmatrix}, \tag{3.38}$$

whereby $\rho_{ba} = \rho_{ab}^*$ is valid. The expectation value of any observable A then is expressed by

$$\langle \hat{A} \rangle = tr(\hat{\rho}\hat{A}). \tag{3.39}$$

The time evolution of the density matrix elements is given by the von Neumann equation

$$\frac{\partial \rho_{nm}}{\partial t} = -\frac{i}{\hbar}[\hat{H}, \hat{\rho}]_{nm}. \tag{3.40}$$

Introducing a characteristic time constant T_1 for the decay from the upper level b to the lower level a and a second constant T_2 for the dephasing of the atomic dipole moment leads to the following equations for the off-diagonal and diagonal density matrix elements

$$\frac{\partial \rho_{ba}}{\partial t} = \frac{\partial \rho_{ab}^*}{\partial t} = -\left(\frac{1}{T_2} + i\omega_{ba}\right)\rho_{ba} + \frac{i}{\hbar}V_{ba}(\rho_{bb} - \rho_{aa}) \tag{3.41}$$

$$\frac{\partial \rho_{bb}}{\partial t} = -\frac{\partial \rho_{aa}}{\partial t} = -\frac{\rho_{bb}}{T_1} - \frac{i}{\hbar}(V_{ba}\rho_{ab} - \rho_{ba}V_{ab}), \tag{3.42}$$

with the transition frequency $\omega_{ba} = \omega_b - \omega_a$. Note that the first equality in Eq. 3.42 implies conservation of the total population. Since the diagonal elements of $\hat{\rho}$ represent probabilities of occupation, the sum of ρ_{aa} and ρ_{bb} equals 1.
When the excitation is close to resonance, the rotating wave approximation can be applied, and the interaction is given by

$$V_{ba} = -\frac{1}{2}\mu_{ba}Ee^{-i\omega t}. \tag{3.43}$$

Next, the steady state solutions shall be found. These are the solutions that are valid long after the dynamics due to the turning-on of the driving field have decayed. This is done by introducing a slowly varying quantity σ_{ba} and rewriting the off-diagonal matrix element as

$$\rho_{ba} = \sigma_{ba}(t)e^{-i\omega t}. \tag{3.44}$$

Applying Eq. 3.39 for the dipole moment then yields

$$\langle \hat{\mu} \rangle = \rho_{ba}\mu_{ab} + \rho_{ab}\mu_{ba} = \sigma_{ba}\mu_{ab}e^{-i\omega t} + \sigma_{ab}\mu_{ba}e^{i\omega t}. \tag{3.45}$$

The macroscopic polarization P is given by $N\langle\hat{\mu}\rangle$ with N the number density of quantum systems. Putting all together, one obtains the equations of motion for the macroscopic polarization and the occupation densities ρ_{bb} and ρ_{aa}:

$$\left(\frac{\partial}{\partial t}+\frac{1}{T_2}-i\Delta\right)P^{NL}=\frac{i}{\hbar}N|\mu_{ba}|^2\frac{n^2+2}{3}(\rho_{bb}-\rho_{aa})E \tag{3.46}$$

$$\left(\frac{\partial}{\partial t}+\frac{1}{T_1}\right)\rho_{bb}=\frac{i}{4\hbar N}\frac{n^2+2}{3}(EP^{NL*}-E^*P^{NL}), \tag{3.47}$$

where $\Delta=\omega-\omega_{ba}$. Moreover, a factor $(n^2+2)/3$ with n being the refractive index was included in order to perform a local field correction[2], and hence P was replaced by P^{NL}. When assuming phase relaxation to be fast and therewith T_2 to be small in comparison to the actual pulse durations, Eq. 3.46 can be solved with respect to P^{NL}:

$$P^{NL}=\frac{i}{\hbar}N|\mu_{ba}|^2\frac{n^2+2}{3}(\rho_{bb}-\rho_{aa})ET_2\frac{1+i\Delta T_2}{1+(\Delta T_2)^2} \tag{3.48}$$

The intensity I of an electromagnetic field and the absorption cross section α_0 of the linear transmission for resonant excitation are identified to be

$$I=\frac{1}{2}cn\epsilon_0E^2 \tag{3.49}$$

$$\alpha_0=|\mu_{ba}|^2\frac{\omega T_2}{\hbar nc\epsilon_0}\left(\frac{n^2+2}{3}\right)^2, \tag{3.50}$$

where c is the speed of light, n the refractive index, and ϵ_0 the vacuum permittivity. In consideration of these two quantities, inserting Eq. 3.48 into Eq. 3.47 leads to the following rate equation for the occupation of the two levels

$$\frac{\partial\rho_{bb}}{\partial t}=-\frac{\partial\rho_{aa}}{\partial t}=\frac{I\alpha_0}{\hbar\omega_{ba}}(\rho_{aa}-\rho_{bb})\frac{1}{1+(\Delta T_2)^2}-\frac{\rho_{bb}}{T_1}. \tag{3.51}$$

The expression shows that the transient signals at resonance frequency decay exponentially. Note that in practice, this exponential decay has to be convolved with the temporal shape of the laser pulse.

Applying the slowly varying wave approximation and the above mentioned local field correction, the nonlinear wave equation reads

$$\left(\frac{\partial}{\partial z}+\frac{n}{c_0}\frac{\partial}{\partial t}\right)\vec{E}(z,t)=i\frac{\omega}{2n\epsilon_0c}\frac{n^2+2}{3}\vec{P}^{NL}(z,t). \tag{3.52}$$

[2]The Clausius-Mossotti relation expresses the macroscopically measurable relative permittivity ϵ_r in terms of the microscopic polarizability. In the course of this, the local field is put in relation to the applied external one by $\vec{E}_{local}=\frac{\epsilon_r+2}{3}\vec{E}$. In non-magnetic materials, ϵ_r can be replaced by n^2.

Its derivation can be found in any textbook on nonlinear optics [55, 61]. In consideration of Eq. 3.48, the propagation equation for the intensity can be obtained from the above wave equation:

$$\left(\frac{\partial}{\partial z} + \frac{n}{c_0}\frac{\partial}{\partial t}\right) I = -\frac{1}{2}(\rho_{bb} - \rho_{aa}) \cdot I\alpha_0 \frac{1}{1 + (\Delta T_2)^2} \tag{3.53}$$

Note that the fraction $1/(1 + \Delta T_2)^2)$ corresponds to homogeneous line broadening with a FWHM of $2/T_2$.
In summary, Eqs 3.51 and 3.53 completely describe the excitation and relaxation of a two-level system when assuming constant molecule orientation, which is reasonable for samples in the crystalline phase as they are applied in the present experiments. Eq. 3.51 shows that transient signals recorded at resonance frequency can be approximated by an exponential decay (convolved with the actual pulse shape), while Eq. 3.53 gives evidence of homogeneous line broadening, meaning that transient spectra can be fitted by Lorentzian curves.
Note that in this work, the dynamics of the first excited state usually are observed in the probe beam's transmission at the spectral position of the so-called excited state absorption (ESA), which is the transition from the first to the second excited state. This is done after an excitation pulse has promoted population from the ground to the first excited state. A detailed description of the associated benefits is given in section 4.3.1. Obviously, this measurement principle actually includes three levels. Yet, the measured dynamics still are due to the decay of the first excited state and hence can effectively be described in a two-level picture. In principle, this also holds for the population decay of symmetric and antisymmetric OH stretching in $Ba(ClO_4)_2$ trihydrate presented in chapter 5.2. Nevertheless, the short time dynamics due to population redistribution between symmetric and antisymmetric stretching as well as the quantum beating that is recorded after simultaneous excitation of the latter two vibrations cannot be analyzed applying a two-level picture.
It should also be noted that in liquid water, a dephasing time around 90 fs is reported [62]. The latter is of the same order as the duration of the laser pulses that are applied in this study. Moreover, in the investigated salt hydrates, the OH stretching linewidth is much smaller than in liquid water, which indicates distinctly longer dephasing times. Thus, the assumption of short phase relaxation times yielding Eq. 3.48 no longer holds in the present experiments and the time derivation in Eq. 3.46 usually has to be taken into account.

Chapter 4

Experimental Setup and Measurement Techniques

It was part of the present work to put a new setup for mid-infrared pump–probe spectroscopy into operation and to extend it in order to perform three-color pump–repump–probe experiments. In the following chapter, the setup as a whole and its individual components shall be described in detail. Moreover, a full characterization of the generated mid-IR pulses is given. The complete specifications have been published and can also be looked up in *Optics Express (Vol. 21, Issue 17, 2013)* [63]. Besides the optical setup, the preparation of the crystalline samples is outlined. For a better understanding of the time-resolved experiments, additionally, the principle of the data acquisition of pump–probe and pump–repump–probe measurements is elucidated. Finally, a newly developed alternative setup to perform phase-sensitive spectroscopy along with first proof-of-principle measurements on a GaSb sample are presented.

4.1 Setup

4.1.1 Overview

An overview of the setup is sketched in Fig. 4.1. A Ti:sapphire laser system provides pulses at a wavelength of 779 nm and pulse energies of 1 mJ that are used to pump the three branches for pump, repump, and probe beams. The excitation pulses are generated in two stages of optical parametric amplification (OPA), while the weaker probe pulses are generated in a one-stage system. To obtain the desired excitation conditions (see section 4.3), the pulses are selected by two chopper wheels (CH) that are synchronized to the laser source. Pump and repump can be delayed with respect to the probe pulses by two delay stages (VD), and their bandwidth can be adjusted by two

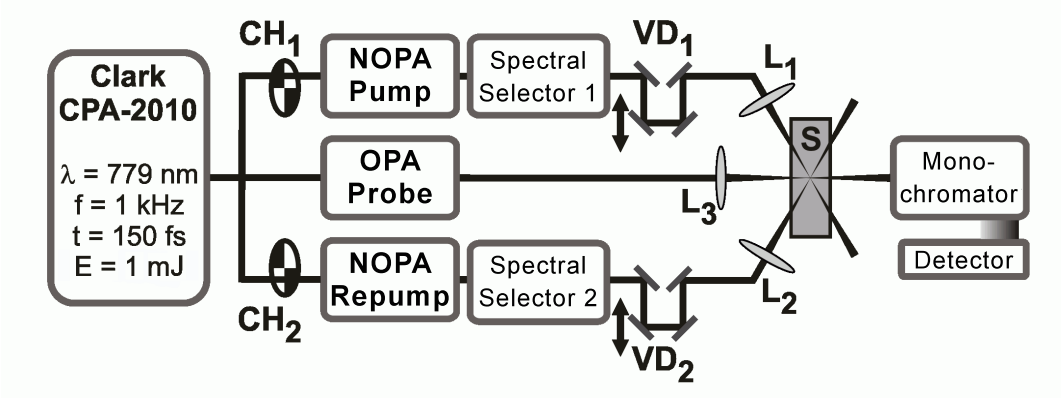

FIGURE 4.1: Schematic representation of the mid-infrared pump–repump–probe setup. CH denote chopper wheels, VD variable delay stages, L are lenses, and S represents the sample. Adapted wih permission from Ref. [63]. Copyright 2013 Optical Society of America.

spectral selectors. The respective polarizations of the individual beams are controlled by broadband half-wave plates, each placed in front of a polarizer. The three pulses are focused onto the sample by three ZnSe lenses (L) with focal lengths of 100 mm for pumping and 75 mm for probing. An estimation of the corresponding spot sizes yields values of roughly 100 μm for the pump beams and 50 μm for the probe. Typically, the investigated samples are available as thin films of about 10 μm to 50 μm thickness, which are crystallized between two CaF_2 windows. The latter are mounted and cooled in a self-made flow-through cuvette that is placed in an evacuated sample chamber in order to avoid the formation of condensation water. A detailed description of the sample preparation can be looked up in section 4.2. After passing through the sample, the transmission of pump and repump beams is detected on two individual HgCdTe sensors, which enables differentiation between the various excitation conditions. The probe pulse's transmission in turn is led to a Czerny-Turner grating monochromator, where it is spectrally resolved and subsequently imaged onto a multichannel detection system consisting of 32 pixels of HgCdTe. At a center wavelength of 3 μm (3333 cm^{-1}), the setup enables shot-by-shot measurement over a bandwidth of scantly 150 nm ($\approx$ 165 cm^{-1}) with a spectral resolution of about 5 nm ($\approx$ 5.5 cm^{-1}).

4.1.2 Laser Source

The laser source that is used to pump the individual OPAs and therefore acts as the workhorse for the whole setup is a Clark-MXR CPA-2010 Ti:sapphire laser system. The pulses originating from an Erbium-doped fiber laser (SErF)

are amplified in a Ti:Sapphire based regenerative amplifier, which is pumped by a frequency-doubled Nd:YAG laser. After internal pulse compression the laser system delivers pulses with a duration of roughly 150 fs at a wavelength of 779 nm and a repetition rate of 1 kHz. With pulse energies of 1 mJ it is suited to run three two-stage noncollinear OPAs (NOPA, pumped by approx. 300 μJ) and one single-stage OPA (pumped by approx. 100μJ) simultaneously.

4.1.3 Generation of Mid-Infrared Pulses

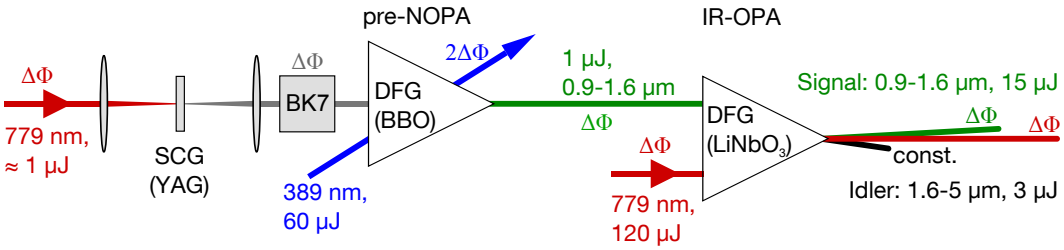

FIGURE 4.2: Setup for the generation of the pump and repump pulses. SCG denotes supercontinuum generation, DFG difference frequency generation, and $n \cdot \Delta\Phi$ depicts the order of the phase fluctuations. Adapted wih permission from Ref. [63]. Copyright 2013 Optical Society of America.

The generation of pump and repump pulses is accomplished in a recently developed hybrid OPA system that delivers femtosecond pulses at the μJ level tunable over a spectral range from about 1 μm to 5 μm. The basic layout can be seen in Fig. 4.2. First of all, a near-infrared (NIR) continuum is generated in 4 mm of yttrium aluminum garnet (YAG). This supercontinuum subsequently seeds a noncollinear stage of OPA. Here, it is amplified in a 2 mm thick beta barium borate crystal (BBO, type I, 32 ° cutting angle) that is pumped by 60 μJ of the second harmonic of the laser light (pre-NOPA). The so generated pulses are of the order of 1 μJ and range in the NIR between 0.9 μm and 1.6 μm. To spatially separate the latter from the pump pulses, a noncollinear setup is chosen for the above DFG process. Note that in this work, the light which is amplified is referred to as signal light and the light that is newly produced as idler light. The NIR pulses subsequently act as seed for a second stage of OPA, where they are further amplified (IR-OPA). In order to make better use of the seed photons, the NIR bandwidth must be matched to the IR-OPA. This is done in the very beginning by introducing a chirp to the supercontinuum by inserting borosilicate (BK7) glass into the beam path. Doing so, the temporal overlap between seed continuum and pump limits the bandwidth of the pre-NOPA. In the IR-OPA,

a linear geometry is chosen to avoid any spatial chirp of the desired idler pulses. It is pumped by 120 μJ of the laser fundamental left over from the second harmonic generation. Via difference frequency generation in a 1.5 mm thick $LiNbO_3$ crystal (type I, 45 ° cutting angle), idler pulses in the MIR are obtained. These range between 1.6 μm and 5 μm and feature typical pulse energies of several μJ. Full characteristics and advantages of this setup have recently been described elsewhere [64].[1]

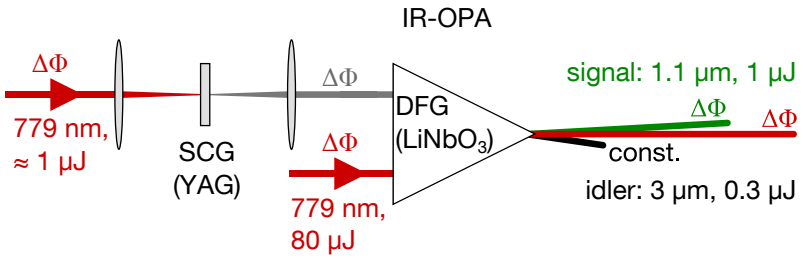

FIGURE 4.3: Scheme of the generation of the probe pulses. SCG denotes supercontinuum generation, DFG difference frequency generation, and $\Delta\Phi$ depicts the phase fluctuation. Adapted wih permission from Ref. [63]. Copyright 2013 Optical Society of America.

The probe pulses are generated in one single stage of OPA (Fig. 4.3). Here again, a collinear setup is chosen to avoid spatial chirp of the idler pulses. As before, a supercontinuum is generated in a 4 mm YAG plate. In order to achieve idler pulses in the MIR, difference frequency generation in a 2 mm thick $LiNbO_3$ crystal (type I, 45° cutting angle) is accomplished by pumping with 80 μJ of the fundamental laser light. This setup allows for the generation of extremely broadband MIR pulses around the desired wavelength of 3 μm. Pulse energies of 0.3 μJ ensure good signal-to-noise ratio.
In order to remove undesired fundamental and signal light from the beam path, Ge filters are placed at the exit of each amplifier.

4.1.4 Pulse Characterization

To perform successful pump–probe experiments, the applied pulses must meet several demands. One basic requirement is that the pulse durations are short enough to ensure adequate time resolution. The latter must be at least of the same order as the fastest dynamics under investigation. To observe a wide spectral range without any readjustments, probe pulses should feature broad spectra. Pump pulses, on the other hand, should be tunable in their

[1] Note that in the setup presented in Ref. [64], not the NIR part of the supercontinuum, but the visible part is amplified in a collinear pre-OPA. Subsequently, the generated NIR idler pulses are applied to seed the IR-OPA.

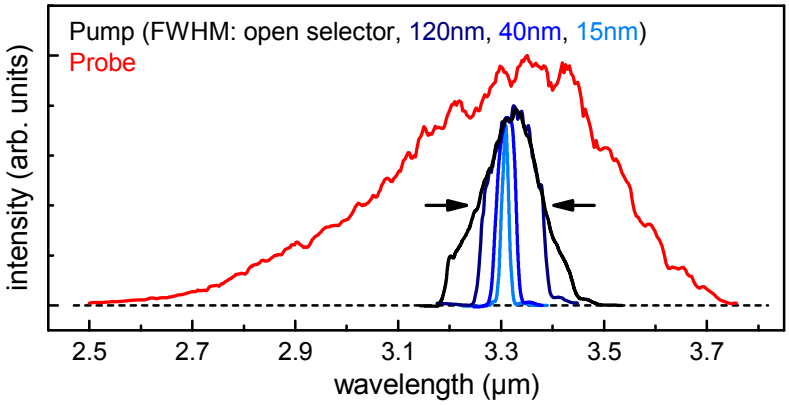

FIGURE 4.4: Pump spectra with different degrees of spectral confinement (black and blue) and a characteristic probe spectrum (red). Adapted wih permission from Ref. [63]. Copyright 2013 Optical Society of America.

center wavelength and bandwidth in order to be suited for an individual excitation of a specific absorption in the vicinity of other absorption bands. The energies of the pulses must ensure good signal-to-noise ratio. Moreover, excitation energies must be high enough to induce measurable changes in the optical density (OD), while probing energies shall be small to prevent inducing commensurable effects in the sample. To make sure that the applied pulses are suited for the actual experiments, they will be fully characterized in the following. Since pump and repump NOPAs have the same layout, only the pump pulses will be analyzed in this section.

An exemplary probe spectrum centered around 3.3 μm ($\approx$ 3 cm^{-1}) with a FWHM of 0.45 μm ($\approx$ 400 cm^{-1}) is depicted in red in Fig. 4.4. Note that the wavelength range that can effectively be employed for transient probing is larger than 1 μm ($\approx$ 1000 cm^{-1}). The bandwidth of the pump spectra can be manually adjusted using a 4f grating spectral selector. By doing so, it can be narrowed down to about 15 nm ($\approx$ 15 cm^{-1}). Respective pump spectra with different degrees of spectral confinement can be seen in Fig. 4.4.

Pulse duration as well as spectral and temporal phase are determined in second harmonic frequency-resolved optical gating (SHG-FROG) measurements. The results obtained for the probe pulses are shown in Fig. 4.5 (a) and (b). At a center wavelength of 3.15 μm, the measurements yield a pulse duration of 45 fs, which corresponds to 4.5 optical cycles. Note that the aforementioned Ge filter at the OPA's exit also is applied for temporal compression of the idler pulses.[2] Here, a thickness of 500 μm was determined to be ideal.

[2]In the course of the DFG, the second and third-order dispersion accumulated in the NIR signal pulses is inverted in the used MIR idler pulses. Hence, these effects can be compensated by materials that exhibit analogous dispersion properties in the MIR as the used nonlinear crystals do in the NIR.

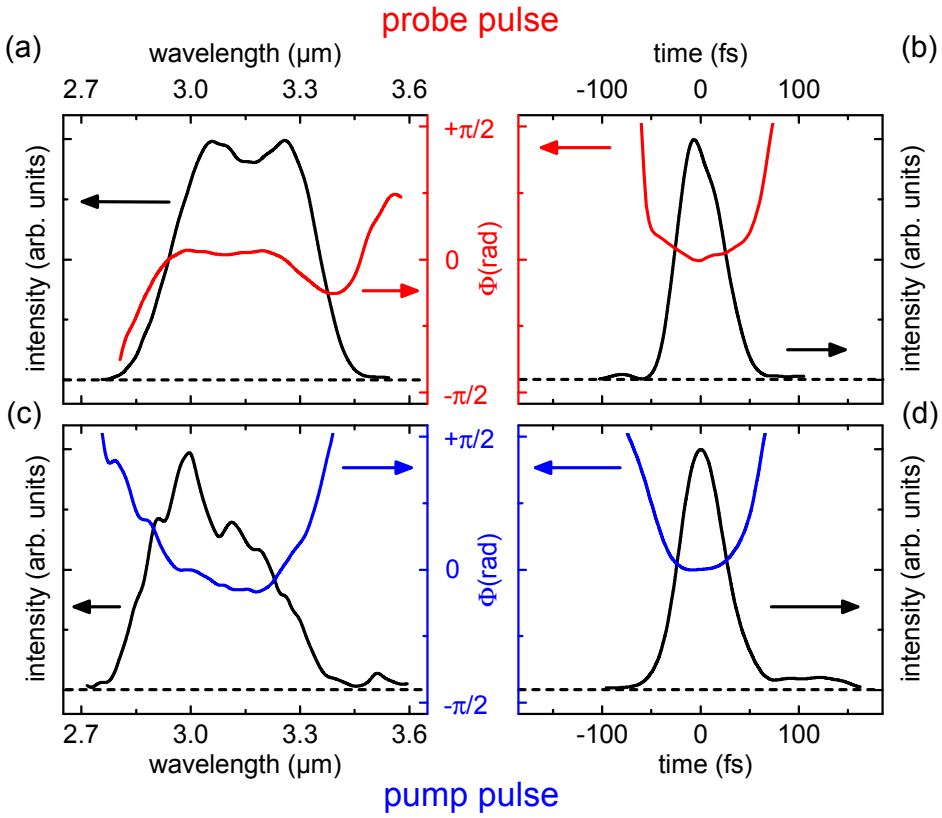

FIGURE 4.5: Results of the SHG-FROG measurements. (a,b) Spectral and temporal intensity profile (black) with the related phases (red) for typical probe pulses. (c,d) Respective profiles (black) and phases (blue) for typical pump pulses. Adapted wih permission from Ref. [63]. Copyright 2013 Optical Society of America.

In view of the almost flat phases in Figs 4.5 (a) and (b), one immediately sees that no further compression is needed. The obtained time–bandwidth product of 0.55 indicates that the pulses are close to the Fourier limit, which would correspond to a pulse duration of 30 fs.

Respective measurements of the pump pulses are shown in Figs 4.5 (c) and (d). These were conducted without passing the spectral selector. At a center wavelength of roughly 3 μm, the pulse duration is 51 fs. Almost flat spectral and temporal phases indicate that the pulses are close to the Fourier limit and exhibit no appreciable chirp. The corresponding time–bandwidth product is 0.52. Additional investigations showed that applying the spectral selector only slightly increases the time–bandwidth product. Nonetheless, spectral narrowing naturally yields longer pulses, which has to be taken into account in actual experiments.

Another pulse property that becomes crucial when applying few-cycle pulses is the carrier–envelope phase. As described in section 3.3, random CEP can lead to strong variations in the maximum electric field. This can decisively

affect the experimental response of a system, especially on timescales of the same order as the pulse duration. Beyond that, there are other aspects making stable CEP worthwhile: Phase stable pump and probe pulses can be applied to perform interferometric experiments and to investigate effects like dephasing or the coupling between different vibrational states. All three MIR pulses of the current setup are few-cycle pulses that show stable CEP. This is remarkable when considering that the driving Ti:sapphire laser system features no CEP stabilization. However, as already indicated in Figs 4.2 and 4.3, all phase changes ($\Delta\Phi$) cancel each other out due to the diverse frequency mixing processes in the amplifiers.

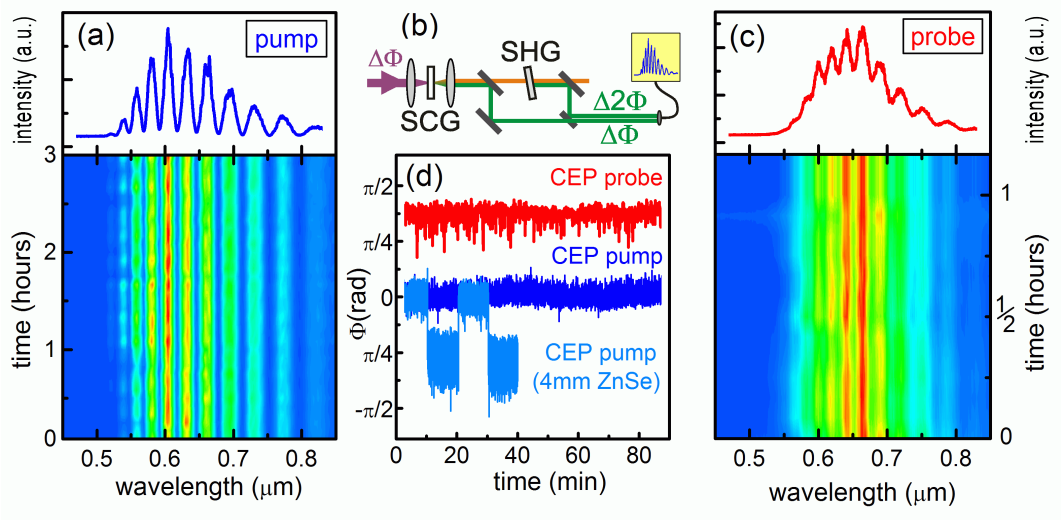

FIGURE 4.6: (a) Exemplary spectrum and long-time interference pattern obtained from the f–2f interferometric measurements of the pump pulses. (c) Respective data for the probe pulses. (b) Principle of the interferometric setup. (d) Temporal evolution of the CEP for pump (blue) and probe (red, up-shifted) pulses. To show the tunability of the pump beam's CEP a 4 mm ZnSe plate was periodically inserted and removed (light blue). Adapted wih permission from Ref. [63]. Copyright 2013 Optical Society of America.

To visualize and verify the phase stability, an f–2f interferometer was set up. The principle is shown in Fig. 4.6 (b). At first the MIR pulses originating from the OPAs are focused into a 4 mm YAG crystal to generate a supercontinuum that ranges from roughly 0.5 μm to 2 μm. In a second step, the 1 μm to 2 μm part of the continuum is frequency doubled in a thin BBO crystal. In the end, fundamental and frequency doubled continua are overlapped in order to generate an interference pattern. The latter is recorded on a fiber-coupled spectrometer. As the original continuum and its second harmonic exhibit different multiples of the phase fluctuation $\Delta\Phi$ ($1\Delta\Phi$ and $2\Delta\Phi$), a lasting interference pattern can only occur when $\Delta\Phi$ equals zero. Thus persistent

interference fringes prove that the pulses feature stable CEP. The spectrum was recorded over a bandwidth from 0.45 μm to 0.85 μm and a time span of 3 hours for the pump (Fig. 4.6 (a)) and 1.2 hours for the probe beam (Fig. 4.6 (c)). In both cases, stable interference patterns were observed. Subsequent Fourier transformation visualizes the spectral phase of the respective pulses. In Fig. 4.6 (d), the temporal evolution of the CEP of the pump and probe pulses is given. For better visualization, the red curve pertaining to the probe pulses is shifted upwards. The standard deviation for the pump pulses is 67 mrad (blue curve) and that of the probe pulses 97 mrad (red curve). To demonstrate the tunability of the CEP, a 4 mm thick ZnSe plate was periodically inserted and removed from the pump beam (light blue curve). With that, CEP stability is verified, and the pulses are fully characterized.

4.2 Sample Preparation

The crystalline samples that are investigated in this thesis are grown by slowly cooling the respective liquid solution between two CaF_2 windows in an evacuated sample chamber. On the one hand, the samples must be thin enough to ensure adequate transmission amplitudes and to minimize stray light, on the other hand, they have to be thick enough to provide a measurable change in the optical density after pump excitation. For this purpose, a sample thickness between 10 μm and 50 μm was found to be optimal. CaF_2 is chosen as window material since it exhibits broadband transmission in a spectral range between 0.2 μm and 8 μm (>90 % at 2 mm thickness). The CaF_2 window pair with the sample in-between is mounted in a homemade cuvette with flow-through temperature control. To prevent the appearance of condensation water on the windows upon cooling, the cuvette is put into an evacuated sample chamber that is again equipped with two CaF_2 windows. For temperatures down to 200 K, a commercial thermostat is used, while lower temperatures can be obtained by circulating liquid nitrogen through the cuvette.
As outlined in section 2.3, due to the limited solubility of the salts, ice forms along the hydrate phase and the samples tend to be polycrystalline (see Figs 2.1 (e-g)).[3] Earlier measurements conducted at our university chair gave evidence that hydrate and ice phases are well separated and can principally

[3]When speaking about solubility in the frame of this thesis, it is generally referred to the molar solubility with the unit mol/l. To compare these solubilities for different salts, it is often advisable to multiply it by the stoichiometric coefficient of the respective salt hydrate (1 for monohydrates, 2 for dihydrates, etc.).

be treated independently. This was concluded from measurements on crystalline NaCl dihydrate, where laser-induced heating of the ice phase did not result in any temperature change in the hydrate phase [18]. However, when investigating the OH stretching of the water molecules bound in the hydrate crystal, spectral overlap with the broad ice absorption band can impede the measurements and complicate data analysis. To minimize its impact, the ice fraction is kept as small as possible by preparing solutions close to the saturation concentration of the respective salt. In principle applies: the higher a salt's solubility and the number of water molecules per formula unit of the hydrate, the smaller the relative proportion of ice.
For an investigation of the OH stretching vibration of HDO molecules, one has to take the appropriate choice of molarities into account. The solvent is obtained from isotopic exchange in a mixture of distinct amounts of H_2O and D_2O. On the one hand, using higher molarities of HDO in D_2O yields higher concentrations of the requested HDO molecules, but, on the other hand, the formation of undesired H_2O is promoted. Depending on the samples under investigation, molarities between 5 and 15 M HDO:D_2O turned out to be most suitable.

4.3 Time-Resolved Spectroscopic Methods

4.3.1 Pump–Probe Principle

Along with the development of ultrafast high-power laser systems, time-resolved pump–probe (PP) spectroscopy became a powerful tool for the observation of ultrafast phenomena in condensed matter. As a technique it was honored in 1999 when Ahmed H. Zewail was awarded with the Nobel prize in chemistry *for his study of the transition states of chemical reactions using femtosecond spectroscopy* [65].
In vibrational pump–probe experiments, an intense pump pulse is applied to populate higher excited vibrational states. The response of the system is monitored in the transmission of a delayed probe pulse that spatially overlaps with the pump in the sample. The probe pulse is of minor intensity and does not cause a noticeable change in the occupation of the system for its part. The pump induced dynamics are displayed in the change of the optical density

$$\Delta OD = -\log\left(\frac{T}{T_0}\right). \tag{4.1}$$

Here, the transmission of the probe beam after excitation by the pump is referred to as T and the transmission with no prior excitation as T_0. Both signals are generated consecutively by applying a chopper wheel that is synchronized with the laser source and blocks every second pump pulse. With the help of a mechanical delay stage, the time evolution of an excitation can be scanned by stepwise altering the pump–probe delay Δt. Thus, the time resolution of a measurement solely is limited by the pulse duration of pump and probe and therefore is sub-100 fs utilizing the pulses characterized in section 4.1.4.

Pulse sequence, energy scheme, and spectrally resolved data generated in a typical PP measurement on the excited states of the OH stretching vibration are shown in Figs 4.7 (a-c). The data is recorded in $NaClO_4$ dissolved in 15 M HDO:D_2O at 200 K. In the following, the vibrational states of the OH stretching vibration are denoted by ν_n with n their quantum number and transitions from state n to m are labeled as ν_{nm}. An intense pump pulse is applied to promote population into the ν_1 state. The corresponding ΔOD signal at a pump–probe delay of 0.8 ps is depicted in blue in Fig. 4.7 (c). Two main features are visible: One is a ground state bleaching (GSB) at ν_{01} that is due to a depletion of ν_0 and the associated weaker absorption of the probe pulse. The second is an excited state absorption at ν_{12} (ESA_{12}) that is observed in the probe beam's transmission after ν_1 was populated by the pump. Thanks to the relatively strong anharmonicity of the OH stretching potential, both features are spectrally well separated and can be observed individually.

Besides the desired signals due to the population dynamics, other effects can occur in pump–probe measurements and oftentimes complicate data analysis. In many experiments, the observed absorption bands exhibit temperature-dependent shape. Since the ΔOD signal can be interpreted as the difference between the probe beam's transmission through an excited (warm) and an unexcited (cold) sample, temperature dependent changes in the absorption bands yield characteristic features in the measured data.[4] In the investigated crystalline aqueous samples, these temperature effects usually build up within the first few picoseconds after excitation and are present on a nanosecond timescale. Note that the sample temperature completely recovers within the time frame between two probe pulses (1 ms) and that therefore

[4]Temperature dependent effects can also be consulted as thermometer and manometer for hydrogen bonded systems [66]. In 2005, Iglev et al. utilized the characteristic shape of the temperature dependent absorption changes of the OH stretching in HDO to demonstrate ultrafast superheating of bulk ice [67].

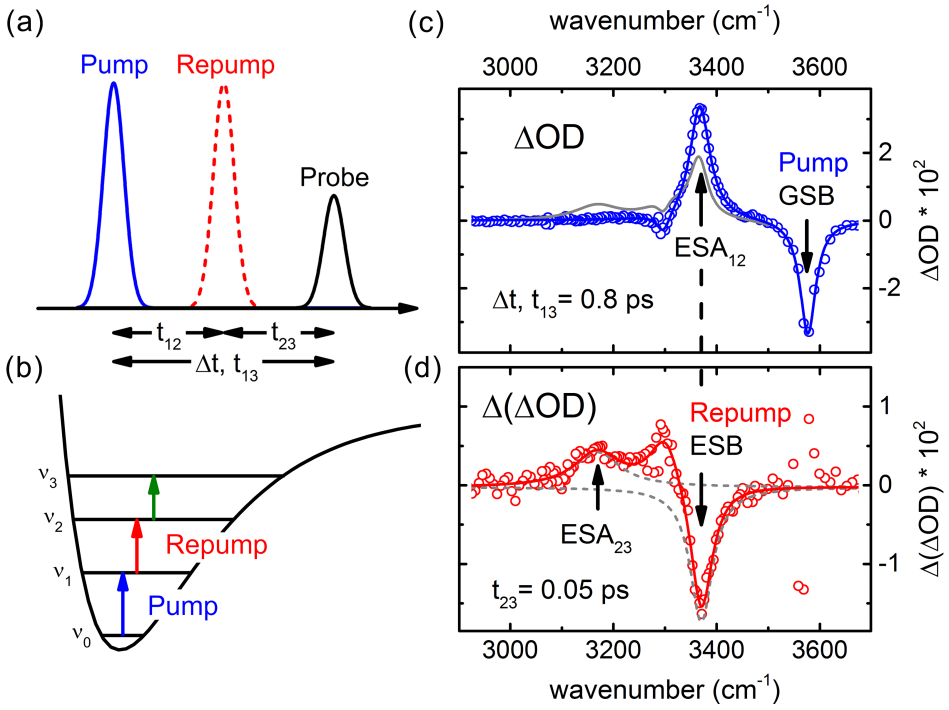

FIGURE 4.7: (a) Pulse sequence and (b) excitation scheme in PP and PREP experiments. (c) Raw data points and fit of the ΔOD signal recorded in $NaClO_4$ dissolved in 15M HDO:D_2O at 200 K for a pump–probe delay of 0.8 ps (blue). The respective ΔOD_{PuRe} signal measured 50 fs after repumping ($t_{12} = 0.75$ ps, $t_{23} = 0.05$ ps) is depicted in gray. (d) Corresponding $\Delta(\Delta OD)$ signal. ESB and ESA_{23} were approximated by Lorentzian functions (dashed gray).

no long-time heating of the sample is observed. The latter can easily be proven by checking for absorption changes at negative pump–probe delays. Nevertheless, especially during their build-up, temperature effects can result in ambiguous data and have to be accounted for when investigating population dynamics.

Another recurring phenomenon in pump–probe measurements is the occurrence of so-called coherent artifacts around zero delay. Generally, when pump and probe pulses are generated from the same laser pulse, their mutual coherence can give rise to a coherence spike in the ΔOD signal. This is a well-known feature and persistent subject of discussion. Most commonly, it is explained by spatial fluctuations in the excited state population, which are induced by the interference of the pump and probe beams in the region of overlap in the sample [68, 69]. This spatial variation can act as a diffraction grating for the pump and probe photons. Thereby, pump stray light that is deflected into the probe's beam path results in a negative contribution to the ΔOD signal, while probe light strayed out of its actual beam path yields a positive signal. However, besides this explanation, several other mechanisms

that can contribute to the coherence spike are suggested. A prominent example is the build-up of a phase grating due to a modulation of the refractive index [70]. Detailed model calculations performed by Balk et al. put the coherence spike in relation to the dephasing time T_2 [71]. They state that the artifact's sensitivity to T_2 strongly depends on the pulse durations and that T_2 can be extracted from the experimental data when it is comparable or larger than the time resolution.
In order to diminish the above described coherent effects in actual experiments, signal processing in the ESA is preferred to data acquisition in the GSB. By doing so, pump and probed wavelengths are separated and the influence of coherent artifacts is strongly suppressed since they are favored by spectral overlap. Another advantage is that different pump and probe frequencies ensure that no pump stray light that was deflected into the probe beam path hits the detector since it does not pass the monochromator.

4.3.2 Pump–Repump–Probe Principle

Besides the standard pump–probe scheme, the setup presented in section 4.1 offers a third pulse for secondary excitation. The so-called repump pulse equals the pump pulse and is individually tunable in its wavelength. It traverses its own delay stage and therefore extends the parameter space by one dimension. The respective delay times are denoted by t_{12} for pump–repump, t_{13} for pump–probe, and t_{23} for repump–probe delay. A second chopper wheel working at half the frequency of the one in the pump beam path alternately blocks and lets pass two successive repump pulses. This configuration enables the generation of four different excitation conditions: no excitation (T_{00}), pump only (T_{10}), repump only (T_{01}), and excitation by pump and repump (T_{11}). The signal of special interest is the $\Delta(\Delta OD)$ signal that reflects the pure impact repumping has when there was prior excitation by the pump, whereby the standalone pump–probe and repump–probe effects do not contribute. It can be written as

$$\begin{aligned}\Delta(\Delta OD) &= -\left[\log\left(\frac{T_{11}}{T_{00}}\right) - \left(\log\left(\frac{T_{10}}{T_{00}}\right) + \log\left(\frac{T_{01}}{T_{00}}\right)\right)\right] = \\ &= -\left[\log\left(\frac{T_{11}}{T_{01}}\right) - \log\left(\frac{T_{10}}{T_{00}}\right)\right] = \Delta OD_{PuRe} - \Delta OD = \\ &= -\log\left(\frac{T_{11}\cdot T_{00}}{T_{10}\cdot T_{01}}\right). \end{aligned} \tag{4.2}$$

Here, ΔOD_{PuRe} is the probe beam's absorption change after two-pulse excitation corrected for effects caused by excitation by the repump only and ΔOD the standard pump–probe signal. Similar data processing was already used by Buback et al. [72]. While pump–repump–probe (PREP) so far mainly concentrated on UV pump and repumping in the visible [72, 73], in chapter 5.1, first purely vibrational PREP experiments are presented. The measuring principle shall be elucidated in the following.

In vibrational PREP, a sequence of excitation pulses is applied to successively populate higher states. The respective pulse series and excitations are schematically drawn in Figs 4.7 (a) and (b). A delayed repump pulse is able to populate the second excited state of the OH stretching potential after population was promoted into the first excited state by the pump. In the experiments performed within the framework of this thesis, the peak intensities of both excitation pulses are roughly 250 GW/cm^2 and thus high enough to generate a measurable occupation in the ν_2 level. The associated features in the $\Delta(\Delta OD)$ signal are very similar to those of the PP measurements but up-shifted by one vibrational quantum number. An excited state bleaching (ESB) is observed at ν_{12} after the first excited state is depopulated by the repump pulse, and a second excited state absorption (ESA_{23}) occurs at ν_{23} after ν_2 was populated. The respective data recorded in crystalline $NaClO_4$ in 15M HDO:D_2O are shown in Figs 4.7 (c) and (d). According to Eq. 4.2, subtracting the ΔOD_{PuRe} (gray) from the ΔOD signal (blue) in Fig. (c) delivers the $\Delta(\Delta OD)$ signal shown in Fig. (d). ESB and ESA_{23} are well apparent and clearly separated due to the potential's anharmonicity. Sample specific additional artifacts like the one around 3300 cm^{-1} and a stray signal at the position of the ν_{01} transition will be explained in full detail in chapter 5.1.

Note that besides the above procedure, one could also imagine reaching highly excited states with only one spectrally broad excitation pulse. This was successfully demonstrated by pumping the weakly anharmonic vibrational ladder of the CO stretching [74–76]. However, the strong anharmonicity of the potentials on hand and the limited spectral bandwidth of the pump pulses strongly hinders this modality in the case of the OH stretching. Moreover, the utilization of a second repump pulse offers an additional degree of freedom and more control over the individual excitations. With three individually tunable pulses, PREP can generally be classified as fifth-order technique. Apart from that, if both excitation pulses are temporally separated, i.e. exhibit a delay longer than the dephasing time, it can also be thought of as a cascade of pump–probe experiments. These assumptions

are in good accordance with observations made for stimulated 2D Raman spectroscopy [77–80]. The measurements on the OH stretching overtones in $NaClO_4$ monohydrate presented in chapter 5.1 show that PREP is able to reach highly excited states of the OH stretching vibration and can even elucidate ordinarily covert relaxation channels. At the same time, it provides a signal-to-noise ratio comparable to that of standard pump–probe experiments.

4.3.3 Transient Absorption Phase-Sensitive Spectroscopy

Compared to femtosecond pump–probe spectroscopy, which made great progress in the past decades, femtosecond phase spectroscopy still is in its infancy. However, knowledge about the transient phase evolution is crucial for fully understanding a system's properties. Besides a direct measurement of the change in the refractive index that a sample undergoes upon excitation, there is a vast number of coherent effects that can be illuminated by analyzing the transient phase dynamics [81–83]. Generally, these coherent effects are identified by the off-diagonal elements of the density matrix, whose dynamics are dominated by the dephasing time T_2 (see section 3.5). As the diagonal matrix elements that reflect the pure population dynamics of the different states can be determined by standard pump–probe spectroscopy, a combination of both techniques yields the full information that is required to completely describe a given system. Here, a novel setup for time-resolved transient absorption phase-sensitive (TAPS) spectroscopy is presented that merges spectral interferometry and IR pump–probe spectroscopy.
The experimental assembly is shown in Fig. 4.8. Being based on the above described setup, the specific pulse characteristics can be looked up in section 4.1. Again, the pump and probe beam paths intersect at the sample position. The third beam, however, is no more used for excitation but as a reference. It is guided around the sample chamber to a CaF_2 beamsplitter, where a small part of it is reflected into the probe beam path. Subsequently, the transmitted probe beam and the reflex of the reference beam collinearly traverse the monochromator, where they are spectrally dispersed and guided to the detection system. The relative delay between probe and reference pulses can be adapted by a variable delay stage in the reference beam path. When temporal and spatial overlap at the detector is achieved, the two pulses generate an interference pattern in the region of spectral overlap. With the chopper wheels running at the same frequencies as in the PREP experiments,

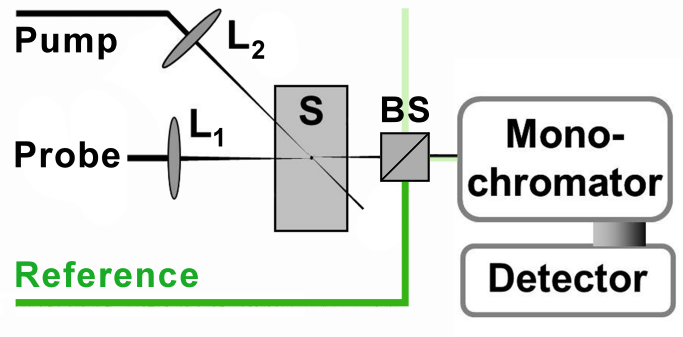

FIGURE 4.8: Schematic representation of the TAPS setup. The standard pump–probe configuration is expanded by an additional reference beam (green) that is guided around the sample chamber and coupled into the spectrometer via a beam splitter BS. L denote lenses, and S represents the sample.

again four different signals are detected: probe transmission without excitation and reference (T_0), with excitation and no reference (T_{ex}), with reference and no excitation (T_{ref}), and with both, excitation and reference ($T_{ex,ref}$). In this way, the background-corrected interference patterns with ($T_{ex,ref} - T_{ex}$) and without pump excitation ($T_{ref} - T_0$) and a standard pump–probe signal ($\Delta OD = -log(T_{ex}/T_0)$), which is not overlaid with any reference signal, can be monitored in one single measurement. The interference picture is spread over a bandwidth of roughly 150 nm on the 32 pixels of the multichannel detector.

In a proof-of-principle measurement, the change in the refractive index of an n-type gallium antimonide (GaSb) sample upon excitation of electrons into the conduction band shall be determined. The band gap of GaSb at room temperature is 0.726 eV, which corresponds to a wavelength of roughly 1.7 μm. Via two-photon absorption, a pump pulse centered around 3 μm is capable of promoting electrons from the valence into the conduction band. These excited electrons are able to absorb photons of a delayed probe pulse. The time-dependent absorption change in the probe transmission at 3 μm is reflected in the ΔOD signal shown in Fig. 4.9 (a) (black line). Fig 4.9 (b) shows the associated interference patterns with (red) and without (blue) excitation for different pump–probe delays τ and fixed reference–probe delay T. One immediately sees that excitation leads to a shift of the spectral phase at positive delays. The amount of phase shift $\Delta\Phi$ was extracted by fitting cosine functions to the data and subsequently calculating the phase difference.[5] The temporal evolution of $\Delta\Phi$ is depicted in green in Fig. 4.9 (a). As one can

[5]In a first series of fits, the average oscillation period was determined to be 41,9 nm. In a second series, this value was applied as constant in order to obtain consistent results.

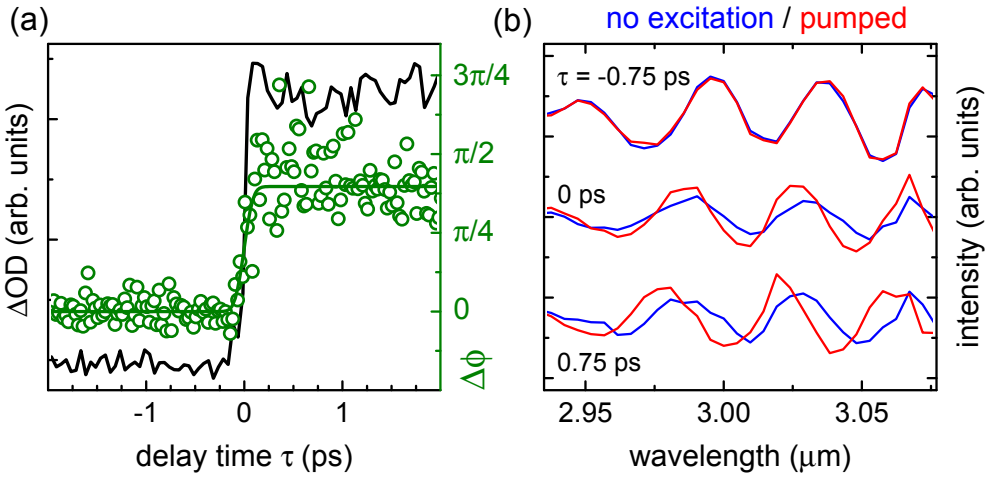

FIGURE 4.9: (a) Change in the transient absorption of a GaSb sample after pump-induced excitation of electrons from the valence into the conduction band (black) and time evolution of the phase change in the associated interference patterns (green). (b) Stacked interference patterns with (red) and without (blue) excitation for different pump–probe delays and fixed reference–probe delay.

see, the phase shift exhibits similar dynamics as the ΔOD signal and peaks around $3/8\ \pi$.

In the following, the induced change in the refractive index shall be extracted. The considerations are in accordance with those made by Tokunaga et al. [81]. The electric field of a probe pulse propagating through a medium can be generally expressed by

$$E'_{pr}(t) = \frac{1}{2\pi}\int d\omega E(\omega-\omega_0)\times e^{i\omega(t-n_c(\omega)x/c)}, \tag{4.3}$$

with $E(\omega)$ being an arbitrary complex function, ω_0 the center frequency, c the speed of light, x the thickness of the medium, and $n_c(\omega) = n(\omega) - ik(\omega)$ its complex refractive index. The Fourier transform of this equation is

$$E'_{pr}(\omega) = E(\omega-\omega_0)e^{-in_c(\omega)\omega x/c}. \tag{4.4}$$

Experimentally, the Fourier transformation is executed by the spectrometer grating. For a reference–probe delay T, one can write the measured interference signal (without excitation) as

$$|E'_{pr}(\omega)+E'_{ref}(\omega)|^2 \propto I_{pr}(\omega)+I_{ref}(\omega)+2\sqrt{I_{pr}(\omega)I_{ref}(\omega)}cos(\omega T), \tag{4.5}$$

where $E'_{ref}(\omega)$ is the field of the reference pulse and $I_{pr}(\omega)$ and $I_{ref}(\omega)$ are the individual pulse intensities. At positive pump–probe delays τ, pump

excitation induces a change in the complex refractive index of the GaSb sample:

$$\Delta n_c(\omega,\tau) = \Delta n(\omega,\tau) - i\Delta k(\omega,\tau) \tag{4.6}$$

With this, the field of a delayed probe pulse that is transmitted through an excited sample writes

$$E'_{pr}(\omega,\tau) = E'_{pr}(\omega)e^{-i\Delta n_c(\omega,\tau)\omega x/c}. \tag{4.7}$$

The respective interference signal measured after pump excitation can then be expressed by

$$\begin{aligned} |E'_{pr}(\omega,\tau) + E'_{ref}(\omega)|^2 \propto I_{pr}(\omega)e^{-2\Delta k(\omega,\tau)\omega x/c} + I_{ref}(\omega) + \\ +2\sqrt{I_{pr}(\omega)I_{ref}(\omega)}e^{-\Delta k(\omega,\tau)\omega x/c} \cdot cos(\omega T - \Delta n(\omega,\tau)\omega x/c). \end{aligned} \tag{4.8}$$

Now, the change in the real part of the refractive index can be obtained by comparing the arguments of the cosine functions in Eqs. 4.5 and 4.8. One immediately sees that

$$\Delta\Phi = \Delta n(\omega,\tau)\omega x/c. \tag{4.9}$$

With a sample thickness of (500 $\pm$ 50) μm at a center wavelength of 3 μm and the above phase shift of 3/8 π, Δn amounts to approximately 0.1 %.
These measurements and data analysis prove the functionality of the TAPS setup and demonstrate its capability to yield highly precise data. Note that the transient phase dynamics can be monitored with a temporal precision that is no more limited by the pulse duration, but only by the carrier wavelength. Being of the same order as the duration of one optical cycle, the effective time resolution at a center wavelength of 3 μm is roughly 10 fs. The smallest measurable phase change is mainly limited by the number of detector pixels. When tuning the reference–probe delay in a way that at least one period of the interference pattern is depicted on the 32 pixels, the resolution can be estimated to 1/16 π, which corresponds to a change in the refractive index of about 0.02 % at 3 μm. For future measurements it is recommended to apply a detection system that offers more pixels in order to improve the precision. This is particularly important when considering the small phase changes that are expected after vibrational excitation [84].

Chapter 5

Measurements on Hydrogen Bonded Systems

5.1 Relaxation of the OH Stretching Overtones in Isolated HDO Molecules in $NaClO_4$ Monohydrate

The following studies on the overtones of the OH stretching vibration of isolated HDO molecules in sodium perchlorate ($NaClO_4$) monohydrate were published in *The Journal of Physical Chemistry A* in 2015 [85]. Being the very first measurements with the newly developed setup for IR pump–repump–probe spectroscopy, the data can be consulted as proof of its functionality and expediency in yielding new and valuable information on hydrogen bonded systems.
As discussed in section 2.3, aqueous salt hydrates are the ideal model system for confined water molecules in defined geometrical environments. Here, $NaClO_4$ monohydrate is a prototypical example. Due to its unique crystal structure, it provides a means to investigate quasi-isolated water molecules.

5.1.1 Crystal Structure and Absorption Spectrum

The sample is obtained by slowly cooling a saturated solution of $NaClO_4$ dissolved in 15 M HDO:D_2O. In the present chapter, water will always refer to the latter isotopic mixture. The crystal structure of the hydrate sample is well-known from X-ray and neutron diffraction studies [86, 87]. It forms a monoclinic crystal of space group *C2/c*, which is shown in Fig. 5.1 (a). Water molecules are electrostatically bound to Na^+ cations via the oxygens' lone pairs[1]. Very weak bifurcated hydrogen bonds are formed between an OH

[1] A water molecule's oxygen atom can be described as having four, approximately tetrahedrally arranged, sp^3-hybridized electron pairs: two associated with covalent bonds to the hydrogen atoms and two lone pairs.

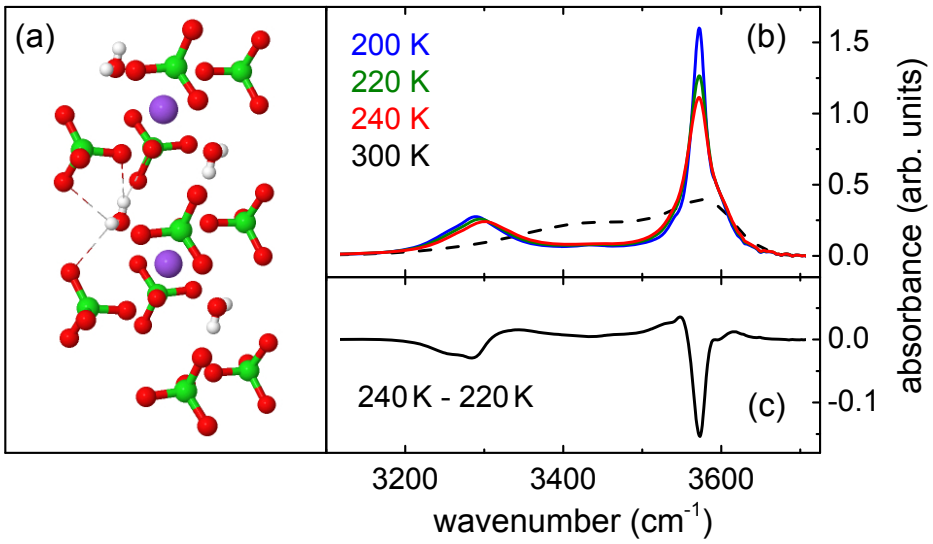

FIGURE 5.1: (a) Crystal structure of $NaClO_4$ monohydrate (Cl in green, H in white, Na in purple, and O in red). Hydrogen bonds are indicated by dashed lines. (b) FTIR absorption spectra of $NaClO_4$ in 15 M HDO:D_2O measured at different temperatures in the liquid (300K) and solid phase. The pronounced peak at 3575 cm^{-1} is due to the water molecules bound in the hydrate crystal, while the minor feature around 3300 cm^{-1} stems from an additional ice phase in the sample. (c) Differential spectrum representing the absorption change for a temperature jump from 220 K to 240 K. Adapted with permission from Ref. [85]. Copyright 2015 American Chemical Society.

group and two oxygen atoms of adjacent ClO_4^- anions. The water molecules are distinctly separated by perchlorate anions, which yields a closest O–O distance of 440 pm between two water molecules. For comparison, the respective value in hexagonal ice is 275 pm. Note that the spacing between the actually investigated OH groups is even larger since in the applied isotopic mixture of 15 M HDO:D_2O, on average, only one of four water molecules contains a hydrogen atom. Thus, one can in fact consider the investigated water molecules as quasi-isolated.

Associated FTIR measurements are displayed in Fig. 5.1 (b). The spectra exhibit two distinct absorption bands in the OH stretching region, which pertain to separate ice and hydrate phases. Due to the relatively high solubility of sodium perchlorate, the hydrate peak at 3575 cm^{-1} is much more pronounced than the well-known ice band around 3300 cm^{-1}. Small shoulders in the hydrate peak can be assigned to a little contamination with H_2O. The FWHMs of the features are 21 cm^{-1} for the hydrate and 93 cm^{-1} for the ice absorption (at 200 K). According to the findings in section 2.2, the large amount of blueshift of the hydrate band relative to the ice absorption gives

evidence of very weak H bonds formed by the hydrate water molecules. When going to lower temperatures, the amplitude of the hydrate peak significantly rises, while the amplitude of the ice absorption shows a much lower increase, which is accompanied by a nearly linear shift of the peak maximum to smaller energies. The same behavior of the ice band was already observed in earlier studies [67]. In Fig. 5.1 (c), a thermal differential spectrum for a temperature jump from 220 K to 240 K is given. It reveals two characteristic features at the positions of the ice and hydrate absorptions.

5.1.2 Applying IR Pump–Repump–Probe Spectroscopy to Climb the Vibrational Ladder

The following time-resolved data was recorded at a sample temperature of 200 K. To avoid spectral overlap between pump and repump pulses, the pump spectrum was narrowed to 90 cm^{-1} with the help of the aforementioned spectral selector. Thus, the overall time resolution is reduced to slightly less than 200 fs. Transient pump–probe spectra measured after excitation in the maximum of the fundamental hydrate absorption band are shown in Figs 5.2 (a-c). The ΔOD signal monitored 0.8 ps and 2.75 ps after excitation exhibits the two features discussed in section 4.3.1: a ground state bleaching (GSB) at (3575 $\pm$ 3) cm^{-1} and an excited state absorption (ESA) at ν_{12} that is spectrally shifted to (3370 $\pm$ 3) cm^{-1} due to the anharmonicity of the OH stretching mode. With a FWHM of (48 $\pm$ 3) cm^{-1}, the ESA is considerably broader than the GSB that features a width of (37 $\pm$ 3) cm^{-1}. The absorption changes that remain 50.75 ps after excitation are in qualitative agreement to the thermal differential spectra in Fig. 5.1 (c) and hence can be ascribed to transient heating of the sample by the pump beam. Since laser-induced heating happens at constant volume, it results in a pressure increase in the illuminated sample volume [66, 67, 88] leading to small deviations between steady-state and transient differential data. Nevertheless, the smaller amplitude in the pump–probe data implies a much lower temperature jump that was determined to be about 4 K.

Time-resolved dynamics recorded in the maximum of the ESA at 3370 cm^{-1} are plotted in Fig. 5.3 (a). The transient's evolution is dominated by a monoexponential decay with a time constant that was fitted to be (9 $\pm$ 2) ps.[2]

[2]Note that this relaxation time was corrected with respect to the value of 7.2 ps given in [85]. Newly measured data yielded distinctly longer lifetimes. The deviating time constants may be due to two different phases in the $NaClO_4$ hydrate samples. The lifetime thus was corrected to 9 ps and the error was deliberately increased.

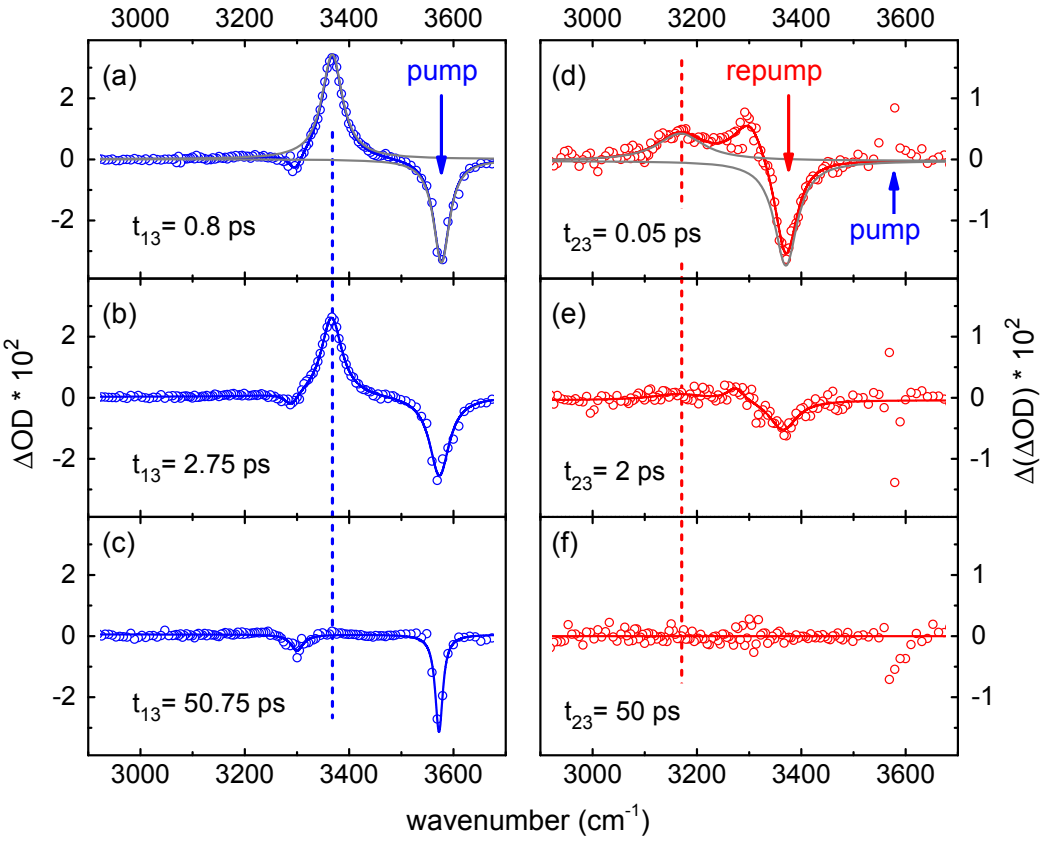

FIGURE 5.2: (a-c) Transient pump–probe spectra recorded after excitation of the ν_{01} transition for three different pump–probe delay times t_{13}. The data displays two main features: a GSB at 3575 cm^{-1} and an ESA at 3370 cm^{-1}. (d-f) Transient PREP spectra monitored after pumping at ν_{01} and repumping at ν_{12}. The pump–repump delay t_{12} is fixed at 0.75 ps, while the repump–probe delay t_{23} is varied. The data shows a bleaching of the excited state absorption at ν_{12} and a second ESA at the ν_{23} transition at 3170 cm^{-1}. Measured data is displayed as circles and corresponding fits as solid lines. Gray lines depict the fits of the individual features. Arrows indicate the excitation wavelengths and dotted lines the spectral positions of the associated ESAs. Adapted with permission from Ref. [85]. Copyright 2015 American Chemical Society.

The small overshoot around zero delay, which disappears within the first few hundred femtoseconds, is treated as coherent artifact and won't be part of the following discussion (see section 4.3.1). It is striking that the extracted lifetime exceeds that of isotopically diluted water and ice by about one order of magnitude [89, 90]. Pursuant to Fermi's golden rule, the relaxation rate is generally subject to two main conditions, which are the presence of suitable accepting modes and the strength of the coupling to these modes. The antisymmetric stretching mode of the perchlorate anion at 1100 cm^{-1} in combination with the OD stretching at roughly 2400 cm^{-1} could be an

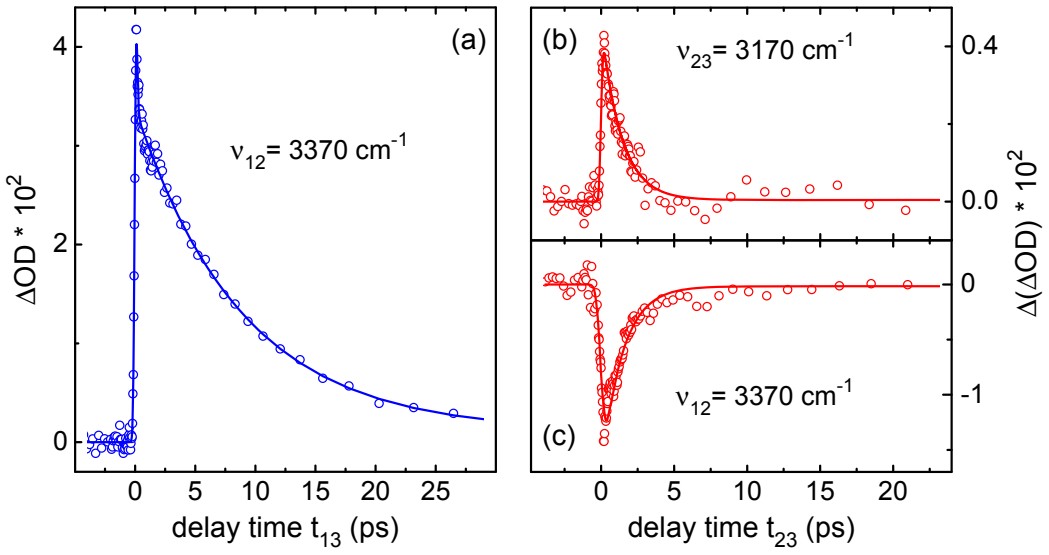

FIGURE 5.3: (a) Pump–probe transient measured in the ESA_{12} at 3370 cm^{-1}. The data shows a population decay time of 9 ps. (b) PREP signal recorded in the ESA_{23} at 3170 cm^{-1} and (c) in the bleaching of the ν_{12} transition at 3370 cm^{-1}. Both transients deliver a time constant of 1.4 ps. Adapted with permission from Ref. [85]. Copyright 2015 American Chemical Society.

accessible relaxation channel [91, 92]. However, the very weak H bonds and the associated very weak coupling of the OH oscillators to their environment strongly hinder relaxation through this channel. There is an ongoing discussion that emphasizes the crucial role of the bending overtone in the relaxation of the OH stretching [93–96]. This overtone is situated at around 2900 cm^{-1} in HDO. Compared to ice, the very weak H bonds in $NaClO_4 \cdot HDO$ and the related blueshift of the OH stretching to 3575 cm^{-1} yield a larger energy mismatch between stretching fundamental and bending overtone, which can explain the larger population lifetime in the hydrate. More sophisticated considerations on the relaxation via the bend mode can be found in chapter 5.3.
In a next measurement the OH stretching overtones shall be observed applying IR pump–repump–probe (PREP) spectroscopy. As before, a pump pulse is used to excite the ν_1 state of the OH stretching in $NaClO_4$ monohydrate. In addition, a delayed repump pulse centered at ν_{12} is utilized to populate the ν_2 state. The repump induced change in the optical density is monitored in the $\Delta(\Delta OD)$ signal that has been described in detail in section 4.3.2. Special attention is paid to the spectral positions of the ν_{12} and ν_{23} transitions. For better differentiation, the first excited state absorption observed in the above PP measurements henceforth is denoted as ESA_{12} and that due to the excitation of the ν_3 level as ESA_{23}. All of the time-resolved measurements within this section were recorded for a fixed pump–repump delay t_{12} of 0.75 ps.

The $\Delta(\Delta OD)$ signal at a pump–probe delay t_{13} of 0.8 ps and accordingly a repump–probe delay t_{23} of 0.05 ps is shown in Fig. 5.2 (d). Two main features are observed: an excited state bleaching (ESB) at the spectral position of the ν_{12} transition and an ESA_{23} due to the ν_{23} transition at (3170 $\pm$ 3) cm^{-1}. Again, excitation by pump, repump, or both pulses simultaneously leads to diverse temperature and pressure jumps in the sample and therefore slightly modifies the hydrate and ice absorption bands. Since the $\Delta(\Delta OD)$ signal puts these different excitation conditions in relation, the latter effects cause additional features in the transient spectra. These are an artifact around the steady state absorption of the ice fraction at 3295 cm^{-1} and some signal at the position of the ν_{01} hydrate absorption band at 3575 cm^{-1}. Furthermore, diminished sample transmission in the maxima of the fundamental ice and hydrate bands reduces the signal-to-noise ratio at these spectral positions. ESB and ESA_{23} are fitted by Lorentzian functions (gray lines), and the corresponding cumulative fit that also accounts for the modified ice absorption band is depicted as solid red line. The fitted amplitude at 3170 cm^{-1} exhibits a FWHM of (105 $\pm$ 30) cm^{-1} and evinces broadening by a factor of roughly 2 when proceeding from ESA_{12} to ESA_{23}. In accordance with observations made by Hamm et al., this may be due to mode mixing between the OH stretching mode and lattice degrees of freedom that becomes more relevant upon climbing higher in the vibrational ladder [52]. The spectra in Figs 5.2 (e) and (f) were recorded at delay times t_{23} of 2 ps and 50 ps to illustrate the decay of the individual signals. As one can see, the $\Delta(\Delta OD)$ signal features no measurable long-time effects 50 ps after (re)excitation.

The transients in Figs 5.3 (b) and (c) show the dynamics measured in the maxima of ESB and ESA_{23} at 3370 cm^{-1} and 3170 cm^{-1}. Fitting an exponential decay to the curve associated with the ESA_{23} delivers a time constant of (1.4 $\pm$ 0.5) ps, which is the population lifetime of the second excited state ν_2. The value indicates a lifetime shortening by a factor of 6.4 when proceeding from the first to the second excited state. This is remarkable since the enhanced overlap of the wave functions for the ν_{12} transition compared to that for the ν_{01} transition would only suggest halving the lifetime.[3] Note that a shortening factor of 2 has been experimentally evidenced in earlier studies on the overtones of the CO stretching in the gas phase [75]. A possible reason for the radical increase of the relaxation rate upon going from ν_1 to

[3] Appropriate computations were conducted applying the matrix elements for the Morse potential that are found in the literature [97, 98]. For ν_{01} = 3575 cm^{-1} and an average anharmonicity of 202.5 cm^{-1}, the calculations yielded a lifetime shortening by factor close to 2.

ν_2 in $NaClO_4$ monohydrate is a more efficient energy transfer to high-lying combination tones. Moreover, the aforementioned mode mixing may result in non-adiabatic coupling between ν_2 and lower vibrational states and thus can accelerate the deexcitation of ν_2 [52].
The ESB measured at 3370 cm^{-1} is shown in Fig. 5.3 (c). It recovers with exactly the same rate as the ESA_{23} decays. This equality of lifetimes is evidence that relaxation from ν_2 to ν_1 proceeds directly with no intermediate states being involved. Moreover, the recovery of the ESB is complete, meaning that the red transient in Fig. 5.3 (c) returns to zero within experimental accuracy. Note that earlier measurements on $NaClO_4 \cdot HDO$ showed that the bleaching of the ν_{01} transition recovers with the same rate as the ESA_{12} decays and that the bleach recovery here also is complete [99]. This behavior explicitly shows that the deexcitation of the ν_2 level proceeds exclusively into ν_1 and then further into the ground state without any additional intermediate steps. In particular, this means that there is no direct relaxation from ν_2 into the ground level. This observation proves that the OH stretching overtone relaxes to a combination of the stretching's fundamental tone and other modes, most likely the bending overtone. Since the ν_{12} transition is redshifted compared to the ν_{01} transition, the energy mismatch to the bending overtone at roughly 2900 cm^{-1} is smaller, which can help to explain the significantly shorter lifetime of the stretching overtone ν_2 with respect to ν_1.

5.1.3 Discussion of the OH Stretch Potential

From the transient spectra in Figs 5.2 (a) and (d), the energy gaps of the vibrational transitions in $NaClO_4 \cdot HDO$ up to the ν_3 level can be quantified. These are ν_{01} = 3575 cm^{-1}, ν_{12} = 3370 cm^{-1}, and ν_{23} = 3170 cm^{-1}. Apparently, the distance between adjacent states is smaller for higher vibrational quantum numbers. A comparison of the transition energies reveals that the frequency shift stays almost constant or rather is even slightly reduced from 205 cm^{-1} (between ν_{01} and ν_{12}) to 200 cm^{-1} (between ν_{12} and ν_{23}). Reflecting the potential's anharmonicity, these values can be employed for further modeling of the OH stretching potential. To this day, a lot of effort was put into finding analytic functions characterizing the vibrational energy surface of the OH stretching vibration [100, 101]. Nonetheless, a comprehensive description is still lacking. In recent studies, particularly the Lippincott-Schroeder (LS) potential was applied for interpreting IR pump–probe and 2D-IR data measured in water and aqueous systems [51, 52, 102, 103]. Describing a linear X–H$\cdots$Y hydrogen bond, the LS potential is the sum of four terms,

which are representing the X–H interaction, the H$\cdots$Y interaction, and the repulsive and attractive interactions between donor and acceptor groups that are functions only of the X$\cdots$Y distance [104, 105]. As evidenced above, the OH oscillators in $NaClO_4$ monohydrate are engaged in very weak H bonds and the potential therefore is dominated by the O–H interaction that is represented by the first term:

$$V_1^{LS}(r_{OH}) = D_e^{LS}\left(1 - exp\left\{\frac{-n(r_{OH} - r_0)^2}{2r_{OH}}\right\}\right) \tag{5.1}$$

Here, D_e^{LS} is the potential depth, r_{OH} the O–H separation, r_0 the respective equilibrium separation with a typical value of 0.97 $\mathring{A}$, and n a potential factor that typically ranges between 9.15 $\mathring{A}^{-1}$ and 10.2 $\mathring{A}^{-1}$ (9.55 $\mathring{A}^{-1}$ on average) [52, 103, 106]. Substituting these values into Eq. 5.1 and solving the Schrödinger equation leads to transition frequencies of ν_{01} = 3574 cm^{-1}, ν_{12} = 3369 cm^{-1}, and ν_{23} = 3158 cm^{-1} for a reduced mass of $\mu = 1.225 \cdot 10^{-27}$ kg and a potential depth of D_e^{LS} = 29800 cm^{-1}. One can immediately see that these numbers are in good agreement with the experimental data.
However, the anharmonicity provided by the LS potential is increasing from 205 cm^{-1} (between ν_{01} and ν_{12}) to 211 cm^{-1} (between ν_{12} and ν_{23}) which is in contrast to the experimentally measured anharmonicity that appears to be almost constant or even to be slightly shrinking. Considering the anharmonicity to be constant with an average value of 202.5 cm^{-1} hence rather suggests modeling by a Morse potential, which features a constant anharmoniticy and is of the form

$$V^M(r_{OH}) = D_e^M(1 - exp\{-a(r_{OH} - r_0)\})^2, \tag{5.2}$$

where a is a potential factor. The Schrödinger equation can be solved analytically for a Morse potential, yielding a potential depth D_e^M of 35250 cm^{-1}, which is close to the binding energy of water (38750 cm^{-1}) [102]. In combination with the reduced mass calculated with help of the LS potential, one derives a potential factor a of 2.8 $\mathring{A}^{-1}$.[4]
Note that these rather simple estimations should not be consulted to find the optimal OH stretching potential but are able to show how the newly generated data can contribute to improve theoretical potentials and help to model the associated H bond interactions.

[4] I want to thank K. Stallhofer for carrying out the calculations.

Concluding this section, the world's first purely MIR pump–repump–probe measurements were performed on the excited states of the OH stretching vibration of quasi-isolated water molecules in $NaClO_4$ monohydrate. The generated data shows population lifetimes of (9 ± 2) ps and (1.4 ± 0.5) ps for the first and second excited state. The spectral positions of the vibrational overtones up to the ν_3 level were extracted and analyzed by means of Lippincott-Schroeder and Morse potentials. Moreover, it is shown that the deexcitation of ν_2 proceeds in a stepwise manner via the ν_1 state. With regard to the applied setup, the presented results show that PREP is not only capable of determining the spectral positions and lifetimes of the OH stretching overtones but can also unravel the relaxation pathways. The data provides explicit and new information on the OH stretching overtones that can be used for a theoretical modeling of the OH stretching potential, and a more comprehensive description of the impact of underlying H bond interactions.

5.2 Dynamics of the OH Stretching Mode in Cyclic Planar Water Trimers in $Ba(ClO_4)_2$ Trihydrate

While the last section focused on well isolated water molecules, the present chapter is concerned with small water clusters. The inclusion of the interactions between individual water molecules is the next building stone in reconstructing the dynamic processes in water. Moreover, proceeding from HDO:D_2O to pure H_2O as a solvent facilitates the investigation of symmetric and antisymmetric OH stretch vibrations and their mutual relaxation dynamics.

Since the overall character of the interactions in small water clusters equals that in the bulk, they can be used to probe water's intermolecular energy surface [37, 107–109]. However, the relative importance of the various types of interaction can vary distinctly. Comprehensive analysis of the water trimer showed that here the contribution that different kinds of interactions make up to the total energy crucially depends on the mutual angular orientation of the water molecules [110, 111]. This makes the trimer an excellent model system to investigate the diverse types of intermolecular forces. While previous studies on these systems focused on the gas phase [112–114], here first IR-pump–probe measurements on water trimers in the solid phase are presented. In contrast to recent measurements on hydrates that mainly focused on the impact of hydrogen bonding onto the properties of aqueous systems [22, 115–117], with barium perchlorate ($Ba(ClO_4)_2$) trihydrate, a sample is chosen that features virtually no hydrogen bond interaction between the individual water molecules. It offers well separated two-dimensional water layers that contain cyclic planar water trimers. Absence of H bonds between the water molecules of one three-ring implies that the electrostatic forces, namely those between the water oxygens and the Ba^{2+} ions, are stronger than the short-range interactions that lead to the formation of hydrogen bonds.

5.2.1 Crystal Structure and Absorption Spectrum

The crystal structure of $Ba(ClO_4)_2 \cdot 3H_2O$ was analyzed by X-ray diffraction [118, 119]. There has been a lack of clarity whether the trihydrate crystallizes in the hexagonal pyramidal space group $P6_3$ or in the dipyramidal space group $P6_3/m$. In 1988, Gallucci et al. claimed to have resolved the ambiguity and established the centrosymmetric space group $P6_3/m$ as the correct one [120]. However, in the investigations presented below, both groups are considered since the measured data points towards the presence

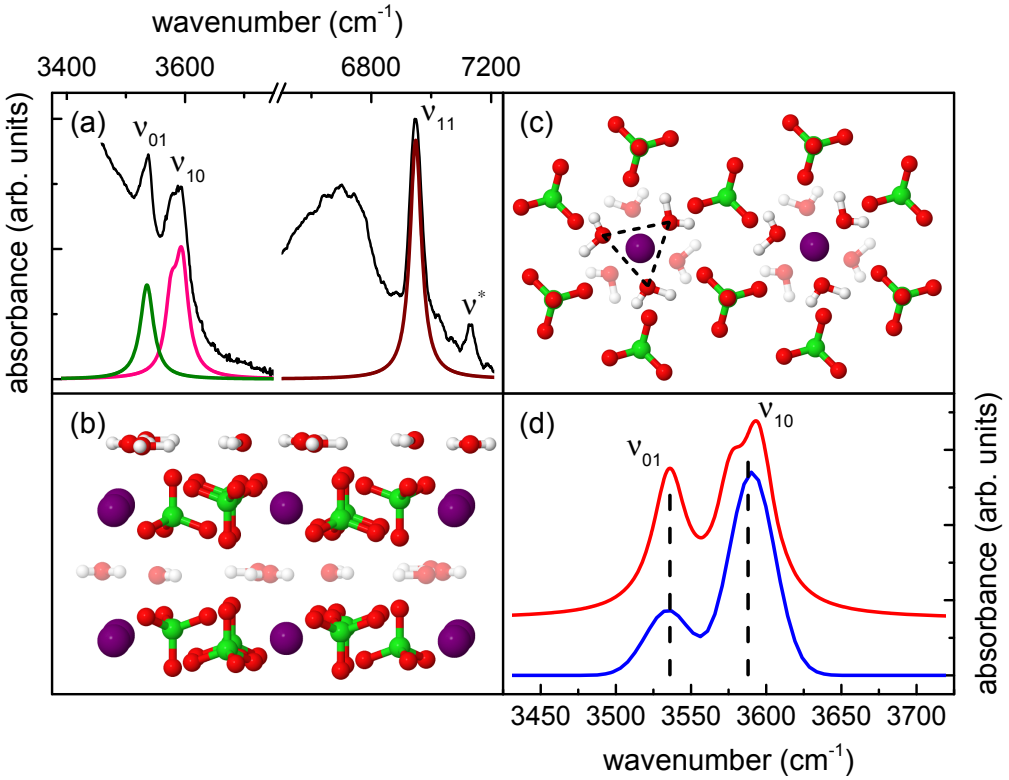

FIGURE 5.4: (a) FTIR absorption spectra of the OH stretching fundamental and overtone region in $Ba(ClO_4)_2$ trihydrate at 200 K (black line). Hydrate absorption bands of symmetric stretching (ν_{01}, green), antisymmetric stretching (ν_{10}, pink), and stretching overtone (ν_{11}, brown) are analyzed by Lorentzian functions. Fundamental and overtone spectra were recorded applying samples of varying thickness and have independently been normalized, thus their absolute amplitudes cannot be put in relation. (b) Crystal structure of $Ba(ClO_4)_2$ trihydrate (Ba in purple, Cl in green, H in white, and O in red). Planes consisting of water molecules alternate with planes comprised of barium and perchlorate ions. (c) Top view of the crystal structure shown in (b). Water trimers placed on top of one another are twisted by an angle of 60° (opaque and transparent red) and arrange circularly around a Ba^{2+} ion in the center. (d) Background corrected stretching bands ν_{01} and ν_{10} (red), and corresponding absorption spectrum deduced from quantum chemical calculations (blue). The data is vertically stacked for better visualization.

of non-centrosymmetric features, which are due to either static disorder or dynamic coupling to symmetry-breaking low-frequency modes. As it can be seen in Fig. 5.4 (b), planes consisting of water molecules are alternating with planes containing Ba^{2+} and ClO_4^- ions. Each perchlorate anion is bound to nine water molecules via weak H bonds. Two successive water layers are separated by a distance of 483 pm. The top view in Fig. 5.4 (c) shows that in a water plane always three water molecules arrange circularly around a

barium ion (purple) with an O–O distance of 284 pm, which is very similar to the corresponding O–O distance in bulk water ($\approx$ 285 pm) and ice (275 pm). The consecutive trimer one water level below exhibits an angular displacement of 60°.

FTIR spectra of $Ba(ClO_4)_2 \cdot 3H_2O$ at 200 K are displayed in Figs. 5.4 (a). The low solubility of barium perchlorate gives rise to a pronounced ice phase around 3250 cm^{-1}, which overlaps with two hydrate features at 3536 cm^{-1} and 3588 cm^{-1}. Note that the measurements on $Ba(ClO_4)_2 \cdot (HDO+2D_2O)$ shown in the next chapter reveal a hydrate absorption band at 3564 cm^{-1}, which is well centered between the two features in the H_2O species (see Fig. 5.11 (a)). A symmetric distribution around the HDO feature indicates that the two features in Fig. 5.4 (a) can be assigned to the symmetric and antisymmetric stretching modes of the H_2O molecules (see section 2.2). In the following, the vibrational states are denoted as ν_{as} with a the quantum number of the antisymmetric stretch and s that of the symmetric stretching vibration. It is emphasized that this designation is only related to the symmetry of the vibrations of individual water molecules and does not pertain to the symmetry assumptions that are concerned with the hydrate crystal. The antisymmetric band is composed of two subbands at roughly 3576 cm^{-1} and 3595 cm^{-1} with FWHMs of 23 cm^{-1} and 26 cm^{-1}, while the symmetric absorption band at 3536 cm^{-1} can be well approached by one single Lorentzian peak with a FWHM of 27 cm^{-1}. Note that measurements at lower temperatures showed the onset of a splitting in the symmetric band as well. The large amount of blueshift of the hydrate features with respect to the center of the ice absorption band gives evidence of relatively weak hydrogen bonds between water molecules and perchlorate anions [121].

In the red spectrum in Fig. 5.4 (d), the symmetric and antisymmetric hydrate peaks, ν_{01} and ν_{10}, are displayed without ice background. The latter was removed by fitting appropriate Gaussian functions and subsequently subtracting the fit from the data. The blue curve is yielded by quantum chemical simulations, which were executed at the *Wilhelm-Ostwald-Institut für Physikalische und Theoretische Chemie* at the *Universität Leipzig*.[5] The computations apply a semiclassical combination of normal modes and provide spectra that are in good agreement with the measured data. A detailed description of the procedure can be found in App. A.1. In accordance with the above assignment of the hydrate features to ν_{01} and ν_{10}, the simulated vibrations associated with the left peak only show symmetric vibrations, while those

[5] I want to thank Dr. Petko Petkov for conducting the calculations.

giving rise to the right band solely exhibit antisymmetric oscillations. The calculations impose $P6_3/m$ symmetry on the crystal resulting in completely delocalized modes. This hinders splitting of the obtained stretching modes as it is observed in the measured ν_{10} absorption band. The relation between mode splitting and crystal symmetry will be further discussed below. With regard to a hexamer consisting of two vertically next water trimers (opaque and transparent red-white molecules in Fig. 5.4 (c)), the simulations reveal that two water molecules that are situated on opposite sides of a Ba^{2+} ion vibrate either in phase or in counter-phase. The respective phase relation thereby is the same for all three pairs of opposing water molecules, which indicates coupling between next trimers.[6]

Turning to the overtone region in Fig. 5.4 (a), one sees a broadband feature around 6700 cm^{-1}, which most likely is due to the OH stretching overtone of the ice fraction, and two narrowband features, ν_{11} and ν^*, at 6949 cm^{-1} and 7130 cm^{-1} stemming from the hydrate water molecules. The latter features a frequency that matches well with the sum of ν_{01} and ν_{10} and thus could be associated with simultaneous excitation of these two bands. It is a minor peak and will not be subject of further discussion. The time-resolved measurements below allow the assignment of the prominent peak at 6949 cm^{-1} to a combination tone of symmetric and antisymmetric stretching, ν_{11}. With only one dominant hydrate absorption band, the overtone spectrum is in stark contrast to corresponding spectra, measured for isolated D_2O molecules [122] and quasi-isolated water molecules in $NaClO_4 \cdot H_2O$ (see Fig. 5.5 (b)). The latter show two additional features assignable to the pure overtones of symmetric and antisymmetric stretching, ν_{02} and ν_{20}.

5.2.2 Discussion of the Crystal Symmetry

The following group theoretical discussion shall put the above observations in relation to the crystal symmetry.[7] Consistent with the centrosymmetric space group $P6_3/m$, a simplified unit cell with two water trimers and a Ba^{2+} ion in the inversion center is considered applying $S6$ symmetry (see Fig. 5.4 (c)). Two nearest Ba^{2+} ions of two successive salt layers lie on the z axis. The strong transition dipole coupling via the twice positively charged Ba^{2+} ions can lead to delocalization of the OH stretching mode on trimers that are symmetry related by inversion on the barium cations. Transitions

[6] Note that within the limits of the simulations, only two distinct phases that differ by π are permitted. However, the consistency of the phase relation on the whole hexamer strongly points towards coupling between the two trimers.

[7] I want to thank Prof. Dr. Sighart Fischer for his friendly assistance.

in the xy plane of the trimers are in principle degenerate in the $S6$ point group. However, small modulations via low-frequency modes can be treated semiclassically for pulses shorter than the vibrational period of the respective mode and hence can violate the symmetry.[8] If the gain in energy by localization exceeds the delocalization energy, dynamic symmetry breakage may evolve as a localization process after excitation. Due to the asymmetric environment of the two OH groups of one water molecule and the related different hydrogen bonding strengths, a breaking of the symmetry can lift the degeneracy of the stretching modes and evoke mode splitting. The effect will be more pronounced in the case of ν_{10} since it features the larger amplitude of the OH stretch and hence is more sensitive to its environment. This can explain the relatively pronounced subdivision of the antisymmetric mode in the FTIR measurements. Note that if the environment violates the symmetry already in the ground state, the splitting of the degenerate modes would be static and the $P6_3/m$ symmetry group with inversion should be relaxed towards the $P6_3$ space group. The same considerations are valid with regard to the applied $S6$ symmetry. It is emphasized that the structure analysis that was done by X-ray diffraction is generally not very sensitive to the hydrogen positions. In contrast, the IR spectroscopic methods which were utilized to generate the present data are very well suited to detect minor symmetry breaking related to the actual coordinates of H atoms engaged in hydrogen bonds.

FTIR spectra of $Ba(ClO_4)_2 \cdot 3H_2O$ and $NaClO_4 \cdot H_2O$ at 200 K are contrasted in Figs 5.5 (a) and (b). Apart from two features stemming from the symmetric and antisymmetric OH stretching, ν_{01} and ν_{10}, both fundamental regions display pronounced ice absorptions around 3250 cm^{-1}. Obviously, these ice bands differ distinctly in their shape. Particularly, the ice absorption in $NaClO_4 \cdot H_2O$ looks very familiar (see for example Fig. 5.13 (a) for comparison), while the respective band in the $Ba(ClO_4)_2 \cdot 3H_2O$ sample is of unconventionally flat shape. This may be effected by either surface effects at the hydrate–ice interfaces or by saturation of the detector. Since the ice phase is not of interest, this discussion is not deepened. Featuring four hydrate peaks, the overtone region of $NaClO_4 \cdot H_2O$ is in stark contrast to that of the $Ba(ClO_4)_2$ sample. The one with the highest energy at 7155 cm^{-1}, ν^*, most likely is due to simultaneous excitation of the ν_{01} and ν_{10} bands. The peaks

[8] An exemplary mode with a frequency of the order of a few tens of wavenumbers was yielded by the above quantum simulations. In the process of this vibration, two vertically next trimers are tilted against each other and thus inversion symmetry in relation to the Ba^{2+} ions is violated.

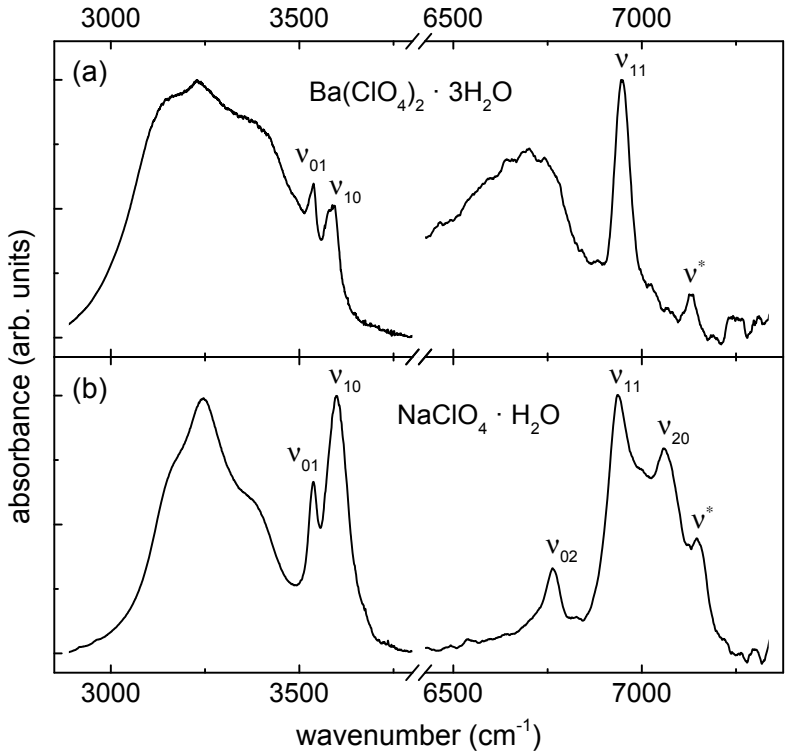

FIGURE 5.5: Comparison between the fundamental and overtone regions of the OH stretching in $Ba(ClO_4)_2 \cdot 3H_2O$ and $NaClO_4 \cdot H_2O$ at 200 K. (a) In $Ba(ClO_4)_2$ trihydrate, ν_{01}, ν_{10}, ν_{11}, and ν^* are located at 3536 cm^{-1}, 3588 cm^{-1}, 6949 cm^{-1}, and 7130 cm^{-1}. (b) In $NaClO_4$ monohydrate, ν_{01}, ν_{10}, ν_{02}, ν_{11}, ν_{20}, and ν^* are situated at 3535 cm^{-1}, 3600 cm^{-1}, 6760 cm^{-1}, 6938 cm^{-1}, 7065 cm^{-1}, and 7155 cm^{-1}. The spectra of fundamental and overtone region were measured applying samples of different thicknesses and have been normalized independently, thus their absolute amplitudes cannot be compared.

at 6760cm^{-1}, 6938 cm^{-1}, and 7065 cm^{-1} are identified to be ν_{02}, ν_{11}, and ν_{20}. This is in a accordance with Ref. [122], where the combination tone was found to range between the overtones of the symmetric and antisymmetric stretching vibration. Considering the water molecules in sodium perchlorate monohydrate to be quasi-isolated, as it was evidenced in the last chapter, one can impose the C_{2v} point group that describes a single water molecule. In C_{2v}, all overtones, ν_{02}, ν_{11}, and ν_{20}, are IR active. On the other hand, when the centrosymmetric group with the inversion subgroup S_6 is considered for delocalized modes in $Ba(ClO_4)_2 \cdot 3H_2O$, all overtones are in principle forbidden. Although the inversion symmetry may be weakly broken, the long range transition dipole interaction prevails and can suppress the diagonal overtones ν_{02} and ν_{20}. However, this argument does not strictly apply to the combination tone ν_{11} when localization is considered. The fact that the ν_{11} bands in the two hydrates lie energetically very close strongly points

towards localization in the $Ba(ClO_4)_2$ sample since the water molecules in the $NaClO_4$ species are well isolated. This assumption is further corroborated when calculating the energy of the overtone of $Ba(ClO_4)_2$ in 5 M HDO:D_2O from its fundamental stretching and ESA (see Figs 5.11 (a) and (d) in chapter 5.3.2). Summation delivers a total overtone frequency of 6949 cm^{-1}, which exactly matches that in the H_2O sample. The small solvent molarity ensures that there is only one HDO molecule in the investigated trimers at a time. The similarity to the overtone energy in the HDO sample therefore is a further indication of localization on one water molecule in the H_2O hydrate.

5.2.3 Individual Excitation of Symmetric and Antisymmetric Stretching Vibration

In three pump–probe experiments, different spectral selection of the excitation pulses was applied to individually pump symmetric ($\nu_{00} \rightarrow \nu_{01}$) and antisymmetric stretching ($\nu_{00} \rightarrow \nu_{10}$) and to excite both simultaneously ($2\nu_{00} \rightarrow \nu_{01} + \nu_{10}$). The measurements were carried out at a sample temperature of 200 K in the redshifted ESA. In the following time-resolved experiments, the subdivided antisymmetric mode is considered as one absorption band at 3588 cm^{-1} with an average spectral width of 42 cm^{-1}, which is reasonable since the bandwidth of the pump pulses exceeds the energy separation of the two subbands.
Fig. 5.6 (a) shows transient spectra recorded at different pump–probe delays after solely pumping the antisymmetric stretching at 3588 cm^{-1}. Excitation gives rise to two distinct features at (3355 ± 5) cm^{-1} and (3403 ± 5) cm^{-1}. At a delay of 0.5 ps, the former peak exhibits the larger amplitude, while at 2.5 ps the high-energy absorption has fully developed and is more pronounced. The signals recorded at larger delay times show no considerable change in their spectral shape and display a joint population decay. The FWHM of the two bands is (40 ± 5) cm^{-1} at an energy separation of (52 ± 5) cm^{-1}, which is very similar to that of the fundamental hydrate peaks in the FTIR spectra in Fig. 5.4 (a). The associated spectra recorded after individual excitation of the symmetric stretch are given in Fig. 5.6 (b). For time delays exceeding 2.5 ps, the measured curves show similar shape and dynamics as in Fig. 5.6 (a). However, the initial dynamics are very different. At 0.5 ps the feature at (3403 ± 5) cm^{-1} is very dominant. Subsequently, its high-energy wing slightly shifts towards smaller energies and the second band at 3355 cm^{-1} becomes more pronounced. Based on these observations, the energy schemes in Figs 5.6 (c) and (d) are deduced: Pumping the antisymmetric stretching

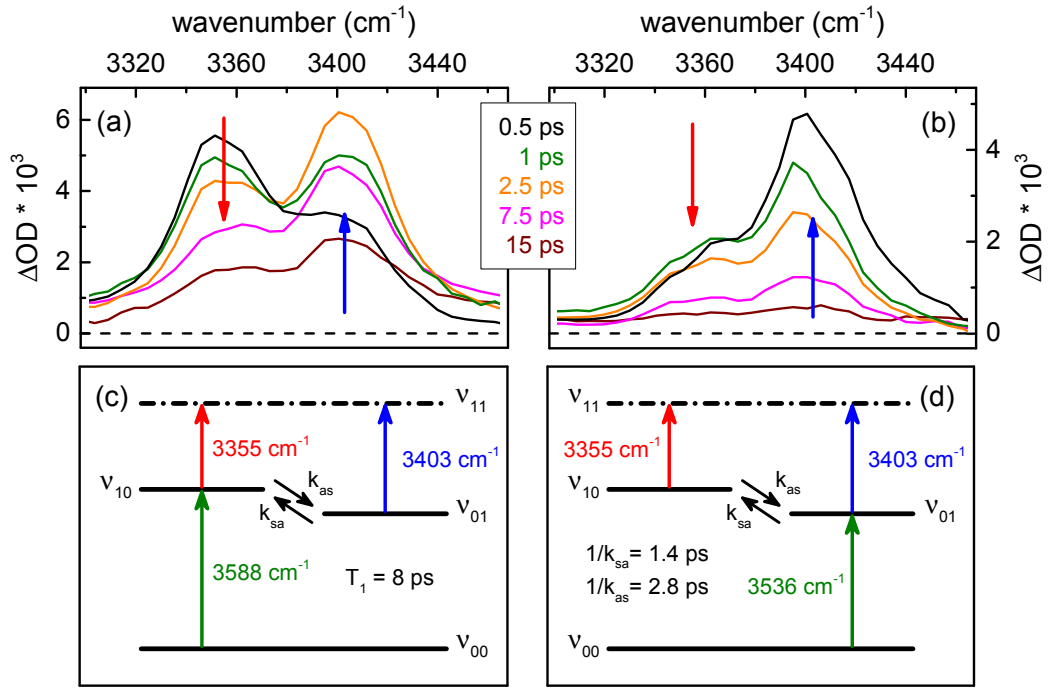

FIGURE 5.6: (a) Transient spectra recorded after excitation of the antisymmetric stretching ν_{10} at 3588 cm^{-1}. Red and blue arrows indicate the maxima of the ESAs at 3355 cm^{-1} and 3403 cm^{-1}. (b) Corresponding spectra recorded after pumping the symmetric stretching ν_{01} at 3536 cm^{-1}. (c,d) Energy schemes for both excitation conditions. Pump excitation is illustrated by green arrows. Red and blue arrows represent the probed ESAs, and black arrows indicate relaxation between ν_{01} and ν_{10} with the associated rates k_{sa} and k_{as}. T_1 is the effective excited state population lifetime.

yields direct excitation of the left branch in Fig. 5.6 (c), while the absorption at 3403 cm^{-1} evolves delayed. This behavior is inverted after excitation of the symmetric stretching (see Fig. 5.6 (d)). Here, the right branch is excited directly and the feature at 3355 cm^{-1} occurs with temporal delay. Following the excited pathways in the two figures leads to a total energy of roughly 6940 cm^{-1} for both excitation conditions. This value matches well with the energy of the overtone in Fig. 5.4 (a) and indicates that the latter actually is a combination tone. Note that the initially recorded redshift in Fig. 5.6 (b) could be linked to localization, as discussed in the above symmetry assumptions.

In Fig. 5.7 (a), transients recorded close to the maxima of the two ESAs after excitation of ν_{10} are depicted.[9] The rising slope of the red trace at 3355 cm^{-1} is dominated by the time resolution, while the feature at 3405 cm^{-1} exhibits a slower rise time. As already visualized in the energy schemes, the dynamics

[9]Since two adjacent detection channels translate into frequencies with a separation of about 5 cm^{-1} (see section 4.1.1), the channels closest to the fitted maxima of the two ESAs were chosen to extract the transients.

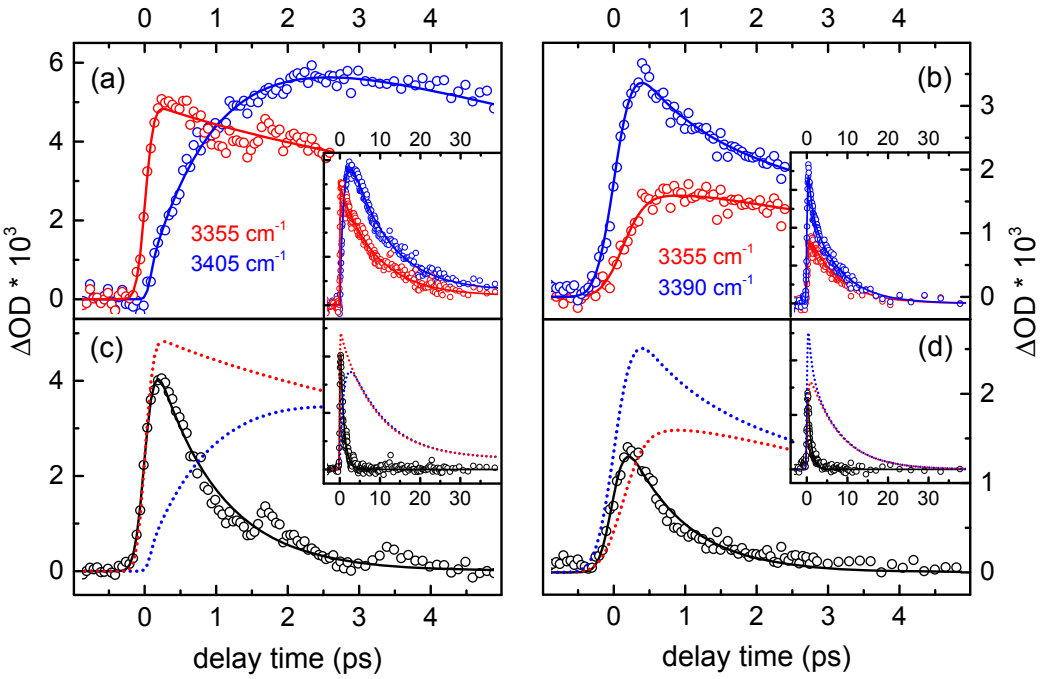

FIGURE 5.7: (a) Transients (and fits) measured in the maxima of the two ESAs at 3355 cm^{-1} (red) and 3405 cm^{-1} (blue) recorded after pumping the ν_{10} band. (b) Respective transients measured at 3355 cm^{-1} and 3390 cm^{-1} after excitation of the symmetric stretching ν_{01}. (c) The transient at 3405 cm^{-1} (blue-dashed) was scaled to match that measured at 3355 cm^{-1} (red-dashed) for large delays. Subtraction yields a difference curve that decays with a total rate of $(k_{as} + k_{sa} + k)$ (black). (d) Here, the curve at 3390 cm^{-1} (blue-dashed) was scaled to lie on top of the one recorded at 3355 cm^{-1} (red-dashed). The black data shows the appropriate difference curve.

indicate direct excitation of the $\nu_{10} \rightarrow \nu_{11}$ transition, whereas the $\nu_{01} \rightarrow \nu_{11}$ transition can only be observed after population redistribution between ν_{01} and ν_{10}. The corresponding transients recorded after excitation of ν_{01} are shown in Fig. 5.7 (b). Note that here the blue curve is recorded at 3390 cm^{-1}, left of the absorption's maximum at 3403 cm^{-1}. This was done to prevent the aforementioned initial redshift of the high-energy flank of the right feature in Fig. 5.6 (b) from affecting the dynamics. The blue transient peaks 0.3 ps after excitation and subsequently shows a fast population decay on a picosecond timescale. Conversely, the signal at 3355 cm^{-1} rises more slowly. For delay times exceeding 3 ps, all four curves in Figs 5.7 (a) and (b) exhibit approximately the same kinetics, yielding an effective population lifetime T_1 of (8 ± 1) ps.

In the following, a kinetic model to extract the relaxation dynamics between ν_{01} and ν_{10} shall be established. In Figs 5.7 (a) and (b), the red pump–probe traces reflect the population dynamics of ν_{10} and henceforth are denoted as $PP_a(t)$. The population of ν_{01} is represented by the blue transients and is

abbreviated by $PP_s(t)$. The signals can be transposed into actual populations by linear interpolation. Then the occupations of ν_{01} and ν_{10} are of the form $N_s(t) = c_s PP_s(t)$ and $N_a(t) = c_a PP_a(t)$ with the undetermined proportionality factors c_s and c_a. In the analysis below, the exchange rates for relaxation from ν_{01} to ν_{10} and vice versa are denoted k_{sa} and k_{as}. Moreover, ν_{01} and ν_{10} are assumed to show the same population lifetime T_1 of 8 ps. This assumption cannot actually be validated. However, model calculations for the extreme case that only one of the two vibrations is allowed to relax into the ground level show that this would change the ratio of exchange rates k_{sa}/k_{as} by only about 10 %. This deviation is accounted for in the corresponding error margins given below. The following rate equations can be set up:

$$\begin{aligned}\dot{N}_s(t) &= +k_{as}N_a(t) - k_{sa}N_s(t) - kN_s(t) = -(k_{as} + k_{sa} + k)N_s(t) + k_{as}N(t)\\ \dot{N}_a(t) &= -k_{as}N_a(t) + k_{sa}N_s(t) - kN_a(t) = -(k_{as} + k_{sa} + k)N_a(t) + k_{sa}N(t)\end{aligned} \quad (5.3)$$

Here, $k = 1/T_1$ is the rate associated with the overall population decay, and $N(t) = N_s(t) + N_a(t)$ is the total excited state population. The latter obviously obeys $\dot{N}(t) = -kN(t)$. Under the assumption that all relaxation rates can be treated as constant, the above differential equations can be solved by

$$\begin{aligned}N_s(t) &= N_{s0}e^{-(k_{as}+k_{sa}+k)t} + \frac{k_{as}}{k_{as}+k_{sa}}N(t)\\ N_a(t) &= N_{a0}e^{-(k_{as}+k_{sa}+k)t} + \frac{k_{sa}}{k_{as}+k_{sa}}N(t),\end{aligned} \quad (5.4)$$

with the constants N_{s0} and N_{a0}. The slow dynamics of the total population proceeding with k can be eliminated by calculating $N_a(t) - k_{sa}/k_{as} \cdot N_s(t)$, which is equal to

$$PP_a(t) - \frac{k_{sa}}{k_{as}}\frac{c_s}{c_a}PP_s(t) = PP_a(t) - d \cdot PP_s(t). \quad (5.5)$$

In this expression, a scaling factor d, which stands for $k_{sa}c_s/k_{as}c_a$, is introduced. In practice, d is found by scaling the blue transients in Figs 5.7 (a) and (b) to match the red ones at large delays (see inset in Figs 5.7 (c) and (d)). This is reasonable since both curves show the same long-time dynamics. After scaling, the signals are subtracted according to Eq. 5.5. The signal thus generated is shown in black in Figs 5.7 (c) and (d). For better comparison, the difference signal in Fig. 5.7 (d) was multiplied by a factor of -1. Note that d is frequency dependent and thus not the same for the transients in Figs 5.7 (a) and (b) since the blue curve once was recorded at 3405 cm^{-1} and once at 3390 cm^{-1}. The modulations at 1.7 ps and 3.4 ps in the transient data

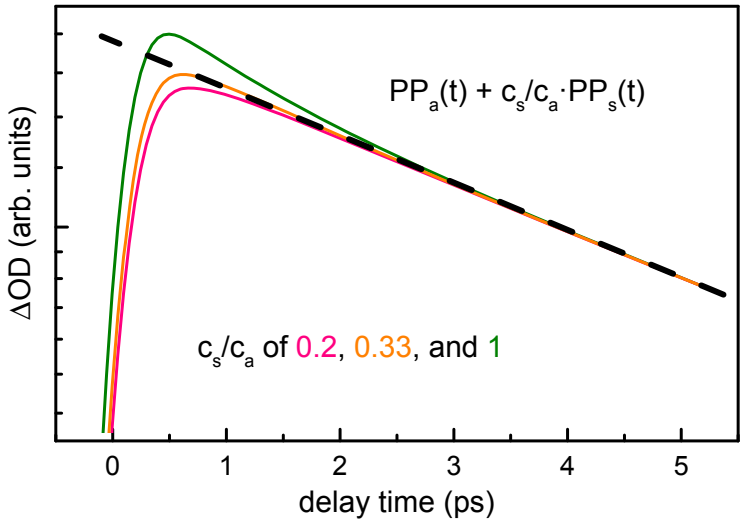

FIGURE 5.8: Procedure that is applied to extract the scaling factor c_s/c_a from the experimental data. Here, exemplary the fitted data from Fig. 5.7 (b) is used. $PP_a(t) + c_s/c_a \cdot PP_s(t)$ is calculated for different values of the scaling factor c_s/c_a and plotted in a logarithmic representation. The curves are scaled to match at long delay times. The correct factor is found by minimizing the difference between the sum curve and a straight line (black-dashed) that reflects the population decay proceeding with T_1.

in Fig. 5.7 (c) may be due to a beating between the two subbands of the antisymmetric stretching that were observed in the FTIR spectra.[10] According to Eqs 5.4 and 5.5, the slope of the difference curves can be approximated by a monoexponential decay with a total rate of $(k_{as} + k_{sa} + k)$. The corresponding time constants are in good accordance for both excitation conditions and can be quantified to be (0.85 ± 0.15) ps.

Next, the individual relaxation rates k_{sa} and k_{as} shall be extracted. To do so, c_s/c_a has to be determined in order to extract the ratio of rates from the scaling factor d. The contribution of the population redistribution between ν_{01} and ν_{10} can be canceled out by calculating

$$\frac{N(t)}{c_a} = \frac{N_s(t) + N_a(t)}{c_a} = PP_a(t) + \frac{c_s}{c_a} PP_s(t). \tag{5.6}$$

In practice, this is done by computing the sum curve of the blue and red transients in Figs 5.7 (a) and (b) as a function of the scaling factor c_s/c_a. In a logarithmic representation, the correct ratio then can be found by minimizing the deviation of the sum curve from a straight line whose gradient reflects the

[10] A beat frequency of 1.7 ps corresponds to an energy distance of 19.6 cm^{-1}, which matches very well with the separation of the two subbands observed in the antisymmetric stretching band at 3576 cm^{-1} and 3595 cm^{-1}.

overall population decay rate k. Fig. 5.8 shows corresponding sum curves obtained for the pump–probe signals in Fig. 5.7 (b) and different values of the scaling factor c_s/c_a. For better comparison, the transients were scaled to lie on top of each other at large delay times. Here, the orange curve visibly fits best. With c_s/c_a = 0.33 and a scaling factor d = 0.75, this leads to a ratio of relaxation rates k_{sa}/k_{as} = 2.3 in this case. However, a set of statistics including several measurements showed that k_{sa}/k_{as} can best be approached by 2 ± 0.7. Again, the values deduced for the different excitation conditions are in good agreement. Along with a rate k of (8 ps)$^{-1}$ for the joint population decay and a total rate $(k_{as} + k_{sa} + k)$ of (0.85 ps)$^{-1}$, one can immediately calculate the individual rates and obtains k_{sa} = (1.4 ps)$^{-1}$ and k_{as} = (2.8 ps)$^{-1}$.
In comparable measurements on isolated D_2O molecules, the ratio of relaxation rates was identified to depend exclusively on the phonon occupation number n_p, which yields $k_{sa}/k_{as} = n_p/(1+n_p)$ [122, 123]. With a given energy distance of 52 cm^{-1} between ν_{01} and ν_{10} at a sample temperature of 200 K, this expression delivers a value of 0.7. The big difference to the experimental value of 2 indicates that more than two states may be involved. In particular, the splitting-up of the antisymmetric band ν_{10} is considered. Fast relaxation from one antisymmetric subband to the other after population redistribution between symmetric and antisymmetric stretching can distinctly affect the equilibrium condition and thus modify the relaxation rates. Note that relaxation within the subdivided antisymmetric band can also be related to the aforementioned localization after breaking of the symmetry.

5.2.4 Simultaneous Excitation of Symmetric and Antisymmetric Stretching Vibration

In a last experiment, symmetric and antisymmetric stretching modes were pumped simultaneously. The corresponding transient spectra are depicted in Fig. 5.9 (a). At 0.15 ps, two features are visible. The high-energy band is centered around 3415 cm^{-1} and subsequently shifts towards lower energies. At delay times larger than 0.5 ps, the spectra exhibit similar shape and dynamics as in Figs 5.6 (a) and (b). The corresponding energy scheme is drawn in Fig. 5.9 (b). In Fig. 5.9 (c) transients measured at 3355 cm^{-1} and 3390 cm^{-1} are given. As after excitation of the symmetric stretching, the blue transient is measured at 3390 cm^{-1} to minimize the impact of the initial redshift. For better visualization, the blue transient already is scaled by c_s/c_a (see below). One immediately sees a sinusoidal modulation on top of the blue and red transients. This is interpreted as a Λ-type quantum beating between ν_{01} and

ν_{10} that can be observed via the combination tone ν_{11}. Note that this is a further indication that ν_{11} in fact is a combination tone of symmetric and antisymmetric stretching. For a more detailed analysis of this phenomenon, the sum signal pursuant to Eq. 5.6 shall be calculated again. First, the factor d is extracted by scaling the transients recorded at 3355 cm^{-1} and 3390 cm^{-1} to coincide for long delays. In order to extract c_s/c_a, the obtained factor d is divided by the ratio of exchange rates that previously was determined to be roughly 2. Now the respective sum curve can be generated according to Eq. 5.6 (black data points in Fig. 5.9 (c)). It is composed of a monoexponential decay overlaid by the beat signal.[11] Fitting an exponential slope (black solid line) yields the same lifetime of (8 $\pm$ 1) ps as in the case of individual excitation.

Fig. 5.9 (d) displays the signal that is remaining after subtracting the monoexponential fit (black line) from the data points in Fig. 5.9 (c). It can be well approached by a sine function multiplied by an exponential decay. However, data analysis showed that the modulations exhibit a shift towards smaller frequencies proceeding in the first few hundred femtoseconds after excitation. This was implemented in the fitting procedure. The resulting curve is shown as solid black line in Fig. 5.9 (d). It is the product of an exponential decay and a sine with an initial frequency of 73 cm^{-1} that is reduced to 52 cm^{-1} within 0.5 ps and subsequently stays constant. Note that small deviations of fit and difference data may be due to the splitting-up of the ν_{10} mode, which can cause an additional modulation similar to that observed in Fig. 5.7 (c). The final beat frequency is in good accordance with the energy distance between ν_{01} and ν_{10}. Moreover, the initial chirp in the beat frequency well reproduces the incipient spectral shift in Fig. 5.9 (a). The latter may be of the same nature as the initial spectral dynamics in Fig. 5.6 (b) and could again be related to the localization dynamics. Concerning the above discussion on the origin of the symmetry breakage, this observation obviously points towards dynamic symmetry breaking rather than innate asymmetries. Contrary to Fig. 5.6 (b), the redshift of the high-energy wing in Fig. 5.9 (a) is complete at a delay of 0.5 ps. Since spectrally broader pump pulses were applied in the present experiment, this can be attributed to the better time resolution. In turn, this shows that the duration of the spectral shift in Fig. 5.6 (b) may be overestimated.

[11] Note that the fact that the modulation's amplitude is amplified in the sum curve indicates that the oscillations in the blue and red curves exhibit similar (if not the same) phase. This observation clearly points out that the modulations actually constitute a quantum beat signal.

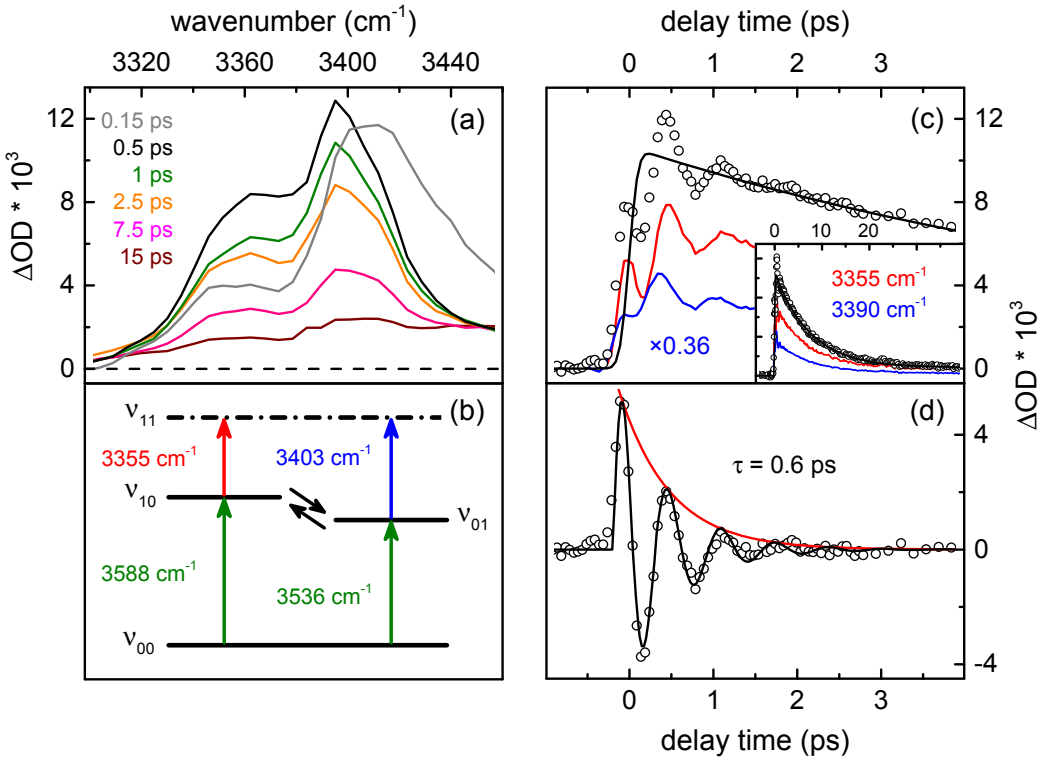

FIGURE 5.9: (a) Transient spectra recorded at different delay times after simultaneous excitation of the ν_{01} and ν_{10} bands. (b) Corresponding energy scheme with pump excitation indicated by green arrows and ESAs by red and blue arrows. The relaxation between ν_{01} and ν_{10} is indicated by black arrows. (c) Transients measured at 3355 cm^{-1} (red) and 3390 cm^{-1} (blue). The blue curve is scaled by a factor of c_s/c_a = 0.36. Black circles indicate the sum signal of blue and red traces . The solid black line represents an exponential decay proceeding with T_1. (d) Quantum beats extracted by subtracting fit from sum data in (c). The solid black line represents a fit that is comprised of a chirped sine wave multiplied by a monoexponential decay (red).

The decay of the beat signal is a measure of the loss of mutual coherence between the two states ν_{01} and ν_{10}. From the exponential slope in Fig. 5.9 (d), a coherence decay time τ of (0.60 $\pm$ 0.07) ps is extracted. This value is remarkably large when considering that the narrowest linewidth that may be involved pertains to the low-energy subband in the antisymmetric stretching band, which features a FWHM of 23 cm^{-1}. Without even accounting for the width of the symmetric band, this value already yields a dephasing time below 0.5 ps and therewith smaller than the measured coherence decay. Such prolonged coherences are also reported in 2D electronic spectroscopy measurements. Here, vibronic coupling is proposed as the underlying mechanism [124, 125]. In particular, recent studies point out the impact of vibrational modes that are resonant with the energy gaps between excited

electronic states [126, 127]. In accordance with these findings, the coupling to low-lying modes with energies matching the energy gap between ν_{01} and ν_{10} is suggested as the origin of the prolonged coherence in $Ba(ClO_4)_2$ trihydrate. A possible mode in the appropriate frequency range was previously put in relation to symmetry breaking.

In conclusion, the present chapter presents first pump–probe measurements on the excited states of the OH stretching vibration in cyclic H_2O trimers in the solid phase. The observations are in accordance with quantum chemical simulations and group theoretical considerations that are conducted in the frame of $S6$ symmetry. The data points towards localization of initially delocalized stretching modes, which occurs after dynamic breaking of the symmetry. After individual excitation of the antisymmetric stretching band, relaxation in the symmetric stretch was observed and vice versa. To extract the respective rates, a kinetic model was developed and successfully applied to determine the relaxation rates k_{sa} and k_{as} to be approximately $(1.4\ \text{ps})^{-1}$ and $(2.8\ \text{ps})^{-1}$. The decay of the total population yields an effective lifetime of $T_1 = (8 \pm 1)$ ps. After simultaneous excitation of ν_{01} and ν_{10}, quantum beats were observed via a combination band ν_{11} that was found to dominate the overtone spectrum. The beat frequency shows an initial chirp towards smaller frequencies, which could be attributed to dynamic symmetry breaking and the associated localization of the OH stretching mode. The final beat frequency of roughly 52 cm^{-1} is in good accordance with the energy distance between ν_{01} and ν_{10}. From the beat decay, an unusually long coherence lifetime of (0.60 ± 0.07) ps is extracted, which may be based on the coupling between the stretching modes and low-lying vibrations. Note that extended theoretical work is required in order to reconcile all of the above findings, including (i) the initial redshift in the high-energy ESA, (ii) the ratio between the relaxation rates k_{sa} and k_{as}, (iii) the chirp in the quantum beats, and (iv) the prolonged coherence of ν_{01} and ν_{10}.

5.3 Relaxation of the OH Stretching Vibration in Isotopically Diluted Ice I_h

While chapters 5.1 and 5.2 were concerned with (quasi-)isolated water molecules and small water clusters, the present chapter shall continue the observations on aqueous hydrates by building a bridge to the relaxation dynamics in isotopically diluted ice I_h. The investigations on ice are crosschecked with data gained in barium perchlorate ($Ba(ClO_4)_2$) trihydrate and sodium chloride (NaCl) dihydrate. This procedure once more emphasizes the utility of aqueous salt hydrates as a construction kit to remodel the interactions found in bulk water and ice.

In the past decades, ice was very comprehensively studied by means of neutron scattering, and linear IR and Raman spectroscopy [8, 67, 128–132]. In contrast, nonlinear optical techniques, such as pump–probe, fall behind in this field. However, especially nonlinear spectroscopy on the OH (or OD) stretching vibration should be suitable to provide significant insights since the stretching vibration's properties are closely linked to its environment. By preparing a low-molar solution of HDO:D_2O, resonant energy transfer between individual OH groups and the accompanied rapid dissipation of the vibrational energy can be strongly suppressed. Relaxation therefore is forced to proceed locally and hence is very sensitive to the local environment of the respective OH group [51].

Previous publications point out the important role of the bend mode, especially its overtone, in the relaxation dynamics of the OH stretching vibration in HDO:D_2O [51, 133]. Nevertheless, the quantitative contribution accounted for by the bending overtone is heavily discussed. While some authors identify it as the dominant relaxation channel [94, 134], others emphasize the role of other possible accepting modes, like the O–H$\cdots$O hydrogen bond or the modes provided by the D_2O solvent [96, 135, 136]. The following investigations shall verify whether the OH stretch relaxation dynamics in HDO:D_2O ice can be explained by one dominant (intramolecular) accepting mode in the first place and whether this mode could be the bending overtone. For this purpose, the ice dynamics are put in relation to those measured in $Ba(ClO_4)_2$ trihydrate and NaCl dihydrate.

5.3.1 Population Relaxation in Isotopically Diluted Ice I_h

The relaxation dynamics of the OH stretching vibration shown within this chapter are conducted by pump–probe spectroscopy. The time-resolved data is exclusively processed in the ESA from the first to the second excited state, which is a direct measure of the population relaxation in the first excited state. This approach is preferred over probing in the GSB in order to avoid pump induced stray signals and to minimize coherent effects that can arise from the spectral overlap of pump and probe pulses (see section 4.3.1). However, since there is still indication of coherent artifacts in some of the data, the transients are fitted by biexponential decays, whereby an ancillary short time constant is assigned to cover initial coherent effects and prevent the actual population decay time from being falsified. In the following discussion, ν_{OH} and ν_{OD} denote the OH and OD stretching modes, and δ_{HDO} represents the HDO bending mode.

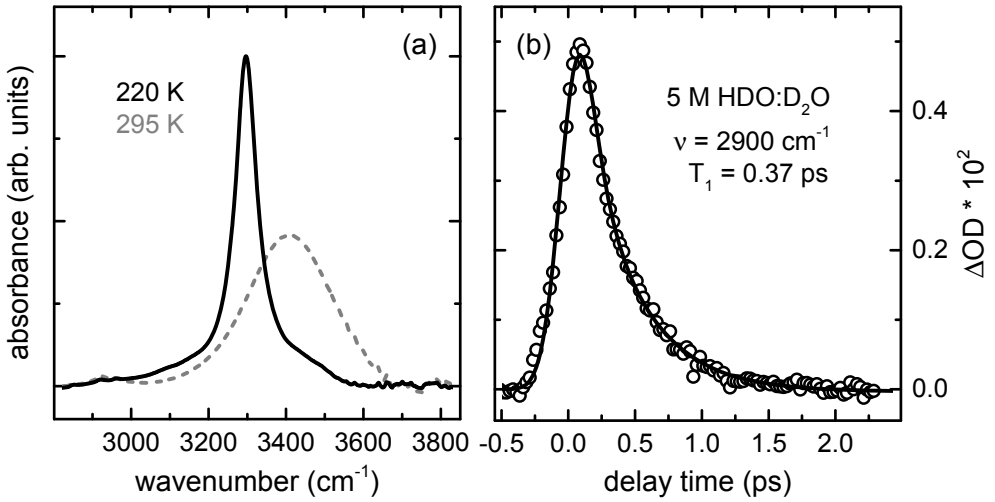

FIGURE 5.10: (a) Normalized FTIR spectra of the OH stretching region in 5 M HDO:D_2O in the liquid and solid phase at 295 K (gray-dashed) and 220 K (black). (b) Respective pump–probe transient (circles) and fit (solid) measured in the ESA at 2900 cm^{-1} at 220 K. The data delivers an average lifetime of 0.37 ps.

The OH stretching region of a crystalline sample consisting of 5M HDO:D_2O obtained at a sample temperature of 220 K is given in Fig. 5.10 (a). It shows a relatively broad absorption band at 3296 cm^{-1}, which exhibits a FWHM of roughly 70 cm^{-1}. In a 5 molar solution, on average, about every eleventh molecule contains an OH group which vindicates the assumption that there is no second OH group in the direct vicinity of an HDO molecule and that resonant energy transfer between individual OH groups can to a large extent

be excluded. The bend fundamental in liquid HDO lies around 1450 cm^{-1} [137, 138]. Since the bending mode is generally less sensitive to its molecular environment and less affected by different degrees of hydrogen bonding, this value can also be applied in the solid phase [139–141]. For the same reasons, the bending can be well approached by a harmonic potential, placing its overtone $\delta_{HDO} = 2$ at roughly 2900 cm^{-1}. Being located well between the ν_{OD} (centered around 2400 cm^{-1}) and the ν_{OH} band, it represents the energetically closest mode to the latter and therefore constitutes the most obvious deexcitation channel when considering intramolecular relaxation of the OH stretch.

As in H_2O, the ESA due to the $\nu_{OH} = 1 \rightarrow 2$ transition in isotopically diluted ice I_h is very flat and broad with a linewidth of the order of 350 cm^{-1}, which exceeds that of the $\nu_{OH} = 0 \rightarrow 1$ absorption by a factor of approximately 5 [51, 103]. Several efforts have been made to theoretically model the broad excited state spectrum. In 2008, Bakker et al. applied a Lippincott-Schroeder model and concluded that the extreme broadening is based on the very short lifetime of the $\nu_{OH} = 2$ state, which is due to resonance between the redshifted $\nu_{OH} = 1 \rightarrow 2$ transition and the bend overtone [103]. In a more recent publication, Hamm and coworkers succeeded in reproducing the spectrum by including the quantum mechanical delocalization of the vibrational wavefunction along the O–O direction. The latter results in a wide range of oxygen-oxygen distances and gives rise to Franck-Condon-like transitions over a broad frequency range. Their investigations gave evidence of strong mode mixing in the $\nu_{OH} = 2$ state that leads to the collapse of an adiabatic representation. Non-adiabatic coupling then causes the diverse Franck-Condon transitions into the $\nu_{OH} = 2$ manifold to couple to a quasi-continuum of states from $\nu_{OH} = 0$ and $\nu_{OH} = 1$. As a consequence, the transitions spread out, which results in a broad excited state spectrum [51]. In principle, the approach of Hamm et al. is preferred over that of Bakker et al. because it is also conform with (i) the broadening of the $1 \rightarrow 2$ transition of the OH stretch in H_2O ice, where the bend overtone coincides with the OH stretching fundamental and with (ii) the respective broadening of the OD stretch of HDO:H_2O ice, where there is no longer resonance to the bend overtone.

An exemplary transient measured in the ESA at 2900 cm^{-1} is depicted in Fig. 5.10 (b). Fitting of several data sets yields an average lifetime of (0.37 ± 0.05) ps. In the following, these dynamics shall be compared to those measured in $Ba(ClO_4)_2$ trihydrate and NaCl dihydrate, each prepared with 5M HDO:D_2O as a solvent.

5.3.2 Supplementary Investigations on $Ba(ClO_4)_2$ Trihydrate and NaCl Dihydrate

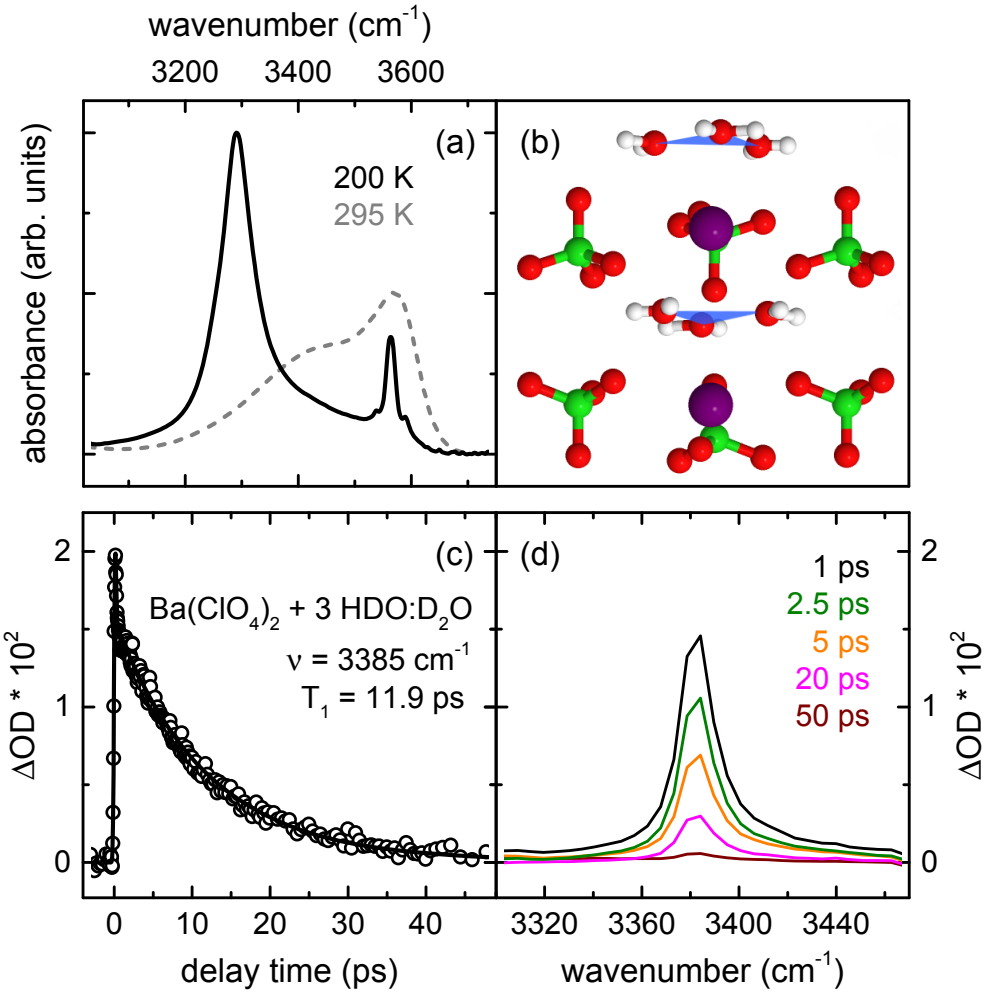

FIGURE 5.11: (a) FTIR spectra of the OH stretching region of $Ba(ClO_4)_2$ dissolved in 5 M $HDO:D_2O$ in the liquid and solid phase at 295 K (gray-dashed) and 200 K (black). (b) Crystal structure of $Ba(ClO_4)_2$ trihydrate (Ba in purple, Cl in green, H in white, and O in red). The blue triangles indicate water trimers that are mutually well separated by planes containing salt ions. (c) Transient measured in the ESA at 3385 cm^{-1}. Fitting yields a lifetime of 11.9 ps. (d) Transient spectra of the ESA at several delay times.

Since a detailed analysis of the crystal structure and symmetry properties of $Ba(ClO_4)_2$ trihydrate can be found in chapter 5.2, only the key features are summarized below. As displayed in Fig. 5.11 (b), in $Ba(ClO_4)_2$ trihydrate, planes containing water molecules alternate with planes consisting of Ba^{2+} and ClO_4^- ions. The water molecules arrange in cyclic trimers (blue triangles) within which there is virtually no hydrogen bonding among the water molecules. In a sample prepared with pure H_2O, strong transition dipole

coupling via the twice positively charged Ba^{2+} cations can lead to delocalization of the stretching mode on adjacent trimers that are symmetry related by inversion on the Ba atoms. In contrast, by usage of 5 M HDO:D_2O as a solvent, one can assume that there is not more than one OH group among the six molecules of two next water trimers and that resonant energy transfer between different HDO molecules can be excluded. A steady state spectrum of the OH stretching region of $Ba(ClO_4)_2 \cdot$ 5M HDO:D_2O at a temperature of 200 K is shown in Fig. 5.11 (a). Low solubility yields a pronounced absorption of an additional ice phase around 3300 cm^{-1}. The feature due to the HDO molecules bound in the hydrate crystal is located at 3564 cm^{-1} and exhibits a FWHM of roughly 20 cm^{-1}. Small sidebands that occur around the HDO hydrate feature may be due to a splitting of the hydrate band as a consequence of one water molecule's asymmetric environment in the hydrate crystal. Correspondingly, previous studies at similar temperature in partially deuterated $Ba(ClO_4)_2 \cdot 3H_2O$ report a splitting of the OD stretching, which is of the order of 10 cm^{-1} [119]. However, since the present side peaks exhibit an energy distance of the order of 50 cm^{-1}, they may more likely be attributed to a contamination with a small amount of H_2O. In the following discussion, only the middle peak is of interest. The large blueshift with respect to the ice absorption indicates minor coupling to neighboring perchlorate ions via weak hydrogen bonds. Weak coupling along with the absence of resonant energy transfer points towards intramolecular relaxation via the bend overtone being the most obvious relaxation pathway. A pump–probe transient measured in the maximum of the excited state absorption at (3385 $\pm$ 5) cm^{-1} is shown in Fig. 5.11 (c). Fitting delivers a population lifetime of the first excited state of (11.9 $\pm$ 1) ps. Respective transient spectra recorded at different delay times are given in Fig. 5.11 (d). The FWHM of the ESA is (20 $\pm$ 5) cm^{-1} and thus comparable to that of the hydrate feature in the FTIR data in Fig. 5.11 (a). Accordingly, in contrast to HDO:D_2O ice, there is no indication of spectral broadening upon going from the fundamental to the excited state transition.

The crystal structure of NaCl dihydrate is depicted in Fig. 5.12 (b). Four different hydrogen bonds can be found among two different pairs of water molecules. These are three rather short and straight bonds at an average Cl–O distance of 320 pm (bonds 1, 2, and 3) and one slightly bent longer bond with a Cl–O distance of 337 pm (bond 4). Steady state spectra of a sample prepared with 5M HDO:D_2O at 200 K are shown in Fig. 5.12 (a). Besides the well-known ice absorption band, there are two hydrate features, which are related to the different hydrogen bonds. A small one at 3541 cm^{-1} stems from

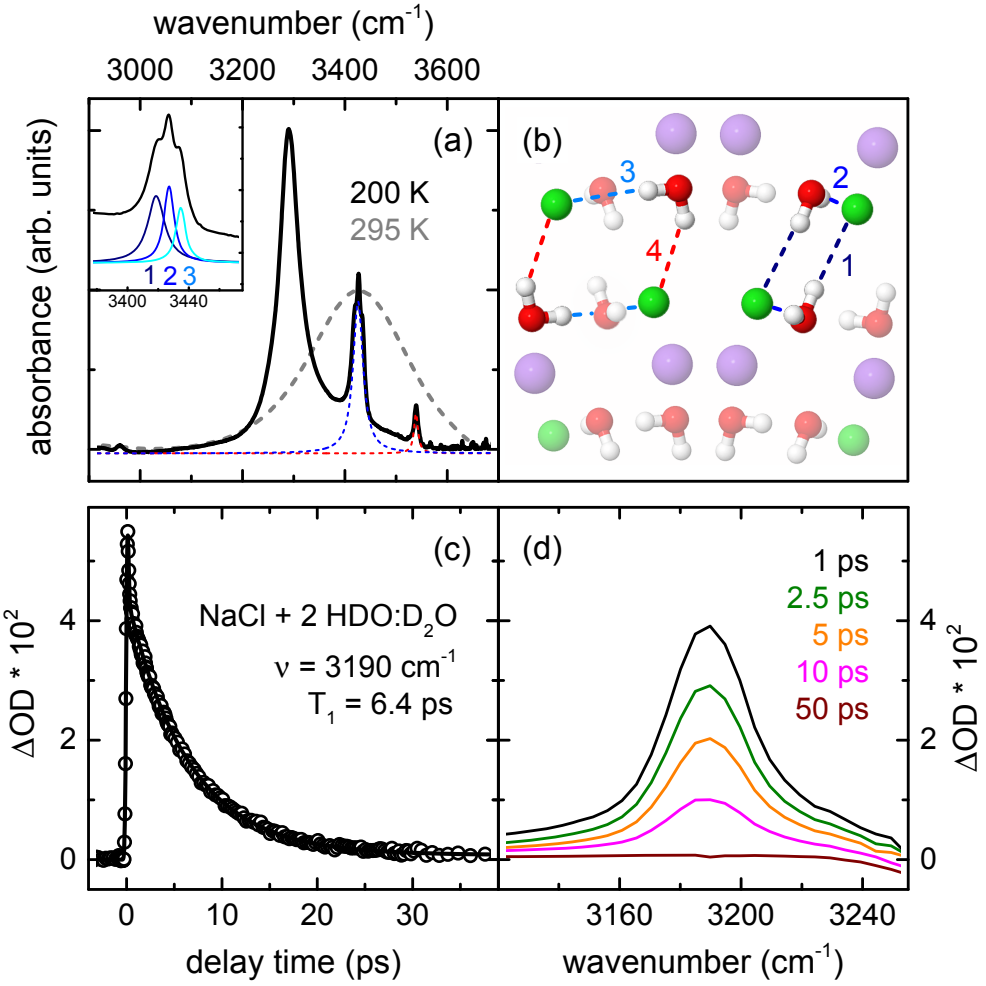

FIGURE 5.12: (a) FTIR spectra of the OH stretching region of NaCl dissolved in 5 M HDO:D_2O in the liquid and solid phase at 295 K (gray-dashed) and 200 K (black). Fitted dashed lines indicate the OH stretching bands due to short straight (blue) and long bent hydrogen bonds (red) at 3426 cm^{-1} and 3539 cm^{-1}. The inset shows the substructure of the low-energy hydrate feature, which is decomposed into three Lorentzian peaks. (b) Crystal structure of NaCl dihydrate (Cl in green, H in white, Na in purple, and O in red). Dashed lines represent the different hydrogen bonds. Bonds 1, 2, and 3 are short straight bonds, while 4 is a long bent one. (c) Transient measured in the ESA at 3190 cm^{-1}. Fitting yields a lifetime of 6.4 ps. (d) Transient spectra of the ESA at several delay times.

the OH groups engaged in the long bent H bonds (dashed red Lorentzian curve), while the more pronounced peak at roughly 3426 cm^{-1} is assigned to the OH groups involved in the short and straight bonds (dashed blue Lorentzian curve). In the following, only the latter absorption will be under investigation. It features a FWHM of (24 ± 3) cm^{-1}. However, a detailed analysis of the feature shows that the peak is splitting into three, which most probably is due to three slightly different hydrogen bond lengths. In the

inset in Fig. 5.12 (a), this substructure is decomposed into three Lorentzian peaks, which are related to Cl–O distances of 319 pm, 320 pm, and 322 pm pertaining to the bonds 1, 2, and 3 in Fig. 5.12 (b). The fitted data is in very good agreement with the measured spectra and delivers peak positions of 3418.5 cm^{-1}, 3427 cm^{-1}, and 3434.5 cm^{-1} with FWHMs of 13.5 cm^{-1}, 8 cm^{-1}, and 7.5 cm^{-1}. Compared to the $Ba(ClO_4)_2$ sample, the smaller blueshift to a center value of about 3426 cm^{-1} is evidence for stronger H bonding to the salt ions. Nonetheless, consisting solely of Na^+ and Cl^- ions, the salt crystal does not supply ν_{OH} with adequate modes for relaxation. Within the two water pairs that couple via two Cl atoms (blue and red-blue squares in Fig. 5.12 (b)) obviously no resonant energy transfer can be achieved since not more than one of the two molecules contains an OH group due to the solvent molarity. So again, intramolecular relaxation via the bending overtone is the most apparent deexcitation mechanism. Excited state dynamics measured at 3190 cm^{-1} are displayed in Fig. 5.12 (c) and reveal a lifetime of the $\nu_{OH} = 1$ state of (6.4 $\pm$ 0.5) ps. Transient pump–probe spectra are depicted in Fig. 5.12 (d). The ESA is located at (3190 $\pm$ 5) cm^{-1} and shows a FWHM of (33 $\pm$ 5) cm^{-1} that indicates little broadening with respect to the fundamental absorption, when the latter is considered as one single band.

5.3.3 Evaluation of the Relaxation Channels

In each of the hydrate and ice samples presented above, the bend overtone is identified to be the most likely deexcitation channel for the OH stretch mode. As outlined before, δ_{HDO} exhibits low sensitivity to its chemical environment and can therefore be assumed to be the same in the three species. In the hydrate samples, the relaxation is considered to proceed intramolecularly, while in isotopically diluted Ice I_h, one has to account for a conceivable influence of the modes provided by the surrounding D_2O molecules. Recent theoretical calculations by Lawrence et al. showed that for each OH stretch excitation in liquid HDO in D_2O, 0.26 quanta of solvent stretch are excited [142]. Their computations, however, also state that this does not greatly affect the $\nu_{OH} = 1$ lifetime and that the relaxation is dominated by the transition to the bend overtone. This vindicates a comparison of the OH stretching dynamics of the three samples with regard to intramolecular relaxation channels.

When assuming deexciation through one single mode, the corresponding rate k can be expressed by Fermi's golden rule, which has already been

discussed in section 3.4. It can be written in the form

$$k = \frac{2\pi}{\hbar} \int d\omega |\langle f| \hat{V}_{\nu,a} |i\rangle|^2 g_\nu(\omega)\rho_a(\omega), \tag{5.7}$$

with $\langle f| \hat{V}_{\nu,a} |i\rangle$ representing the coupling between the initial and final states, i and f. $g_\nu(\omega)$ is the spectral distribution of the OH stretching vibration, and $\rho_a(\omega)$ is the acceptor mode density of states. Assuming the latter to be proportional to its spectral distribution $g_a(\omega)$ and the coupling strength to be independent of the frequency, one gets

$$k = c\,|\langle f| \hat{V}_{\nu,a} |i\rangle|^2 \int d\omega g_\nu(\omega) g_a(\omega), \tag{5.8}$$

where c is a constant of proportionality. In the case of Lorentzian distributions, the overlap integral can be solved analytically and one arrives at

$$k = c\,|\langle f| \hat{V}_{\nu,a} |i\rangle|^2 \frac{2}{\pi} \frac{\Gamma_\nu + \Gamma_a}{4(\omega_\nu - \omega_a)^2 + (\Gamma_\nu + \Gamma_a)^2}, \tag{5.9}$$

where ω_ν and ω_a are the center frequencies of the OH stretch mode and the accepting mode, and Γ_ν and Γ_a represent the corresponding FWHMs. Note that the same data processing has been used by Bakker et al. in their investigations on the OD stretch in $LiNO_3 \cdot (HDO{+}2H_2O)$ [117].
Insertion of the spectral positions, FWHMs of the FTIR data, and the $\nu_{OH} = 1$ relaxation times of $HDO{:}D_2O$ ice, $Ba(ClO_4)_2 \cdot (HDO{+}2D_2O)$, and $NaCl \cdot (HDO{+}D_2O)$ yields spectral positions and bandwidths of possible accepting modes.[12] Here, the same coupling strength is assumed for the three different species, which is reasonable when expecting intramolecular relaxation. The constant c is only related to the accepting mode and hence independent of the sample. Note that the computations do not provide absolute values of the coupling strength since c cannot be canceled out. As it is not absolutely clear whether the substructure of the NaCl hydrate peak is due to the different hydrogen bond types, independent computations were processed for one single absorption band at 3426 cm^{-1} with a FWHM of 24 cm^{-1} and for each of the three Lorentzian peaks that are depicted in the inset in Fig. 5.12 (a).
Assuming a single broad absorption feature in the NaCl sample, the calculations do not provide any real-valued and physically sensible results for Γ_a and ω_a. Even variation of the input parameters within the error margins

[12] Since literature reports widely diverging values for the FWHM of the absorption band in isotopically diluted ice [103, 143], in the following, values ranging from 50 cm^{-1} to 90 cm^{-1} were tested.

does not yield reasonable values. In contrast, accounting for the subdivision of the NaCl hydrate feature and performing individual calculations for the three Lorentzian peaks in all three cases leads to accepting modes which are situated between 3170 cm^{-1} and 3230 cm^{-1} with FWHMs ranging from unrealistically narrow up to 25 cm^{-1}. Comparing the average spectral position of about 3200 cm^{-1} with that expected for the bend overtone at approximately 2900 cm^{-1} reveals an energy mismatch of the order of 300 cm^{-1}, which contradicts the assumption of the bend overtone being the exclusive dominant deexcitation channel. Note that in ice, a lattice mode around 300 cm^{-1} is reported [144, 145]. The latter can in principle account for the difference between the bend overtone and the computed mode. However, the relatively narrow calculated bandwidths and the very different crystal lattices of the ice and hydrate samples argue against an identical accepting mode, which is composed of the bend overtone and lattice vibrations. Apart from that, isolated HDO molecules do neither provide any vibrational bands nor combination tones around 3200 cm^{-1}, which strongly points towards the presence of additional relaxation channels.

When considering different accepting modes, one has to distinguish between intra- and intermolecular relaxation. A conceivable additional intramolecular mode is the OD stretching vibration around 2400 cm^{-1}. Nevertheless, comparing the bandwidths of the fundamental OH stretching features reveals a non-negligible spectral broadening when going from the hydrate to the ice species. This broadening cannot be explained in a straightforward way when only accounting for intramolecular accepting modes since these are of the same nature in the hydrate and ice species. Obviously, the main difference between the samples is the strong coupling to the D_2O solvent via strong hydrogen bonds in isotopically diluted ice. In view of this, the spectral broadening rather suggests inclusion of the solvent modes in the relaxation process in crystalline HDO:D_2O. This conclusion is in good agreement with a recent publication that states that the OH stretching in liquid-phase HDO:D_2O does not relax exclusively through the bend overtone [96]. The 2D-IR experiments rather show that primarily the strongly hydrogen bonded OH groups couple to the bend overtone that for its part transfers the energy to either the bend fundamental or the deuteroxyl stretch. Conversely, the weakly H bonded hydroxyl groups are expected to relax to the bend only after forming a strong hydrogen bond or alternatively to relax directly into the solvent modes.

Concluding this section, it is emphasized that the bend overtone certainly plays a substantial role in the relaxation of the OH stretching dynamics. However, a comparison between 5M HDO:D_2O ice and hydrate data shows that the observed dynamics cannot be explained with the bend overtone as the only dominant relaxation channel. Steady state spectra and transient data rather indicate the involvement of the D_2O solvent modes in the relaxation dynamics of the ice sample. These observations underpin the complexity of the processes in bulk ice, which already yields ambiguous data in isotopically diluted ice I_h. From this, one gets a first impression of the intricacy when it comes to neat H_2O, where resonant energy transfer between different water molecules constitutes an additional substantial relaxation mechanism.

5.4 Ice-Like Spectral and Dynamic Behavior due to a Strong Hydrogen Bond in $LiNO_3$ Trihydrate

The previous chapter focused on the relaxation dynamics in isotopically diluted ice I_h and exposed its complicated relaxation dynamics. In undiluted H_2O ice (neat ice) and hydrate samples that are prepared with pure H_2O, the presence of neighboring H_2O molecules additionally allows for resonant energy transfer. Moreover, Fermi resonance to the H_2O bend overtone distinctly affects the relaxation dynamics. These effects further complicate the investigations, and a comprehensive treatment demands more sophisticated methods and theoretical models. However, the degrees of freedom can be restricted when comparing similar systems: one prepared with pure H_2O and one with low-molar HDO:D_2O. Especially, the ice-like behavior due to a strong hydrogen bond in $LiNO_3$ trihydrate shall be worked out in this section.

5.4.1 Impact of the Crystal Matrix onto the OH Stretching Dynamics

The investigations in chapter 5.3 already showed that a comparison to the interactions found in crystalline hydrate samples can yield valuable information on the processes found in ice. Apart from that, divergent spectral and transient data indicate that the relaxation processes also strongly depend on the crystal matrices that contain the water molecules. This is particularly evident when comparing two actually very similar hydrates, which are barium perchlorate ($Ba(ClO_4)_2$) trihydrate and lithium perchlorate ($LiClO_4$) trihydrate, both prepared with a 5M HDO:D_2O solvent. The crystal structure of $LiClO_4$ trihydrate and the respective FTIR and time-resolved measurements can be found in App. A.2. Both species feature mutually well separated three-rings of water molecules, whereby vertically next rings are twisted by an angle of 60° (see Fig. 5.4 (c)). The O–O distances within one ring are also very similar for the two samples ($\approx$ 285 pm). Nonetheless, the arrangement of the salt ions is different in a way that there are well separated layers containing either salt ions or water molecules in $Ba(ClO_4)_2$ trihydrate, whereas the salt and water layers are meshed in $LiClO_4$ trihydrate. This results in stronger coupling to the perchlorate ions via stronger hydrogen bonds in the case of $LiClO_4$. The corresponding OH stretching frequency is thus shifted

from 3564 cm^{-1} in the Ba species to 3552 cm^{-1} in the Li species. Moreover, the distance between vertically adjacent water trimers is shortened from 483 pm to 273 pm in the $LiClO_4$ trihydrate. These differences result in a lifetime shortening from (11.9 $\pm$ 1) ps in the Ba sample to (6.6 $\pm$ 1) ps in the Li sample. The divergent spectral and dynamical properties of these two actually quite similar species immediately unveil the problems entailed when putting different samples in relation.
However, effects due to the crystal matrix can be overcome when comparing the properties of H_2O and HDO molecules embedded in the very same crystal. Considering the relaxation dynamics, the change in the population lifetime upon going from deuterated to pure H_2O samples can be expressed by a rate that is characteristic for the respective crystal. Generally, the dynamics in the corresponding H_2O sample are faster and one can introduce an acceleration rate K_{acc} that is calculated as the difference between the reciprocal OH stretching lifetimes of the related H_2O and deuterated samples:

$$K_{acc} = k_{H_2O} - k_{HDO} = (1/T_1)_{H_2O} - (1/T_1)_{HDO} \tag{5.10}$$

In the end, spectral changes and rates can be cross-checked to map the relaxation dynamics and unfold differences and similarities of the various systems. In the following, this is done for ice I_h and several salt hydrates. In particular, the ice-like spectral and dynamical properties of $LiNO_3$ trihydrate will be scrutinized in more detail.

5.4.2 A Comparison between Neat and Isotopically Diluted Samples

As in the previous chapters, the following steady-state data is recorded by a conventional FTIR spectrometer, and the time-resolved data is measured in standard pump–probe experiments. The dynamical evolution of the OH stretching vibration again is measured in the ESA from the first to the second excited state. The extracted transients are fitted applying two independent exponential decays: One is used to tailor initial coherent effects, while the other one represents the actual population lifetime. The following abbreviations are applied for the different vibrations: The common designations ν_1 and ν_3 represent symmetric and antisymmetric stretching in the H_2O samples, and ν_{HDO} denotes the OH stretching in the deuterated samples.

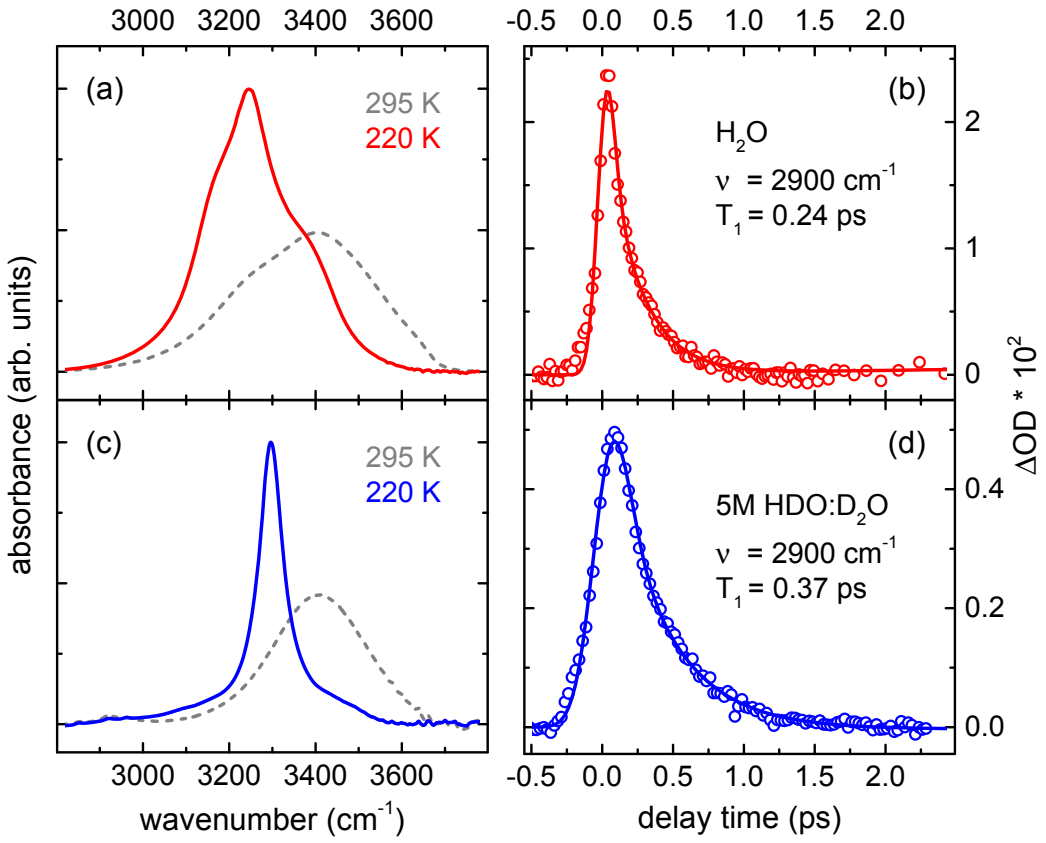

FIGURE 5.13: (a) Normalized FTIR spectra of the OH stretching region in H_2O in the liquid and solid phase at 295 K (dashed gray) and 220 K (red). (b) Pump–probe transient (circles) and fit (solid line) measured in the ESA of H_2O ice at 2900 cm^{-1} at a sample temperature of 220 K. The data shows a population lifetime of 0.24 ps. (c) OH stretch region of 5M HDO:D_2O in the liquid and solid phase at 295 K (dashed gray) and 220 K (red). (d) Respective pump–probe transient (circles) and fit (solid line) recorded in the ESA at 2900 cm^{-1} at 220 K. The data yields a population relaxation time of 0.37 ps.

Fig. 5.13 (a) depicts the OH stretching region of ordinary H_2O ice at 220 K. It displays a broad absorption band that features a characteristic substructure, which is subject of continuing discussions. Besides the contributions of the symmetric and antisymmetric stretching vibration, usually three factors are listed that crucially impact the band's shape. These are (i) delocalized intermolecular vibrations (vibrational excitons) that form when the excited OH stretch transition dipoles add up as a consequence of strong intra- and intermolecular coupling [143, 146], (ii) a contribution of the bend overtone that is enhanced by Fermi resonance with the OH stretching vibration [147, 148], and (iii) an exciton–phonon coupling, meaning the coupling to other non-resonant excitations, such as low-frequency intermolecular modes, like phonons [132, 149].

The ESA of neat ice I_h is very flat and broad. Its shape is known from 2D-IR measurements [149, 150]. Although a generally accepted and comprehensive description of the ESA's spectral properties is lacking to this day, one can bring forward the same arguments as for isotopically diluted ice I_h in chapter 5.3. Here, it was argued that strong mode mixing leads to a collapse of an adiabatic representation. Non-adiabatic coupling then causes the diverse Franck-Condon transitions into the ν_{HDO} = 2 multifold to spread out, resulting in an unusually broad range of excited state transitions that spans over more than 2000 cm^{-1} [51]. In Fig. 5.13 (b), a transient measured at 2900 cm^{-1} is given. A set of statistics delivers an averaged population relaxation time of (0.24 ± 0.05) ps, which is in good accordance with the corresponding times for liquid water and ice that are found in the literature [90, 151].
Respective data measured in 5 M HDO:D_2O at 220 K has already been discussed in the previous chapter. The steady-state spectrum in Fig. 5.13 (c) shows the ν_{HDO} band that is centered at 3295 cm^{-1} and exhibits a FWHM of roughly 70 cm^{-1}. A pump–probe transient recorded in the ESA at 2900 cm^{-1} is depicted in Fig. 5.13 (d). Several measurements yield an average population lifetime of (0.37 ± 0.05) ps.
The first thing that is striking when comparing the neat and isotopically diluted ice samples is the much narrower fundamental OH stretching band in the deuterated species that cannot solely be explained by the lack of splitting into symmetric and antisymmetric stretching. In addition, the absence of resonant energy transfer and the related local character of the OH stretching mode in HDO:D_2O have to be considered. Moreover, only minor effects due to Fermi resonance to the HDO bend overtone are expected. The latter is located around 2900 cm^{-1}, which makes up an energy distance of about 400 cm^{-1} to the ν_{HDO} band. In contrast, in H_2O ice, the bend overtone is situated at roughly 3300 cm^{-1} and coincides with the stretching band, which can heavily influence the spectral pattern. Referring to the dynamics, a distinct acceleration is observed upon going from HDO:D_2O to H_2O. According to Eq. 5.10, it can be quantified by an acceleration rate K_{acc} of 1.46 ps^{-1}. At this point, one cannot distinctly say whether this accelerated dynamics are due to effects of resonant energy transfer and accompanied delocalization of the OH stretching vibration, Fermi resonance with the bend overtone, or a combination of both.
To evaluate the acceleration rate in ice, similar measurements were performed on several aqueous salt hydrates. Data gained in $Ba(ClO_4)_2$ trihydrate has already been shown and a detailed analysis can be looked up in chapters 5.2 and 5.3. The appropriate lifetimes at a sample temperature of 200 K are

(11.9 ± 1) ps and (8 ± 1) ps for deuterated and pure H_2O samples. This results in a minor acceleration rate upon going from an HDO:D_2O to a H_2O solvent of K_{acc} = 0.04 ps^{-1}. In addition to the NaCl · (HDO+D_2O) data that is shown in the previous chapter, measurements were also performed in NaCl · $2H_2O$. Note that here again only the hydrate absorption due to the straight and short H bonds is considered. At 200 K, one delivers an OH stretching population relaxation rate of (1.9 ± 0.2) ps. From a comparison to the respective ν_{HDO} lifetime of (6.4 ± 0.5) ps an acceleration rate of K_{acc} = 0.37 ps^{-1} is extracted. The latter exceeds the one found in the $Ba(ClO_4)_2$ species by almost one order of magnitude. In $Ba(ClO_4)_2$ trihydrate, due to very weak hydrogen bonds, the OH stretching bands show a large blueshift: ν_1 and ν_3 are located at 3535 cm^{-1} and 3588 cm^{-1}. In NaCl dihydrate, however, the H bond interaction is stronger and the hydrate features are found at lower energies. Here, symmetric and antisymmetric H_2O stretching are expected to split around the HDO feature at 3426 cm^{-1} (see Fig. 5.12). Thus, a smaller energy distance to the H_2O bending overtone can explain the bigger K_{acc} in NaCl · $2H_2O$ when comparing NaCl and $Ba(ClO_4)_2$ samples.

5.4.3 Investigations on $LiNO_3$ Trihydrate

To figure out whether the value of K_{acc} systematically gets higher with increasing hydrogen bond strength, a third hydrate sample is investigated. In $LiNO_3$ trihydrate, a very strong ice-like hydrogen bond between two water molecules is reported [22, 117]. The corresponding dynamics shall be investigated in the following.

Spectra and dynamics of deuterated $LiNO_3$ trihydrate have been subject of earlier measurements at our university chair and have already been published [22]. However, the data shown in this chapter was independently recorded since the new setup offers improved time resolution. The crystal structure of $LiNO_3$ trihydrate is known from X-ray and neutron diffraction data [152, 153] and is displayed in Fig. 5.14 (a). The hydrate water molecules form three different types of H bonding, which are contained in two perpendicular planes. A strong ice-like hydrogen bond is developed between the water molecules a and b and the molecules b and c, respectively (highlighted by dashed lines). Note that the corresponding O–O distance of 282 pm is very similar to the one found in bulk ice (275 pm). In the same plane, a rather weak bond is found between the second OH group of a (or c) and the nearest oxygen atom of the neighboring nitrate anion. The third type of bond

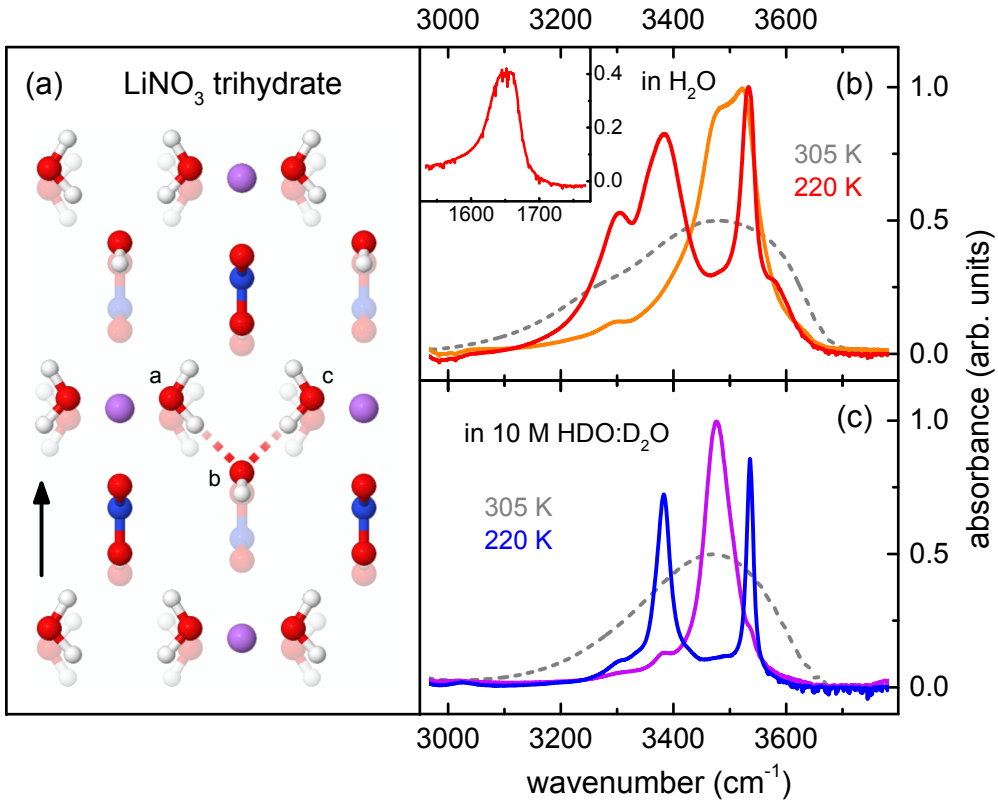

FIGURE 5.14: (a) Crystal structure of $LiNO_3$ trihydrate (H in white, Li in purple, N in blue, and O in red). The water molecules a and c form strong hydrogen bonds to molecule b on the one side (dashed lines) and weak hydrogen bonds to the next oxygen of a nitrate anion on the other side. Bifurcated hydrogen bonds are developed between the water molecules that lie perpendicular to the plane of the figure and nearby nitrate anions. Laser light propagating in the direction indicated by the black arrow can individually excite the water molecules in the two planes. (b) Normalized FTIR spectra of $LiNO_3 \cdot 3H_2O$ in the solid phase at 220 K (red and orange) and in the liquid phase at 305 K (dashed gray). Red and orange spectra were recorded applying perpendicular polarizations. The inset shows the H_2O bending mode in the plane of the weak and strong hydrogen bonds. (c) Respective spectra of $LiNO_3 \cdot (HDO{+}2D_2O)$ at 220 K (blue and violet) and 305 K (dashed gray). Blue and violet spectra were recorded with perpendicular polarizations.

lies in a plane perpendicular to the layer of the figure. These are bifurcated bonds of medium energy that form between each of the OH groups of water molecule b and two oxygen atoms of a nearby NO_3^- ion. In the following, special attention shall be devoted to the strong bond.

When the crystal is properly oriented with regard to the direction of the excitation light, the correct polarization yields exclusive excitation of the OH groups involved in the weak and strong hydrogen bonds. Accordingly, perpendicular polarization then solely addresses the oscillators associated

with the bifurcated bonds. This applies to laser light traversing along the vertical direction indicated by the black arrow in Fig. 5.14 (a). Actual experiments showed that usually an area with appropriate orientation can be found within the accessible sample surface. Figs 5.14 (b) and (c) display the corresponding polarization-resolved FTIR spectra of $LiNO_3$ dissolved in H_2O and 10 M HDO:D_2O at 220 K. Each figure shows two spectra that are recorded with perpendicular polarizations. In (c), the two features in the blue curve are situated at 3383 cm^{-1} and 3536 cm^{-1} and exhibit FWHMs of 31 cm^{-1} and 14 cm^{-1}. They are due to the OH groups engaged in the strong and weak hydrogen bonding. A small shoulder at the low-energy end of the peak due to the strong H bonds around 3300 cm^{-1} could not distinctly be assigned. It is not apparent in the perpendicular spectrum (violet) and hence cannot be related to the formation of an ice phase since the excitation in ordinary ice is generally polarization independent. It more likely is due to any kind of local substructure in the hydrate or is a nitrate mode. The inhomogeneously broadened band at 3475 cm^{-1} in the violet spectrum stems from the OH groups involved in the bifurcated hydrogen bond and shows a FWHM of 57 cm^{-1}. Small shoulders occur in the high- and low-energy flank at the spectral positions of the OH stretching vibrations due to the strong and weak hydrogen bonds. This is a result of not perfectly matching polarization and crystal orientation.

In Fig. 5.14 (b), assignment of the individual peaks is more demanding. A comparison of the red spectrum with the blue one in Fig. (c) indicates that the peaks at 3385 cm^{-1} and 3532 cm^{-1} with FWHMs of 101 cm^{-1} and 34 cm^{-1} are due to the strong and weak hydrogen bonds. Note that there is no splitting into symmetric and antisymmetric stretching since the two features pertain to two OH groups of the same water molecule. Their mutual energy distance of about 150 cm^{-1} hinders resonance and decouples the two OH groups, which in turn explains the good energy match to the HDO features. The third absorption around 3290 cm^{-1}, however, is new to the spectrum. It is almost non-existent in the perpendicular spectrum (orange) and thus polarization dependent. Along with the high solubility of $LiNO_3$, this observation argues with the assumption that the feature stems from an additional ice phase. Its energy matches well with twice that of the H_2O bending mode that was found to be at 1650 cm^{-1} (see inset in Fig. 5.14 (b)). A detailed analysis shows that its amplitude accounts for 80 % of the amplitude of the bend fundamental, which is depicted in the inset in Fig. (b). This is in stark contrast to all previous hydrate measurements, where the bend overtone was either of very minor quantity or not apparent at all. Nevertheless, the hydrate peak

due to the strong H bonds at 3385 cm^{-1} lies very close and the enhanced bend overtone thus might be explained by the evocation of Fermi resonance between the two modes. Moreover, associated resonance broadening could explain the spectral broadening of the strong hydrate peak upon going from the deuterated to the pure H_2O sample. A small shoulder around 3575 cm^{-1} occurs on the high-energy flank of the peak of the OH stretching engaged in the weak hydrogen bond. This may be due to a local substructure but could not be distinctly linked to the crystal. The orange curve displays the absorption of the water molecules involved in the bifurcated hydrogen bond. It is centered around 3500 cm^{-1} and is subdivided into two features with a distance of about 50 cm^{-1}. Independent recording of the two hydrate peaks in the red spectrum and the one in the orange spectrum indicates that the same crystal direction as in Fig. 5.14 (c) is observed. As a consequence, the splitting of the absorption band associated with the bifurcated hydrogen bond in the H_2O sample cannot be due to symmetric and antisymmetric stretching since the symmetric vibration cannot be accessed because of its dipole moment being collinear to the direction of the incident laser light. It is more likely that the split-up is evoked by coupling to low-lying intermolecular vibrations. In particular, a wagging mode of the water molecules that has recently been discussed is considered [22]. Since only the OH groups of the water molecules involved in the strong hydrogen bonds are of interest, this discussion is not deepened.

A pump–probe transient measured in the maximum of the ESA of the OH stretching related to the strong hydrogen bond in the H_2O sample recorded at 3070 cm^{-1} is shown in Fig. 5.15 (a). Averaging the fitted time constants of various measurements delivers an OH stretching decay time of (0.40 ± 0.05) ps. Respective transient spectra can be seen in Fig. (b). In contrast to the excited state spectra measured in other hydrate samples, a very broad absorption band is visible. Along with the very fast relaxation time, this strongly resembles the above measurements in ice. Note that due to the high solubility of $LiNO_3$ and the related lack of an ice absorption band in Fig. 5.14 (b), one can exclude that the measured values stem from an additional ice phase in the sample. This is corroborated when comparing the associated transient spectra: The excited state absorption bands in $LiNO_3 \cdot 3H_2O$ and H_2O ice both are generally very broad and flat. However, the ESA in the $LiNO_3$ sample peaks around 3070 cm^{-1}, while that of neat ice was found to have its maximum around 2900 cm^{-1} and to extend to smaller energies.

Corresponding data recorded in the deuterated sample is shown in Figs 5.15 (c) and (d). Here, a population relaxation time of (1.1 ± 0.1) ps is extracted in

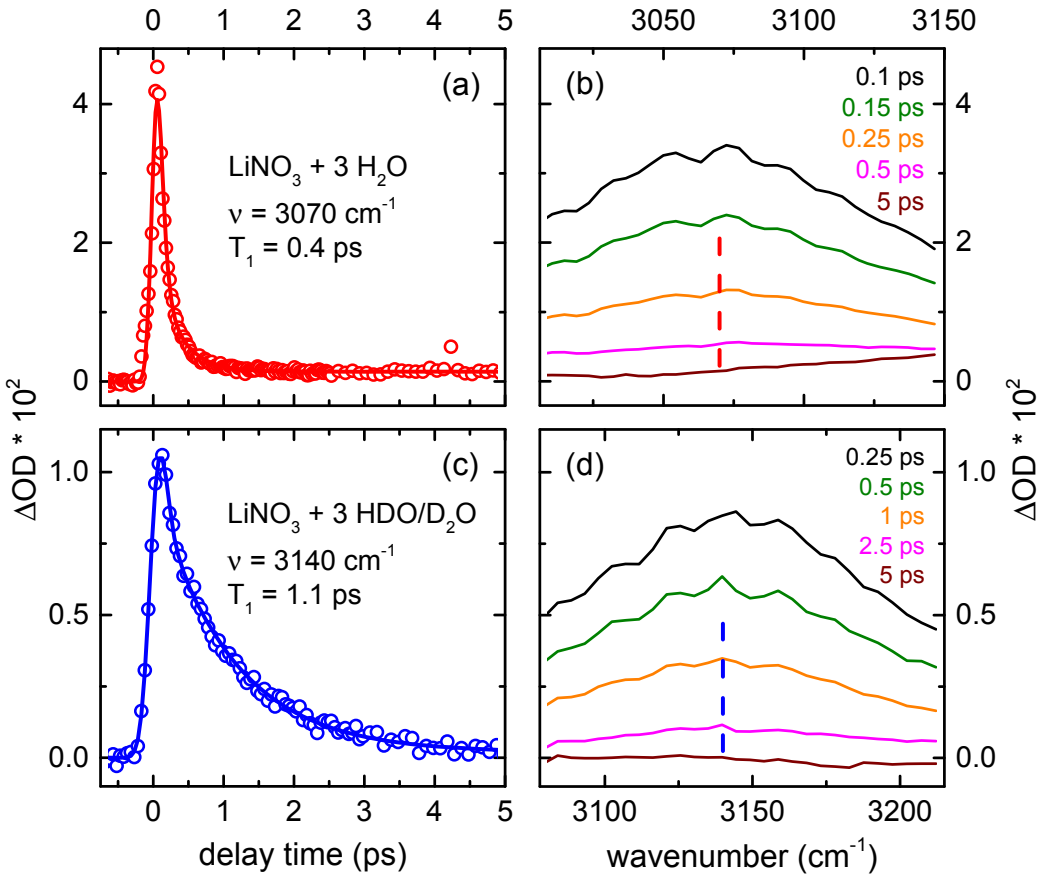

FIGURE 5.15: (a) Pump–probe transient measured in the ESA in $LiNO_3 \cdot 3H_2O$ after excitation of the OH stretching that is associated with the strong hydrogen bond. The curve is recorded at 3070 cm^{-1}, and a population relaxation time of 0.4 ps was extracted from a set of data. (b) Corresponding transient spectra measured at different delay times after pump excitation. (c) Transient measured in the ESA in $LiNO_3 \cdot (HDO + 2D_2O)$ at 3140 cm^{-1}. The data shows a lifetime of 1.1 ps. (d) Related transient spectra recorded at different delays. The dashed lines in (c) and (d) indicate the spectral positions of the corresponding transients in (a) and (b).

the maximum of the ESA at 3140 cm^{-1}, which is in good accordance with the value found in previous measurements that also determined the ESA's FWHM to be (125 ± 10) cm^{-1} [22]. Compared to the population lifetimes in other hydrates, the dynamics of the OH stretching vibrations involved in the strong, bifurcated, and weak hydrogen bonds in $LiNO_3 \cdot (HDO{+}2D_2O)$ are generally very fast (1.1 ps, 1.7 ps, and 2.2 ps [22]). In the case of the weak and bifurcated bonds, this may be due to coupling to appropriate nitrate modes. In contrast, the strong hydrogen bond is formed between two water molecules and thus the coupling to nitrate modes can only account for minor effects. A comparison between the spectral width of the ground state absorption in Fig. 5.14 (c) and that of the respective ESA delivers a magnification

factor of more than 4, which is comparable to that detected in isotopically diluted ice I_h that was determined to be about 5 in the previous chapter. Comparing the transient spectra in Fig. 5.15 (d) to those of the H_2O species in (b) shows that the maximum is blueshifted by roughly 70 cm^{-1} in the deuterated sample. This is in stark contrast to observations in other hydrates, like $Ba(ClO_4)_2$ trihydrate, where the ESAs of ν_1 and ν_3 are distributed symmetrically around that of ν_{HDO}. This observation is particularly interesting since in $LiNO_3$ trihydrate the vibrations of the OH groups of the H_2O molecules in the plane of the strong hydrogen bond are decoupled and should therefore actually be very similar to the ones in the deuterated sample. However, the strong mutual hydrogen bonding of the water molecules a, b, and c in Fig. 5.14 (a) can cause delocalization of the OH stretching on the three molecules in the H_2O sample and therewith yield different spectral properties in the ESA. Turning to the decay times, strong acceleration is observed when going from HDO to H_2O. It can be quantified by an additional rate of K_{acc} = 1.59 ps^{-1} that is even larger than the rate found in ice.

5.4.4 The Smallest Ice Crystal

Summarizing the observations in ice I_h and $LiNO_3$ trihydrate, in both samples very similar spectral broadening is observed when comparing the ν_{HDO} fundamental to the respective ESA. This points towards the same underlying mechanisms and emphasizes the ice-like nature of the strong hydrogen bond in the trihydrate. Being of the order of 1.5 ps^{-1} for both samples, K_{acc} is very comparable for ice and the $LiNO_3$ hydrate. By inversion of this argument, one can conclude that the acceleration rate upon going from the deuterated $LiNO_3$ species to isotopically diluted ice I_h and the rate when proceeding from $LiNO_3 \cdot 3H_2O$ to neat ice I_h are also very similar. The corresponding values are about 1.8 ps^{-1} for the deuterated samples and roughly 1.7 ps^{-1} for the ones prepared with H_2O. Since there is no resonant energy transfer in the deuterated species, the former rate must be due to a more effective coupling to low-lying modes, which most probably are the bend overtone and the D_2O solvent modes. The equality of the rates further suggests that coupling to lower-energy modes is also the decisive mechanism when comparing the two H_2O species. Concerning the acceleration rate K_{acc}, one can deduce that this rate is due to resonant coupling between the involved water molecules. Recent studies explained the different lifetimes occurring in ice samples with varying degree of deuteration by Förster energy transfer to the six nearest OH groups [90]. However, in $Ba(ClO_4)_2$ trihydrate, the acceleration rate is

very small, although the transition dipole coupling via the Ba^{2+} ions is very pronounced. This suggests that effects like Förster resonance transfer and other radiation-free dipole interactions only play a minor role. Along with the findings in $LiNO_3$ trihydrate, resonant coupling via the strong hydrogen bond is suggested as the origin of the large value of K_{acc} in ice. All things considered, there is striking resemblance between the ice and $LiNO_3$ data. The formation of strong hydrogen bonds in both cases yields (i) very fast OH stretching relaxation, (ii) similar spectral broadening upon going from the fundamental to the excited state absorption in the deuterated samples, and (iii) comparable acceleration upon going from samples prepared with $HDO:D_2O$ to ones prepared with H_2O. This indicates that the three water molecules a, b, and c in Fig. 5.14 (a) suffice to mimic the spectral and dynamical properties of ordinary ice I_h. As far as the vibrational properties are concerned, one can thus say that the smallest ice crystal, as found in $LiNO_3$ trihydrate, consists of not more than three water molecules.

Chapter 6

Conclusion and Outlook

The ambition of this thesis is to contribute to a better understanding of water and its hydrogen bonding network. In liquid water, a multitude of different H bond lengths, angles, and types results in a broad and structureless OH stretch band. As outlined in section 2.3, the composition of the latter still is heavily discussed. Although the structure of water has been investigated comprehensively by means of NMR, X-ray and neutron diffraction, the very limited time resolution of these methods strongly hinders a correlation between structural features and the ultrafast dynamics. Generally, when dealing with complex systems, it is a common approach to start from a simpler one that only addresses sub-aspects of the full problem. Subsequently, one can move towards more sophisticated samples to finally end up at the system of actual interest. Here, (quasi-)isolated water molecules are chosen as a starting point. Next, the interaction between water molecules is gradually increased by investigating small water clusters. Thereby, kind and strength of the interactions can be controlled by the proper selection of the sample. Commencing with a sample that features virtually no hydrogen bonds between the individual water molecules of one cluster, in the end, a sample that exhibits very strong ice-like H bonds is presented. The findings on aqueous salt hydrates first are put in relation to isotopically diluted ice and finally a bridge is built to the characteristics of neat ice.

To perform successful measurements, the basic prerequisite is a working system that fully meets the given requirements. For this purpose, a new setup for two-color pump–probe spectroscopy was put into operation. The core pieces are two optical parametric amplifiers that are applied to provide the desired IR pulses: A recently developed hybrid technique of OPA delivers tunable μJ pulses that can be shaped by a spectral selector. In addition, spectrally ultrabroad probe pulses are generated in a one-stage OPA. Altogether, the setup exhibits a time resolution of sub-100 fs and is capable of resolving even the very fast OH stretching dynamics in H_2O ice. In the framework

of this thesis, a third amplifier was implemented to perform three-pulse experiments. The latter is similar to the pump NOPA and was successfully applied to investigate the OH stretching overtones of quasi-isolated water molecules. The exceptional time resolution along with the high spectral tunability in the mid-infrared spectral region make the setup very powerful and qualify it for a wide range of different experiments.

The experimental part of my work is divided into four chapters. First, quasi-isolated water molecules in $NaClO_4$ monohydrate were investigated. Through the usage of HDO:D_2O as a solvent, the sample was kept even more basic since here no splitting into symmetric and antisymmetric stretching is present and thus a single OH group is under investigation. In the world's first purely MIR pump–repump–probe experiments, the dynamics of the OH stretching overtones were observed. The data yielded the energy positions of the first three excited vibrational states. These were analyzed under the assumption of underlying Lippincott-Schroeder and Morse potentials. Going from the first to the second excited state, the respective lifetimes of (9 ± 2) ps and (1.4 ± 0.5) ps indicate a shortening that is much larger than expected when only considering the overlap of the wave functions. A more efficient energy transfer to high-lying combination tones involving the bend overtone and non-adiabatic vibrational relaxation were given as possible reasons. Furthermore, the data shows that relaxation proceeds in a stepwise manner from the second into the first excited state and then into the ground state. This observation demonstrates that vibrational PREP is not only capable of yielding quantitative lifetimes and spectral positions of the vibrational overtones but can also decipher the underlying relaxation pathways.

In a next experiment, the interaction of water molecules in small clusters was highlighted. The special feature of the water trimers in $Ba(ClO_4)_2$ trihydrate is that the formation of hydrogen bonds between the individual water molecules is strongly hindered due to the arrangement of the molecules. This shifts the focus to the transition dipole coupling via Ba^{2+} ions that can lead to delocalization of the OH stretching mode. Moreover, with pure H_2O as solvent, splitting into symmetric and antisymmetric stretching is present and one can observe the interplay of these two modes. The experimental data is in accordance with quantum simulations and group theoretical considerations that were conducted in the frame of $S6$ symmetry along with aspects of symmetry breakage. The latter may be due to low frequency modes and can cause localization of the stretching mode. After individual excitation of the symmetric or antisymmetric mode, population redistribution between the two modes was observed. A kinetic model was developed to extract the

respective relaxation rates and could be successfully applied to determine rates of roughly $(1.4\ \mathrm{ps})^{-1}$ and $(2.8\ \mathrm{ps})^{-1}$ for relaxation from symmetric into antisymmetric vibration and vice versa. Moreover, an effective population relaxation time of (8 ± 1) ps was obtained from the overall decay of the excited state signal. Simultaneous pumping of symmetric and antisymmetric vibration resulted in a quantum beating, which was observed via a combination tone that dominates the overtone spectrum. Proceeding with a time constant of (0.60 ± 0.07) ps, the decay of the beat signal indicates extraordinary long coherence between the symmetric and antisymmetric excitations, which may be related to the coupling to low-lying vibrations.

Chapter 5.3 is concerned with the relaxation dynamics in isotopically diluted ice I_h. Supplementary measurements in $Ba(ClO_4)_2 \cdot (HDO{+}2D_2O)$ and $NaCl \cdot (HDO{+}D_2O)$ were executed and the results were put in relation to the findings in ice. With all three samples being prepared with low molar $HDO{:}D_2O$, resonant energy transfer between individual OH groups is strongly hindered and the bend overtone at around 2900 cm^{-1} was identified to be the most evident relaxation channel. Calculations based on Fermi's golden rule were carried out in order to figure out whether the OH stretch relaxation dynamics can be explained with the bending overtone as exclusive dominant relaxation channel and whether the dynamics can be accounted for by a single prevailing deexcitation mode at all. The computations, however, delivered no physically reasonable accepting modes and it was concluded that more than one relaxation pathway must be involved. With a FWHM of roughly 70 cm^{-1}, the OH stretching's fundamental absorption in ice is generally much broader than the respective excitations found in the hydrate samples. Since the main difference between ice and hydrates is the coupling to the D_2O solvent in ice, the different bandwidths point towards the participation of solvent modes in the deexcitation in isotopically diluted ice. The findings are in good accordance with recent investigations that show that primarily the OH groups engaged in strong hydrogen bonds couple to the bend overtone, while those involved in weak H bonds preferably relax to solvent modes or form a strong hydrogen bond before relaxing to the bend overtone.

The last experimental chapter finally builds a bridge to neat ice I_h. Dynamic and spectral properties were put in relation to observations made on the OH stretching involved in a strong hydrogen bond in $LiNO_3$ trihydrate. In a sample prepared with low-molar $HDO{:}D_2O$ as solvent, this strong H bond yields a spectral broadening by a factor of roughly 4 upon going from the OH stretch fundamental to the ESA. This value is very similar to the one

measured in isotopically diluted ice I_h, which verifies the ice-like nature of the hydrate bond. In time-resolved measurements comparable acceleration rates of roughly 1.59 ps^{-1} and 1.46 ps^{-1} were extracted when proceeding from $LiNO_3$ in $HDO:D_2O$ to $LiNO_3$ solved in pure H_2O and when going from isotopically diluted to neat ice I_h. From a comparison to $Ba(ClO_4)_2$ trihydrate, where the corresponding rate is relatively small (about 0.04 ps^{-1}), it was concluded that radiation-free interactions, such as Förster transfer, only play a minor role in the relaxation of the H_2O species. The large acceleration in ice and $LiNO_3$ trihydrate instead was assigned to resonant coupling via strong hydrogen bonds. Since only three water molecules are involved in $LiNO_3$ trihydrate, it is reasoned that these three molecules can be considered as the smallest ice crystal with respect to the OH stretching vibration and its properties.

The above findings in connection with neat ice conclude the investigations on aqueous hydrates. With the study of isolated water molecules at the beginning and the investigations on bulk ice at the end, the present work represents a comprehensive overview of the vibrational properties of hydrogen bonded systems. The individual results deliver valuable information and parameters for the development of theoretical models that are capable of a profound and detailed description of OH stretching potentials and the underlying hydrogen bond system. The specific measured values and the conclusions drawn from them can be consulted as a spectral and dynamic fingerprint in any further measurement on aqueous systems. I personally hope that my observations can contribute to a better understanding of bulk ice and liquid water. Since the latter is the natural form of water at positive temperatures, the logical next step is to proceed to measurements in the liquid phase. Contrary to other liquids, the intermolecular motion in water vastly broadens the spectra of the underlying vibrational frequencies, which enormously complicates an investigation of the intra- and intermolecular relaxation pathways. Besides well-advanced measurement techniques, an understanding of these diverse mechanisms demands very sophisticated theoretical models. However, the already established knowledge and experience gained in the crystalline phase can aid in meeting this challenge. Moreover, the phase-resolved technique that was introduced in section 4.3.3 can be further developed in order to improve its spectral resolution. Like in 2D spectroscopy, simultaneous monitoring of the population dynamics and the transient phase can provide new and important information on the coupling to low-lying modes and unravel relaxation pathways that are covert so far. I am confident that persistent scientific work along with the advancing

technical state of the art can lead to a universal understanding of the various mechanisms that lend water its extraordinary properties.

Appendix

A.1 Details on the Simulations of the Symmetric and Antisymmetric OH Stretching Bands of $Ba(ClO_4)_2$ Trihydrate

The present paragraph provides a detailed description of the quantum chemical calculations that were performed to simulate the symmetric and antisymmetric OH stretching bands of $Ba(ClO_4)_2 \cdot 3H_2O$. The yielded spectrum is depicted in blue in Fig. 5.4 (d) in chapter 5.2.1. The simulations were carried out by Dr. Petko Petkov at the *Wilhelm-Ostwald-Institut für Physikalische und Theoretische Chemie* at the *Universität Leipzig*.
The VASP software package [154] is used to perform electronic structure calculations and vibrational analysis with the Perdew–Burke–Ernzerhof exchange-correlation functional [155]. A plane-wave basis with a 500 eV cutoff for the kinetic energy and projector-augmented wave description [156] of core-valence electron interactions are employed. The DFT-D2 method of Grimme [157] is applied to account for the van der Waals interactions resulting from the dynamical correlations between fluctuating charge distributions. Only Γ-point calculations are performed. Structural optimizations continue until the maximum forces acting on each atom are less than 0.012 eV$\mathring{A}^{-1}$. The unit cell of $Ba(ClO_4)_2$ trihydrate used for the calculations contains 2 Ba ions, 4 Cl ions, 22 O ions, and 12 H ions with dimensions of $a = b =$ 727.7 pm, $c =$ 965.6 pm, $\alpha = \beta =$ 90.0°, and $\gamma =$ 120.0°. In this model, there are two water trimers placed in subsequent planes behind each other (Fig. 5.4 (c)). In order to check the dependence of the OH vibrations with respect to the size of the unit cell, another two sets of calculations were performed. In these cases, the super cell has the dimensions $1 \times 1 \times 3$ and $3 \times 1 \times 1$ times the unit cell, respectively. Vibrational frequencies of the water molecules are calculated from the Hessian matrix using the density functional perturbation theory as it is implemented in VASP 5. The IR intensities are determined from the Born effective charge tensor. The calculated spectrum for the OH vibrations shown in Fig. 5.4 (d) was obtained by fitting the positions of the

bands with Gaussian functions with FWHMs of 35 cm^{-1}. For analysis of the water vibrations, the calculated vibrational frequencies were visualized along the displacement vectors and short movies that show the OH vibrations were recorded using the VMD software [158].

A.2 Measurements on $LiClO_4$ Trihydrate

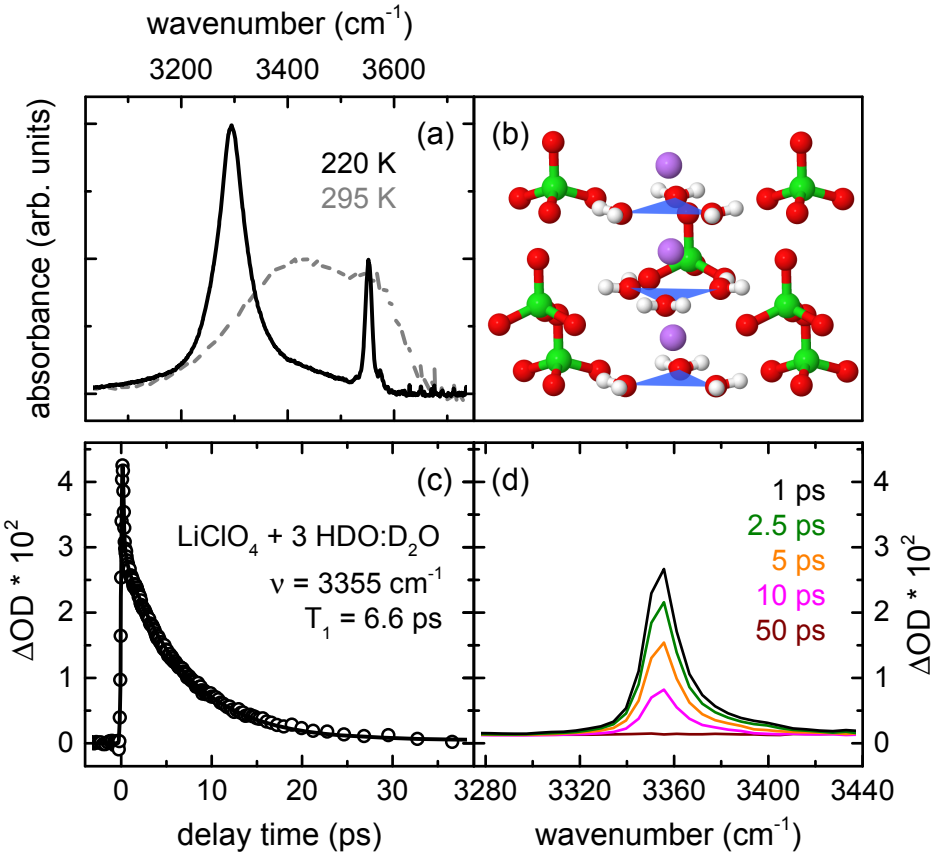

FIGURE A.1: (a) FTIR spectra of the OH stretching region of $LiClO_4$ dissolved in 5 M HDO:D_2O in the liquid and solid phase at 295 K (dashed gray) and 220 K (black). (b) Crystal structure of $LiClO_4$ trihydrate (Cl atoms in green, H in white, Li in purple, and O in red). The blue triangles indicate water trimers. (c) Transient measured in the ESA at 3355 cm^{-1}. (d) Pump–probe spectra of the ESA at several delay times.

Fig. A.1 (a) shows FTIR spectra measured in $LiClO_4$ trihydrate prepared with 5 M HDO:D_2O. In the crystalline phase at a sample temperature of 220 K, two features are visible (black line). The prominent one around 3300 cm^{-1} is due to a separate ice phase in the sample, while the smaller one at 3552 cm^{-1} with a FWHM of roughly 13 cm^{-1} stems from the water molecules bound in the hydrate crystal. Small sidebands that form around the latter absorption

band may be attributed to a small contamination with H_2O. The crystal structure of $LiClO_4$ trihydrate is known form X-ray and neutron diffraction data [159, 160]. It is depicted in Fig. (b). The water molecules arrange to clearly assignable trimers with O–O distances of 283 pm (indicated by blue trianlges in Fig. (b)), a value which is very similar to the one found for ice. Two next trimers in the vertical direction are twisted against each other by 60° and show a displacement of 273 pm. This is 210 pm less than the respective distance in $Ba(ClO_4)_2$ trihydrate, where salt ions and water molecules are situated in well separated planes (see Fig. 5.4 (b)). The ESA is found at (3355 ± 5) cm^{-1} and shows a FWHM of (18 ± 5) cm^{-1}. A transient measured in its maximum and corresponding pump–probe spectra are shown in Figs (c) and (d). The data yields a population lifetime of (6.6 ± 0.5) ps.

Bibliography

[1] M. Chaplin. “Do we underestimate the importance of water in cell biology?” In: *Nature Reviews Molecular Cell Biology* 7.11 (2006), 861–866.

[2] G. S. Hubbard, F. M. Naderi, and J. B. Garvin. “Following the water, the new program for Mars exploration”. In: *Acta Astronautica* 51.1 (2002), 337–350.

[3] A. Pohorille and L. R. Pratt. “Is Water the Universal Solvent for Life?” In: *Origins of Life and Evolution of Biospheres* (2012), 405–409.

[4] In: *Saggi di naturali esperienze* 1 (1667).

[5] F. H. Stillinger. “Water Revisited”. In: *Science* 209.4455 (1980), 451–457.

[6] J. Morgan and B. E. Warren. “X-Ray Analysis of the Structure of Water”. In: *The Journal of Chemical Physics* 6.11 (1938), 666–673.

[7] A. H. Narten and H. A. Levy. “Observed Diffraction Pattern and Proposed Models of Liquid Water”. In: *Science* 165.3892 (1969), 447–454.

[8] W. F. Kuhs and M. S. Lehmann. “The Structure of Ice Ih by Neutron Diffraction”. In: *The Journal of Physical Chemistry* 87.21 (1983), 4312–4313.

[9] A. K. Soper and M. G. Phillips. “A new determination of the structure of water at 25°C”. In: *Chemical Physics* 107.1 (1986), 47–60.

[10] K. Modig, B. G. Pfrommer, and B. Halle. “Temperature-Dependent Hydrogen-Bond Geometry in Liquid Water”. In: *Physical Review Letters* 90.7 (2003), 075502.

[11] Ph. Wernet, D. Nordlund, U. Bergmann, M. Cavalleri, M. Odelius, H. Ogasawara, L. Å. Näslund, T. K. Hirsch, L. Ojamäe, P. Glatzel, L. G. M. Pettersson, and A. Nilsson. “The Structure of the First Coordination Shell in Liquid Water”. In: *Science* 304.5673 (2004), 995–999.

[12] A. Tokmakoff. “Shining Light on the Rapidly Evolving Structure of Water”. In: *Science* 317.5834 (2007), 54–55.

[13] S. Ashihara, N. Huse, A. Espagne, E. T. J. Nibbering, and T. Elsaesser. "Ultrafast Structural Dynamics of Water Induced by Dissipation of Vibrational Energy". In: *The Journal of Physical Chemistry A* 111.5 (2007), 743–746.

[14] T. Elsässer and H. Van den Akker. *Ultrafast Hydrogen Bonding Dynamics and Proton Transfer Processes in the Condensed Phase*. Vol. 23. Springer Science & Business Media, 2013.

[15] C. N. R. Rao, P. C. Dwivedi, H. Ratajczak, and W. J. Orville-Thomas. "Relation between O–H stretching frequency and hydrogen bond energy: re-examination of the Badger–Bauer rule". In: *Journal of the Chemical Society, Faraday Transactions 2: Molecular and Chemical Physics* 71 (1975), 955–966.

[16] H. Graener, G. Seifert, and A. Laubereau. "New spectroscopy of water using tunable picosecond pulses in the infrared". In: *Physical Review Letters* 66.16 (1991), 2092–2095.

[17] S. Scheiner. *Hydrogen Bonding: A Theoretical Perspective*. Oxford University Press on Demand, 1997.

[18] S. Pandelov, B. M. Pilles, J. C. Werhahn, and H. Iglev. "Time-Resolved Dynamics of the OH Stretching Vibration in Aqueous NaCl Hydrate". In: *The Journal of Physical Chemistry A* 113.38 (2009), 10184–10188.

[19] S. Pandelov, J. C. Werhahn, B. M. Pilles, S. S. Xantheas, and H. Iglev. "An Empirical Correlation between the Enthalpy of Solution of Aqueous Salts and Their Ability to Form Hydrates". In: *The Journal of Physical Chemistry A* 114.38 (2010), 10454–10457.

[20] F. H. Allen. "The Cambridge Structural Database: a quarter of a million crystal structures and rising". In: *Acta Crystallographica Section B: Structural Science, Crystal Engineering and Materials* 58.3 (2002), 380–388.

[21] J. C. Werhahn, S. Pandelov, G. S. Fanourgakis, H. Iglev, and S. S. Xantheas. "Hydrogen Bonds in Aqueous Hydrates: Experiment and Theory". In: *International Conference on Ultrafast Phenomena*. Optical Society of America. 2010, MF5.

[22] J. C. Werhahn, S. Pandelov, S. S. Xantheas, and H. Iglev. "Dynamics of Weak, Bifurcated, and Strong Hydrogen Bonds in Lithium Nitrate Trihydrate". In: *The Journal of Physical Chemistry Letters* 2.13 (2011), 1633–1638.

[23] J. C. Werhahn, S. S. Xantheas, and H. Iglev. "Dynamics of the OH Stretching Vibration in Aqueous Hydrates". In: *International Conference on Ultrafast Structural Dynamics*. Optical Society of America. 2012, JT2A.45.

[24] A. Werner. "Ueber Haupt- und Nebenvalenzen und die Constitution der Ammoniumverbindungen". In: *Justus Liebigs Annalen der Chemie* 322.3 (1902), 261–296.

[25] A. Hantzsch. "Über die Isomerie-Gleichgewichte des Acetessigesters und die sogen. Isorrhopesis seiner Salze". In: *Berichte der deutschen chemischen Gesellschaft* 43.3 (1910), 3049–3076.

[26] T. S. Moore and T. F. Winmill. "CLXXVII.–The State of Amines in Aqueous Solution". In: *Journal of the Chemical Society, Transactions* 101 (1912), 1635–1676.

[27] P. Pfeiffer, Ph. Fischer, J. Kuntner, P. Monti, and Z. Pros. "Zur Theorie der Farblacke, II". In: *Justus Liebigs Annalen der Chemie* 398.2 (1913), 137–196.

[28] T. Steiner. "The Hydrogen Bond in the Solid State". In: *Angewandte Chemie International Edition* 41.1 (2002), 48–76.

[29] G. C. Pimentel and A. L. McClellan. *The hydrogen bond*. Freeman, San Francisco, 1960.

[30] H. Umeyama and K. Morokuma. "The Origin of Hydrogen Bonding. An Energy Decomposition Study". In: *Journal of the American Chemical Society* 99.5 (1977), 1316–1332.

[31] K. Morokuma. "Why do molecules interact? The origin of electron donor-acceptor complexes, hydrogen bonding and proton affinity". In: *Accounts of Chemical research* 10.8 (1977), 294–300.

[32] G. A. Jeffrey. *An Introduction to Hydrogen Bonding*. Vol. 12. Oxford university press New York, 1997.

[33] S. S. Xantheas and T. H. Dunning Jr. "Ab initio studies of cyclic water clusters $(H_2O)_n$, n = 1–6. I. Optimal structures and vibrational spectra". In: *The Journal of Chemical Physics* 99.11 (1993), 8774–8792.

[34] M. W. Feyereisen, D. Feller, and D. A. Dixon. "Hydrogen Bond Energy of the Water Dimer". In: *The Journal of Physical Chemistry* 100.8 (1996), 2993–2997.

[35] W. A. P. Luck. "The importance of cooperativity for the properties of liquid water". In: *Journal of Molecular Structure* 448.2 (1998), 131–142.

[36] Th. Steiner and W. Saenger. "Lengthening of the Covalent O–H Bond in O–H· · ·O Hydrogen Bonds Re-examined from Low-Temperature Neutron Diffraction Data of Organic Compounds". In: *Acta Crystallographica Section B: Structural Science, Crystal Engineering and Materials* 50.3 (1994), 348–357.

[37] R. Ludwig. "Water: From Clusters to the Bulk". In: *Angewandte Chemie International Edition* 40.10 (2001), 1808–1827.

[38] L. Ojamäe and K. Hermansson. "Ab Initio Study of Cooperativity in Water Chains: Binding Energies and Anharmonic Frequencies". In: *The Journal of Physical Chemistry* 98.16 (1994), 4271–4282.

[39] S. Scheiner. "Ab Initio Studies of Hydrogen Bonds: The Water Dimer Paradigm". In: *Annual Review of Physical Chemistry* 45.1 (1994), 23–56.

[40] T. K. Ghanty, V. N. Staroverov, P. R. Koren, and E. R. Davidson. "Is the Hydrogen Bond in Water Dimer and Ice Covalent?" In: *Journal of the American Chemical Society* 122.6 (2000), 1210–1214.

[41] U. Bergmann, A. Di Cicco, P. Wernet, E. Principi, P. Glatzel, and A. Nilsson. "Nearest-neighbor oxygen distances in liquid water and ice observed by x-ray Raman based extended x-ray absorption fine structure". In: *The Journal of Chemical Physics* 127.17 (2007), 174504.

[42] J.-B. Brubach, A. Mermet, A. Filabozzi, A. Gerschel, and P. Roy. "Signatures of the hydrogen bonding in the infrared bands of water". In: *The Journal of Chemical Physics* 122.18 (2005), 184509.

[43] N. Miura, H. Yamada, and A. Moon. "Intermolecular vibrational study in liquid water and ice by using far infrared spectroscopy with synchrotron radiation of MIRRORCLE 20". In: *Spectrochimica Acta Part A: Molecular and Biomolecular Spectroscopy* 77.5 (2010), 1048–1053.

[44] M. Heyden, J. Sun, S. Funkner, G. Mathias, H. Forbert, M. Havenith, and D. Marx. "Dissecting the THz spectrum of liquid water from first principles via correlations in time and space". In: *Proceedings of the National Academy of Sciences* 107.27 (2010), 12068–12073.

[45] J. Savolainen, S. Ahmed, and P. Hamm. "Two-dimensional Raman-terahertz spectroscopy of water". In: *Proceedings of the National Academy of Sciences* 110.51 (2013), 20402–20407.

[46] R. M. Badger. "A Relation Between Internuclear Distances and Bond Force Constants". In: *The Journal of Chemical Physics* 2.3 (1934), 128–131.

[47] R. M. Badger. "The Relation Between the Internuclear Distances and Force Constants of Molecules and Its Application to Polyatomic Molecules". In: *The Journal of Chemical Physics* 3.11 (1935), 710–714.

[48] T. Brinzer, E. J. Berquist, Z. Ren, S. Dutta, C. A. Johnson, C. S. Krisher, D. S. Lambrecht, and S. Garrett-Roe. "Ultrafast vibrational spectroscopy (2D-IR) of CO_2 in ionic liquids: Carbon capture from carbon dioxide's point of view". In: *The Journal of Chemical Physics* 142.21 (2015), 212425.

[49] R. Laenen, C. Rauscher, and A. Laubereau. "Dynamics of Local Substructures in Water Observed by Ultrafast Infrared Hole Burning". In: *Physical Review Letters* 80.12 (1998), 2622–2625.

[50] J. D. Smith, C. D. Cappa, K. R. Wilson, B. M. Messer, R. C. Cohen, and R. J. Saykally. "Energetics of Hydrogen Bond Network Rearrangements in Liquid Water". In: *Science* 306.5697 (2004), 851–853.

[51] F. Perakis, S. Widmer, and P. Hamm. "Two-dimensional infrared spectroscopy of isotope-diluted ice Ih". In: *The Journal of Chemical Physics* 134.20 (2011), 204505.

[52] F. Perakis, J. A. Borek, and P. Hamm. "Three-dimensional infrared spectroscopy of isotope-diluted ice Ih". In: *The Journal of Chemical Physics* 139.1 (2013), 014501.

[53] I. Bialynicki-Birula. "Classical Limit of Quantum Electrodynamics". In: *Acta Physica Austriaca* Suppl. 18 (1977).

[54] P. A. Franken, A. E. Hill, C. W. Peters, and G. Weinreich. "Generation of Optical Harmonics". In: *Physical Review Letters* 7.4 (1961), 118–119.

[55] P. G. Harper and B. S. Wherrett. *Nonlinear optics*. Academic press, 1977.

[56] R. W. Boyd. *Nonlinear optics*. Academic press, 2003.

[57] M. Bradler, P. Baum, and E. Riedle. "Femtosecond continuum generation in bulk laser host materials with sub-μJ pump pulses". In: *Applied Physics B* 97.3 (2009), 561–574.

[58] J.-C. Diels and W. Rudolph. *Ultrashort Laser Pulse Phenomena*. Academic press, 2006.

[59] C. Cohen-Tannoudji, B. Diu, and F. Laloë. *Quantum Mechanics, 2 Volume Set*. Wiley-VCH, 2006.

[60] A. Yariv. *Quantum electronics, 3rd edition*. Wiley, 1988.

[61] B. E. A. Saleh and M. C. Teich. *Fundamentals of photonics*. Vol. 3. 1991.

[62] J. Stenger, D. Madsen, P. Hamm, E. T. J. Nibbering, and T. Elsaesser. "Ultrafast Vibrational Dephasing of Liquid Water". In: *Physical Review Letters* 87.2 (2001), 027401.

[63] M. Bradler, J. C. Werhahn, D. Hutzler, S. Fuhrmann, R. Heider, E. Riedle, H. Iglev, and R. Kienberger. "A novel setup for femtosecond pump–repump–probe IR spectroscopy with few cycle CEP stable pulses". In: *Optics Express* 21.17 (2013), 20145–20158.

[64] M. Bradler, C. Homann, and E. Riedle. "Mid-IR femtosecond pulse generation on the microjoule level up to 5 μm at high repetition rates". In: *Optics Letters* 36.21 (2011), 4212–4214.

[65] A. H. Zewail. *The Nobelprize in Chemistry*. www.nobelprize.org, 1999.

[66] M. Schmeisser, A. Thaller, H. Iglev, and A. Laubereau. "Picosecond temperature and pressure jumps in ice". In: *New Journal of Physics* 8.6 (2006), 104.

[67] H. Iglev, M. Schmeisser, K. Simeonidis, A. Thaller, and A. Laubereau. "Ultrafast superheating and melting of bulk ice". In: *Nature* 439.7073 (2006), 183–186.

[68] B. S. Wherrett, A. L. Smirl, and T. F. Boggess. "Theory of Degenerate Four-Wave Mixing in Picosecond Excitation-Probe Experiments". In: *IEEE Journal of Quantum Electronics* 19.4 (1983), 680–690.

[69] H. J. Eichler, D. Langhans, and F. Massmann. "Coherence peaks in picosecond sampling experiments". In: *Optics Communications* 50.2 (1984), 117–122.

[70] T. F. Heinz, S. L. Palfrey, and T. J. Watson. "Contribution of phase gratings in pump–probe measurements of induced absorption". In: *Digest of technical papers from the OSA/IEEE 1985 conference on lasers and electro-optics*. 1985.

[71] M. W. Balk and G. R. Fleming. "Dependence of the coherence spike on the material dephasing time in pump–probe experiments". In: *The Journal of Chemical Physics* 83.9 (1985), 4300–4307.

[72] J. Buback, M. Kullmann, F. Langhojer, P. Nuernberger, R. Schmidt, F. Würthner, and T. Brixner. "Ultrafast Bidirectional Photoswitching of a Spiropyran". In: *Journal of the American Chemical Society* 132.46 (2010), 16510–16519.

[73] H. Iglev, M. K. Fischer, A. Gliserin, and A. Laubereau. "Ultrafast Geminate Recombination after Photodetachment of Aqueous Hydroxide". In: *Journal of the American Chemical Society* 133.4 (2010), 790–795.

[74] R. Disselkamp and G. E. Ewing. "High Vibrational States of Carbon Monoxide in Liquid Argon: Overtone Intensity Enhancement and Reactions with Oxygen". In: *The Journal of Physical Chemistry* 93.17 (1989), 6334–6339.

[75] S. M. Arrivo, T. P. Dougherty, W. T. Grubbs, and E. J. Heilweil. "Ultrafast infrared spectroscopy of vibrational CO-stretch up-pumping and relaxation dynamics of $W(CO)_6$". In: *Chemical Physics Letters* 235.3 (1995), 247–254.

[76] T. Witte, J. S. Yeston, M. Motzkus, E. J. Heilweil, and K.-L. Kompa. "Femtosecond infrared coherent excitation of liquid phase vibrational population distributions ($\nu > 5$)". In: *Chemical Physics Letters* 392.1 (2004), 156–161.

[77] D. J. Ulness, J. C. Kirkwood, and A. C. Albrecht. "Competitive events in fifth order time resolved coherent Raman scattering: Direct versus sequential processes". In: *The Journal of Chemical Physics* 108.10 (1998), 3897–3902.

[78] D. A. Blank, L. J. Kaufman, and G. R. Fleming. "Fifth-order two-dimensional Raman spectra of CS_2 are dominated by third-order cascades". In: *The Journal of Chemical Physics* 111.7 (1999), 3105–3114.

[79] K. C. Wilson, B. Lyons, R. Mehlenbacher, R. Sabatini, and D. W. McCamant. "Two-dimensional femtosecond stimulated Raman spectroscopy: Observation of cascading Raman signals in acetonitrile". In: *The Journal of Chemical Physics* 131.21 (2009), 214502.

[80] B. Zhao, Z. Sun, and S.-Y. Lee. "Quantum theory of time-resolved femtosecond stimulated Raman spectroscopy: Direct versus cascade processes and application to $CDCl_3$". In: *The Journal of Chemical Physics* 134.2 (2011), 024307.

[81] E. Tokunaga, A. Terasaki, and T. Kobayashi. "Frequency-domain interferometer for femtosecond time-resolved phase spectroscopy". In: *Optics Letters* 17.16 (1992), 1131–1133.

[82] T. Fuji, T. Yoda, T. Hattori, and H. Nakatsuka. "Phase Sensitive Pump–Probe Spectroscopy Using a Michelson-Type Interferometer". In: *Japanese Journal of Applied Physics* 39.4R (2000), 1738–1742.

[83] F. E. Robles, P. Samineni, J. W. Wilson, and W. S. Warren. "Pump–probe nonlinear phase dispersion spectroscopy". In: *Optics Express* 21.8 (2013), 9353–9364.

[84] B. Wilhelmi and E. Heumann. "Refractive index change from vibrational excitation in induced Raman scattering". In: *Journal of Applied Spectroscopy* 19.3 (1973), 1233–1235.

[85] D. Hutzler, J. C. Werhahn, R. Heider, M. Bradler, R. Kienberger, E. Riedle, and H. Iglev. "Highly Selective Relaxation of the OH Stretching Overtones in Isolated HDO Molecules Observed by Infrared Pump–Repump–Probe Spectroscopy". In: *The Journal of Physical Chemistry A* 119.26 (2015), 6831–6836.

[86] B. Berglund, J. O. Thomas, and R. Tellgren. "Hydrogen Bond Studies. CII. An X-ray Determination of the Crystal Structure of Sodium Perchlorate Monohydrate, $NaClO_4.H_2O$". In: *Acta Crystallographica Section B: Structural Science, Crystal Engineering and Materials* 31.7 (1975), 1842–1846.

[87] B. Berglund, R. Tellgren, and J. O. Thomas. "Hydrogen bond studies. CXVI. A Neutron Diffraction Study of the Structure of Sodium Perchlorate Monohydrate, $NaClO_4.H_2O$, at 298 K". In: *Acta Crystallographica Section B: Structural Science, Crystal Engineering and Materials* 32.8 (1976), 2444–2449.

[88] M. Schmeisser, H. Iglev, and A. Laubereau. "Maximum superheating of bulk ice". In: *Chemical Physics Letters* 442.4 (2007), 171–175.

[89] S. Woutersen, U. Emmerichs, H.-K. Nienhuys, and H. J. Bakker. "Anomalous temperature dependence of vibrational lifetimes in water and ice". In: *Physical Review Letters* 81.5 (1998), 1106–1109.

[90] R. Timmer and H. Bakker. "Vibrational Förster Transfer in Ice Ih". In: *The Journal of Physical Chemistry A* 114.12 (2010), 4148–4155.

[91] J. L. Bishop, R. Quinn, and M. D. Dyar. "Spectral and thermal properties of perchlorate salts and implications for Mars". In: *American Mineralogist*, 99.8-9 (2014), 1580–1592.

[92] Y. Chen, Y.-H. Zhang, and L.-J. Zhao. "ATR-FTIR spectroscopic studies on aqueous $LiClO_4$, $NaClO_4$, and $Mg(ClO_4)_2$ solutions". In: *Physical Chemistry Chemical Physics* 6.3 (2004), 537–542.

[93] C. P. Lawrence and J. Skinner. "Vibrational spectroscopy of HOD in liquid D_2O. I. Vibrational energy relaxation". In: *Journal of Chemical Physics* 117.12 (2002), 5827–5838.

[94] R. Rey, K. B. Møller, and J. T. Hynes. "Ultrafast Vibrational Population Dynamics of Water and Related Systems: A Theoretical Perspective". In: *Chemical Reviews* 104.4 (2004), 1915–1928.

[95] J. Lindner, P. Vöhringer, M. S. Pshenichnikov, D. Cringus, D. A. Wiersma, and M. Mostovoy. "Vibrational relaxation of pure liquid water". In: *Chemical Physics Letters* 421.4 (2006), 329–333.

[96] L. De Marco, K. Ramasesha, and A. Tokmakoff. "Experimental Evidence of Fermi Resonances in Isotopically Dilute Water from Ultrafast Broadband IR Spectroscopy". In: *The Journal of Physical Chemistry B* 117.49 (2013), 15319–15327.

[97] J. A. C. Gallas. "Some matrix elements for Morse oscillators". In: *Physical Review A* 21.6 (1980), 1829–1834.

[98] E. F. de Lima and J. E. M. Hornos. "Matrix elements for the Morse potential under an external field". In: *Journal of Physics B: Atomic, Molecular and Optical Physics* 38.7 (2005), 815–825.

[99] J. C. Werhahn. "Theoretical & Experimental Investigations of Hydrogen Bonded Systems from Cluster to Bulk". PhD thesis. Technische Universität München, 2012, 100–103.

[100] S. S. Xantheas and J. C. Werhahn. "Universal scaling of potential energy functions describing intermolecular interactions. I. Foundations and scalable forms of new generalized Mie, Lennard-Jones, Morse, and Buckingham exponential-6 potentials". In: *The Journal of Chemical Physics* 141.6 (2014), 064117.

[101] J. C. Werhahn, D. Akase, and S. S. Xantheas. "Universal scaling of potential energy functions describing intermolecular interactions. II. The halide-water and alkali metal-water interactions". In: *The Journal of Chemical Physics* 141.6 (2014), 064118.

[102] H. J. Bakker and H.-K. Nienhuys. "Delocalization of Protons in Liquid Water". In: *Science* 297.5581 (2002), 587–590.

[103] A. M. Dokter and H. J. Bakker. "Transient absorption of vibrationally excited ice Ih". In: *The Journal of Chemical Physics* 128.2 (2008), 024502.

[104] E. R. Lippincott and R. Schroeder. "One-Dimensional Model of the Hydrogen Bond". In: *The Journal of Chemical Physics* 23.6 (1955), 1099–1106.

[105] R. Chidambaram, R. Balasubramanian, and G. N. Ramachandran. "Potential functions for hydrogen bond interactions I. A modified Lippincott-Schroeder potential function for NH· · ·O interaction between peptide groups". In: *Biochimica et Biophysica Acta (BBA) - Protein Structure* 221.2 (1970), 182–195.

[106] H.-J. Kim and B.-G. Yoon. "Study of the Librational Motion of H_2O Molecules in Hydrates by Neutron Inelastic Scattering". In: *Journal of the Korean Nuclear Society* 11.1 (1979), 1–20.

[107] K. Liu, J. D. Cruzan, and R. J. Saykally. "Water Clusters". In: *Science* 271.5251 (1996), 929–933.

[108] S. S. Xantheas. "Cooperativity and hydrogen bonding network in water clusters". In: *Chemical Physics* 258.2 (2000), 225–231.

[109] F. N. Keutsch and R. J. Saykally. "Water clusters: Untangling the mysteries of the liquid, one molecule at a time". In: *Proceedings of the National Academy of Sciences* 98.19 (2001), 10533–10540.

[110] G. Chałasiński, M. M. Szczęśniak, P. Cieplak, and S. Scheiner. "Ab initio study of intermolecular potential of H_2O trimer". In: *The Journal of Chemical Physics* 94.4 (1991), 2873–2883.

[111] F. N. Keutsch, J. D. Cruzan, and R. J. Saykally. "The Water Trimer". In: *Chemical Reviews* 103.7 (2003), 2533–2578.

[112] N. Pugliano and R. J. Saykally. "Measurement of Quantum Tunneling Between Chiral Isomers of the Cyclic Water Trimer". In: *Science* (1992), 1937–1940.

[113] S. S. Xantheas and T. H. Dunning Jr. "The structure of the water trimer from ab initio calculations". In: *The Journal of Chemical Physics* 98.10 (1993), 8037–8040.

[114] K. Liu, J. G. Loeser, M. J. Elrod, B. C. Host, J. A. Rzepiela, N. Pugliano, and R. J. Saykally. "Dynamics of Structural Rearrangements in the Water Trimer". In: *Journal of the American Chemical Society* 116.8 (1994), 3507–3512.

[115] H. D. Lutz. "Structure and strength of hydrogen bonds in inorganic solids". In: *Journal of Molecular Structure* 646.1 (2003), 227–236.

[116] F. Zhang, K. Li, H. Ratajczak, and D. Xue. "Hydrogen bonds in inorganic crystals: A microscopic study on the valence electron distribution of hydrogen in O–H· · ·O systems". In: *Journal of Molecular Structure* 976.1 (2010), 69–72.

[117] W. J. Smit and H. J. Bakker. "Vibrational Energy Relaxation of Water Molecules in a Hydrated Lithium Nitrate Crystal". In: *The Journal of Physical Chemistry C* 120.20 (2016), 11078–11084.

[118] S. Mani N. V. Ramaseshan. "The crystal structure of barium perchlorate trihydrate $Ba(ClO_4)_2 \cdot 3H_2O$ and the crystal coordination of Ba^{++} Ion". In: *Zeitschrift für Kristallographie - Crystalline Materials* 114.1-6 (1960), 200–214.

[119] G. Brink and M. Falk. "Infrared studies of water in crystalline hydrates: $NaClO_4 \cdot H_2O$, $LiClO_4 \cdot 3H_2O$, and $Ba(ClO_4)_2 \cdot 3H_2O$". In: *Canadian Journal of Chemistry* 48.13 (1970), 2096–2103.

[120] J. C. Gallucci and R. E. Gerkin. "Structure of Barium Perchlorate Trihydrate". In: *Acta Crystallographica Section C: Structural Chemistry* 44.11 (1988), 1873–1876.

[121] G. E. Walrafen. "Raman Spectral Studies of the Effects of Perchlorate Ion on Water Structure". In: *The Journal of Chemical Physics* 52.8 (1970), 4176–4198.

[122] D. B. Wong, C. H. Giammanco, E. E. Fenn, and M. D. Fayer. "Dynamics of Isolated Water Molecules in a Sea of Ions in a Room Temperature Ionic Liquid". In: *The Journal of Physical Chemistry B* 117.2 (2013), 623–635.

[123] V. M. Kenkre, A. Tokmakoff, and M. D. Fayer. "Theory of vibrational relaxation of polyatomic molecules in liquids". In: *The Journal of Chemical Physics* 101.12 (1994), 10618–10629.

[124] V. Tiwari, W. K. Peters, and D. M. Jonas. "Energy Transfer: Vibronic coherence unveiled". In: *Nature Chemistry* 6.3 (2014), 173–175.

[125] L. Wang, G. B. Griffin, A. Zhang, F. Zhai, N. E. Williams, R. F. Jordan, and G. S. Engel. "Controlling quantum-beating signals in 2D electronic spectra by packing synthetic heterodimers on single-walled carbon nanotubes". In: *Nature Chemistry* 9 (2017), 219–225.

[126] A. W. Chin, J. Prior, R. Rosenbach, F. Caycedo-Soler, S. F. Huelga, and M. B. Plenio. "The role of non-equilibrium vibrational structures in electronic coherence and recoherence in pigment-protein complexes". In: *Nature Physics* 9.2 (2013), 113–118.

[127] J. Lim, D. Paleček, F. Caycedo-Soler, C. N. Lincoln, J. Prior, H. Von Berlepsch, S. F. Huelga, M. B. Plenio, D. Zigmantas, and J. Hauer. "Vibronic origin of long-lived coherence in an artificial molecular light harvester". In: *Nature Communications* 6 (2015), 1–7.

[128] H. J. Prask, S. F. Trevino, J. D. Gault, and K. W. Logan. "Ice I-Lattice Dynamics and Incoherent Neutron Scattering". In: *The Journal of Chemical Physics* 56.7 (1972), 3217–3225.

[129] J. E. Bertie and E. Whalley. "Infrared Spectra of Ices Ih and Ic in the Range 4000 to 350 cm^{-1}". In: *The Journal of Chemical Physics* 40.6 (1964), 1637–1645.

[130] J. E. Bertie and E. Whalley. "Optical Spectra of Orientationally Disordered Crystals. II. Infrared Spectrum of Ice Ih and Ice Ic from 360 to 50 cm^{-1}". In: *The Journal of Chemical Physics* 46.4 (1967), 1271–1284.

[131] J. R. Scherer and R. G. Snyder. "Raman intensities of single crystal ice I_h". In: *The Journal of Chemical Physics* 67.11 (1977), 4794–4811.

[132] E. Whalley. "A detailed assignment of the O–H stretching bands of ice I". In: *Canadian Journal of Chemistry* 55.19 (1977), 3429–3441.

[133] Z. Wang, A. Pakoulev, Y. Pang, and D. D. Dlott. "Vibrational Substructure in the OH Stretching Transition of Water and HOD". In: *The Journal of Physical Chemistry A* 108.42 (2004), 9054–9063.

[134] R. Rey and J. T. Hynes. "Vibrational energy relaxation of HOD in liquid D_2O". In: *The Journal of Chemical Physics* 104.6 (1996), 2356–2368.

[135] H.-K. Nienhuys, S. Woutersen, R. A. van Santen, and H. J. Bakker. "Mechanism for vibrational relaxation in water investigated by femtosecond infrared spectroscopy". In: *The Journal of Chemical Physics* 111.4 (1999), 1494–1500.

[136] J. C. Deàk, S. T. Rhea, L. K. Iwaki, and D. D. Dlott. "Vibrational Energy Relaxation and Spectral Diffusion in Water and Deuterated Water". In: *The Journal of Physical Chemistry A* 104.21 (2000), 4866–4875.

[137] F. Franks. *Water: A Comprehensive Treatise, Vol. 1*. Plenum Press, New York, 1972.

[138] M. D. Fayer. *Ultrafast Infrared Vibrational Spectroscopy*. CRC Press, 2013.

[139] M. Vinaykin and A. V. Benderskii. "Vibrational Sum-Frequency Spectrum of the Water Bend at the Air/Water Interface". In: *The Journal of Physical Chemistry Letters* 3.22 (2012), 3348–3352.

[140] Y. Nagata, C.-S. Hsieh, T. Hasegawa, J. Voll, E. H. G. Backus, and M. Bonn. "Water Bending Mode at the Water–Vapor Interface Probed by Sum-Frequency Generation Spectroscopy: A Combined Molecular Dynamics Simulation and Experimental Study". In: *The Journal of Physical Chemistry Letters* 4.11 (2013), 1872–1877.

[141] Y. Ni and J. L. Skinner. "IR and SFG vibrational spectroscopy of the water bend in the bulk liquid and at the liquid-vapor interface, respectively". In: *The Journal of Chemical Physics* 143.1 (2015), 014502.

[142] C. P. Lawrence and J. L. Skinner. "Vibrational spectroscopy of HOD in liquid D_2O. VI. Intramolecular and intermolecular vibrational energy flow". In: *The Journal of Chemical Physics* 119.3 (2003), 1623–1633.

[143] F. Li and J. L. Skinner. "Infrared and Raman line shapes for ice Ih. II. H_2O and D_2O". In: *The Journal of Chemical Physics* 133.24 (2010), 244504.

[144] C. J. Burnham, J. Li, S. S. Xantheas, and M. Leslie. "The parametrization of a Thole-type all-atom polarizable water model from first principles and its application to the study of water clusters (n= 2–21) and the phonon spectrum of ice Ih". In: *The Journal of Chemical Physics* 110.9 (1999), 4566–4581.

[145] H. Fukazawa and S. Mae. "The vibrational spectra of ice Ih and polar ice". In: *Physics of Ice Core Records*. Hokkaido University Press. 2000, 25–42.

[146] V. Buch and J. P. Devlin. "A new interpretation of the OH-stretch spectrum of ice". In: *The Journal of Chemical Physics* 110.7 (1999), 3437–3443.

[147] M. S. Bergren and S. A. Rice. "An improved analysis of the OH stretching region of the vibrational spectrum of ice Ih". In: *The Journal of Chemical Physics* 77.2 (1982), 583–602.

[148] S. A. Rice, M. S. Bergren, A. C. Belch, and G. Nielsen. "A Theoretical Analysis of the OH Stretching Spectra of Ice Ih, Liquid Water, and Amorphous Solid Water". In: *The Journal of Physical Chemistry* 87.21 (1983), 4295–4308.

[149] F. Perakis and P. Hamm. "Two-dimensional infrared spectroscopy of neat ice Ih". In: *Physical Chemistry Chemical Physics* 14.18 (2012), 6250–6256.

[150] L. Shi, J. L. Skinner, and T. L. C. Jansen. "Two-dimensional infrared spectroscopy of neat ice I_h". In: *Physical Chemistry Chemical Physics* 18.5 (2016), 3772–3779.

[151] A. Lock, H. Bakker, et al. "Temperature dependence of vibrational relaxation in liquid H2O". In: *Journal of Chemical Physics* 117.4 (2002), 1708–1713.

[152] K. Hermansson, J. O. Thomas, and I. Olovsson. "Hydrogen Bond Studies. CXX. An X-ray Determination of the Crystal Structure of $LiNO_3.3H_2O$". In: *Acta Crystallographica Section B: Structural Science, Crystal Engineering and Materials* 33.9 (1977), 2857–2861.

[153] K Hermansson, J. O. Thomas, and I. Olovsson. "Hydrogen Bond Studies. CXXXVIII. Neutron Diffraction Studies of $LiNO_3.3H_2O$ at 120 and 295 K". In: *Acta Crystallographica Section B: Structural Science, Crystal Engineering and Materials* 36.5 (1980), 1032–1040.

[154] G. Kresse and J. Furthmüller. "Efficient iterative schemes for ab initio total-energy calculations using a plane-wave basis set". In: *Physical Review B* 54.16 (1996), 11169–11186.

[155] J. P. Perdew, K. Burke, and M. Ernzerhof. "Generalized Gradient Approximation Made Simple". In: *Physical Review Letters* 77.18 (1996), 3865–3868.

[156] G. Kresse and D. Joubert. "From ultrasoft pseudopotentials to the projector augmented-wave method". In: *Physical Review B* 59.3 (1999), 1758–1775.

[157] S. Grimme. "Semiempirical GGA-Type Density Functional Constructed with a Long-Range Dispersion Correction". In: *Journal of Computational Chemistry* 27.15 (2006), 1787–1799.

[158] W. Humphrey, A. Dalke, and K. Schulten. "VMD: Visual Molecular Dynamics". In: *Journal of Molecular Graphics* 14.1 (1996), 33–38.

[159] C. D. West. "Crystal Structures of some Hydrated Compounds. I. $LiClO_4 \cdot 3H_2O$, $LiI \cdot 3H_2O$, $Ba(ClO_4)_2 \cdot H_2O$". In: *Zeitschrift für Kristallographie - Crystalline Materials* 88.1-6 (1934), 198–204.

[160] A. Sequeira, I. Bernal, I. D. Brown, and R. Faggiani. "The Structure of Lithium Perchlorate Trihydrate $Li(H_2O)_3ClO_4$ – an X-ray and Neutron Diffraction Study". In: *Acta Crystallographica Section B: Structural Science, Crystal Engineering and Materials* 31.6 (1975), 1735–1739.

Acknowledgements

I want to take the opportunity to thank all those who helped and supported me during the last years. Without you, this work would not have been possible.

My sincere thanks go to **Prof. Reinhard Kienberger** for giving me the opportunity to conduct my PhD research at the *Chair for Laser and X-ray Physics E11* at the *Technische Universität München*. Thank you for granting me access to a powerful setup and supporting me in all matters, including informative discussions on physical topics, but also bureaucratic issues and everything else that fell due.

I want to thank my direct supervisor **Dr. Hristo Iglev** for the great mentoring and guidance. I am very grateful for long and fruitful discussions, for all the thought-provoking impulses that oftentimes directed me out of a dead end, and not least for sharing your experience and expertise with me.
Moreover, I want to thank **Dr. Jasper Werhahn**, who introduced me to the team and accompanied me during my first steps in the laboratory. Thank you for making me feel at home right from the beginning.

A big thank you to **Rupert Heider**, **Klara Stallhofer**, and **Christian Brunner**, who, during their master theses, substantially contributed to the experiments and data analysis that is shown in this work and of course to **Jasper** and **Wolfi** for proofreading and suggested improvements.

I had the pleasure of being part of a great team here at the *E11*. Therefore, my gratitude goes to all bachelor, master and PhD students, to my bureau roommates **Andi**, **Michi**, **Martin**, **Rupert**, and **Wolfi**, and all those that came and went during my time at the chair.

A special *Vergelt's Gott* to the workshop crew, **Wolfgang Dürichen** and **Lukas Loidl**, who always were available when any mechanical requirements or problems occurred during the experiments. Not forgetting our secretaries **Susi Würzinger** and **Stefanie Völkl**, who always were on their toes when there were any bureaucratic issues to be dealt with.

I want to thank all of my friends, the old and newly found ones, for the very welcome distractions, for one or the other closing time pint, and for nice conversations about all the world and his wife, but no physical topics. Happy to have you!

Last but not least, this work could not have been realized without the support and love of my family. I want to thank my parents, **Heidelinde** and **Rudolf**, and my brother **Jochen** for always being there for me. It's good to know that I can always count on your support no matter what I need. Thank you!

At the very end, I want to express special thanks to my wonderful girlfriend **Christina**. Thank you for your support, your patience, and for always believing in what I am doing.